Mitochondria-Lysosome Crosstalk Shapes Metabolic Transition in Neonatal Enterocytes

Gonzalo Herranz,[1,2] Diego Alonso-Larre,[1,2,10] Tamara González,[1,2,10] Laura Akintche,[1,2] Alejandra Ramos-Manzano,[1,2,7] Marta Iborra-Pernichi,[1,2,8], María Velasco de la Esperanza[1,2], Covadonga Díaz-Díaz,[1,2,9] Ian G Ganley,[3] Patricia Boya,[4,5] Sara Cogliati,[6] Nuria Martínez-Martín,[1,2]* and Fernando Martín-Belmonte[1,2,11]**

[1]Program of Tissue and Organ Homeostasis, Centro de Biología Molecular Severo Ochoa, Consejo Superior de Investigaciones Científicas-Universidad Autónoma de Madrid, Madrid, Spain

[2]Intestinal Morphogenesis and Homeostasis Group, Área 3-Cancer, Instituto Ramón y Cajal de Investigación Sanitaria (IRYCIS), Madrid, Spain

[3]MRC Protein Phosphorylation and Ubiquitylation Unit, University of Dundee, Dundee, UK

[4]Dept of Cellular and Molecular Biology, Centro de Investigaciones Biológicas Margarita Salas, CSIC, Madrid, Spain

[5]Department of Neuroscience and Movement Science, Section of Medicine, University of Fribourg, Fribourg, Switzerland

[6]Program of Physiological and Pathological Processes, Centro de Biología Molecular Severo Ochoa, Consejo Superior de Investigaciones Científicas-Universidad Autónoma de Madrid, Madrid, Spain

[7]Present addresses: Immunology Department, Hospital Universitario de La Princesa, Instituto de Investigación Sanitaria (IIS)-Princesa, Madrid, Spain; Medicine Department, School of Medicine, Universidad Autónoma of Madrid, Madrid, Spain

[8]Present address: B Lymphocyte Biology Lab, Centro Nacional de Investigaciones Cardiovasculares (CNIC), Madrid, Spain

[9]Present addresses: Cardiovascular Regeneration Program, Centro Nacional de Investigaciones Cardiovasculares (CNIC), Madrid, Spain; Centro de Investigación Biomédica en Red de Enfermedades Cardiovasculares (CIBERCV), Madrid, Spain

[10]These authors contributed equally

[11]Senior author and Lead contact

*Correspondence: nmartinez@cbm.csic.es

**Correspondence: fmartin@cbm.csic.es

SUMMARY

The neonatal gastrointestinal tract mediates nutrient absorption and the establishment of immune tolerance to commensal microbiota. In early life, lysosome-rich enterocytes (LREs) in the ileum are necessary for the intracellular digestion of maternal milk proteins. However, the molecular mechanisms sustaining their function remain incompletely characterized. Here, we demonstrate that LRE mitochondrial homeostasis and autophagic capacity are critical for efficient nutrient uptake and maintenance of their specialized identity, as disruption of either process leads to premature differentiation into post-weaning enterocytes (PECs) with diminished endolysosomal and metabolic activity. Transcriptomic profiling further revealed that neonatal LREs exhibit a distinctive antioxidant signature, which preserves redox balance and safeguards the expression of the transcriptional regulators MAFB and BLIMP1, both central repressors of the neonatal-to-adult metabolic transition. These findings establish the mitochondria–lysosome axis as a key determinant of LRE function and neonatal metabolic programming. They also provide a mechanistic framework for understanding how organelle dysfunction and redox imbalance may contribute to early-life malnutrition syndromes, such as Kwashiorkor, and suggest therapeutic strategies aimed at preserving mitochondrial and lysosomal integrity.

KEYWORDS

Intestine, Enterocyte, Autophagy, Mitochondria, Lysosome, Neonatal, Metabolic Switch, ROS, Nutrient Absorption, Mouse

INTRODUCTION

The small intestine is a specialized section of the gastrointestinal tract (GIT) engaged in nutrient digestion and absorption, while simultaneously acting as a barrier against harmful substances. It consists of a variety of cell types, with epithelial and immune cells playing key roles in maintaining intestinal function. Through their interactions with one another and the gut microbiota, these cells help create a finely balanced microenvironment that supports both nutritional and immunological functions[1,2]. The main absorptive epithelial cells in the intestine are called enterocytes. They are the most numerous cells in the intestinal epithelium and, along with secretory epithelial cells (including Paneth, goblet, and enteroendocrine cells), originate from stem cells of the intestinal crypts[1].

Dietary protein is a macronutrient essential for growth and overall organismal homeostasis. In weaned mammals, protein digestion takes place in the lumen of GIT, where gastric pepsin and intestinal proteases sequentially break down proteins into oligopeptides and free amino acids, which are then absorbed by enterocytes via specific transporters[3–5].

However, in the intestinal lumen of suckling mammals and stomachless fishes, protease activity remains low and protein digestion is incomplete[3–5]. For this reason, their posterior-mid small intestine contains a population of lysosome-rich enterocytes (LREs), formerly referred to as vacuolated enterocytes[6–8]. These cells possess a highly developed endolysosomal system, including a prominent lysosomal vacuole (LV), which is capable of internalising and metabolising intact proteins via non-specific fluid-phase processes (pinocytosis) and receptor-mediated endocytosis and membrane adsorption[5,7,9,10]. Moreover, LREs facilitate the transcytosis of antigens, maternal immunoglobulins, and antibodies across the epithelial barrier while preserving their biological activity, contributing to the immune system development[5,11]. Recent studies have highlighted the nutritional importance of LREs during the neonatal period. Key endolysosomal proteins, whose absence leads to developmental defects, have been identified, including Mucolipins 1 and 3[12], Pllp[8], Mamdc4 (also known as endotubin)[13] and Dab2[7]. Despite these findings, the molecular mechanisms that regulate endocytic and lysosomal pathways in LREs are still not fully understood.

Autophagy is a conserved lysosome-dependent catabolic pathway that recycles intracellular components and nutrients. This process involves the sequestration of cytoplasmic material into double-membraned autophagosomes, which subsequently fuse with lysosomes for degradation and breakdown. The lipidation of LC3, a key step in autophagosome formation, is mediated by the ATG12–ATG5–ATG16L1 complex[14,15]. Mutations in components of this complex have been linked to intestinal pathologies[16,17], and *Atg5*-deficient neonates exhibit increased neonatal mortality under fasting conditions, underscoring the essential role of autophagy during early postnatal life[18]. Despite this, the homeostatic role of autophagy throughout the entire neonatal period, particularly in LRE biology, remains unclear.

Autophagy plays a crucial role in cellular metabolism and differentiation, primarily through the selective elimination of mitochondria (mitophagy), thereby contributing to the control of reactive oxygen species (ROS) levels[19,20]. Beyond their role in energy production, mitochondria and ROS also function as key

regulators of cell signalling and differentiation[21–23]. In the intestinal epithelium, a gradient of increasing mitochondrial mass, activity, and ROS levels has been described along the crypt–villus axis, correlating with higher degrees of cellular differentiation[24]. However, how mitochondrial homeostasis and ROS dynamics influence the developmental remodelling of enterocytes remains poorly understood. In particular, their role in regulating the metabolic and functional transition of neonatal LREs into post-weaning enterocytes (PECs) has not yet been explored.

This study reveals that the mitochondria–lysosome axis is essential for the function and maturation of LREs. We show that LREs rely on high autophagic and mitophagic activity to sustain nutrient absorption and lysosomal integrity, and that disruption of either autophagy (*Atg16*cKO) or mitochondrial homeostasis (*Tfam*cKO) leads to impaired endolysosomal function, oxidative stress, and premature weaning transition through the repression of the transcription factors BLIMP1 and MAFB. These findings establish organelle homeostasis as a critical determinant of neonatal enterocyte identity and provide mechanistic insights into how its disruption contributes to childhood malnutrition.

RESULTS

Lysosome-rich enterocytes (LREs) display heightened basal autophagy levels essential for absorptive function

Unlike adult enterocytes, LREs rely on intracellular digestion within lysosomes to process macromolecular nutrients. This process demands a highly active endolysosomal system that breaks down complex proteins into absorbable units, which confers a particular architecture to LREs (**Figures S1A and S1B**)[9]. Autophagy, the cellular mechanism responsible for degrading and recycling cellular components, plays a central role in maintaining lysosomal function and turnover[25]. In LREs, elevated basal autophagy may support endolysosomal activity. Exploring this hypothesis could clarify the role of autophagy in the absorption and processing of nutrients in neonates, as well as its contribution to early development.

Utilising the GFP-LC3 transgenic mouse model (*GFP-Map1lc3a*$^{TG/+}$) [26], we visualised autophagosomes as GFP-LC3 positive puncta and monitored autophagy flux via western blot (WB) by assessing the levels of free GFP, a byproduct of lysosomal degradation of GFP-LC3 II (**Figures 1A, 1B and S1C**)[27,28]. The presence and activity of LREs was determined by probing with mCherry/ fluorescent dextrans that are internalised as a macromolecule by LREs, but not by PECs (**Figures 1A, 1B, S1C, and S1D**)[7]. Following gavage, fluorescent-dextran was rapidly internalised from the lumen into early and late endosomes (**Figure S1D**, arrowheads), accumulating progressively in lysosomal vacuoles (LVs) (**Figure S1D**, arrows). WB analysis was performed on lysates in epithelial cells from both proximal and distal sections of small intestines in GFP-LC3 mice at neonatal stages (P1, P7 and P14), and post-weaning (P21–30). This analysis revealed a proximal-distal gradient of protein absorption and autophagic degradation, mirroring the anterior-posterior intestinal maturation (**Figure 1B**)[29].

115 In the distal intestine, protein absorption preceded the induction of autophagy, with a subtle onset already
116 detectable at P1, although no free GFP signal was observed. By P7, both mCherry uptake and free GFP
117 increased markedly, with a strong accumulation of free GFP (**Figure 1B**, pink rectangle), indicating peak
118 autophagic activity in LREs—coinciding with the establishment of neonatal intestinal features[30]. At P14,
119 mCherry absorption persisted in the distal region, while free GFP levels declined, and by weaning (P21)
120 both signals were absent (**Figure 1B**). Quantification of mCherry and free GFP in ileal epithelial lysates at
121 P7 and P21 confirmed these developmental differences (**Figures 1C and S1C**).

122 In contrast, the proximal intestine displayed a different temporal profile. At P1, both mCherry and free GFP
123 were already present, but their levels progressively declined, and at P14 only low residual signals were
124 detectable. Note that undegraded GFP-LC3 forms (I and II) and intermediate degradation products
125 accumulated at P21, in both distal and proximal samples (**Figure 1B**).

126 Given these observations, we conclude that LREs maintain elevated autophagy levels relative to PECs,
127 most probably as a result of their enhanced lysosomal function. To explore the consequences of autophagy
128 disruption in these cells during early development, we utilised a genetic mouse model. ATG16L1 is crucial
129 for both autophagosome formation and LC3 lipidation, two processes essential for autolysosomal
130 degradation[31,32]. This gene has been extensively studied for its association with inflammatory bowel
131 diseases[6,17]; nonetheless, its specific role in LRE functionality during the neonatal period remains largely
132 unexplored. For this, we crossed with the *Atg16l1*$^{fl/fl}$ mice[33], with mice expressing the *Villin-creER*^{T2}
133 transgene[34]. This breeding strategy generated an *Atg16l1* knockout offspring in which the *Atg16l1* gene is
134 conditionally deleted in the intestinal epithelium upon administration of tamoxifen (*Atg16*cKO) (**Figure 1D**).

135 Initially, we validated our model via WB analysis by measuring the levels of ATG16L1 and LC3 isoforms
136 (cytoplasmic LC3-I and lipidated LC3-II) in the ileum of both WT and *Atg16*cKO mice at P14. We observed
137 a significant reduction in ATG16L1 protein levels across all *Atg16*cKO samples, which led to a
138 corresponding decrease in LC3-II/LC3-I ratio (**Figures 1D and 1E**). Specifically, our data showed an 84.5%
139 reduction in ATG16L1 protein levels and an approximately 8-fold decrease in LC3-II/LC3-I ratio (**Figure 1E**).
140 Furthermore, we observed elevated levels of P62, indicating a reduction in its autophagy-dependent
141 degradation (**Figures 1D and 1E**). These outcomes are consistent with previous results[35].

142 Subsequently, we examined the developmental trajectory of *Atg16*cKO mice, with a primary focus on their
143 intestinal morphology and function. We observed that the mice reached the post-weaning stage (P30)
144 without apparent issues, showing no weight defects throughout early postnatal development (**Figure S2A**).
145 No significant changes were noted in the length or histological state of the small and large intestines
146 (**Figures S2B–S2D**). However, a reduction in villus length and a decrease in the number of Goblet cells
147 (GCs) were detected in the ileum at P14 (**Figures 1F and 1G**), along with mild oedema in the ileum at P30,
148 an indicator of inflammation (**Figure S2D**). Inspired by these observations, we quantified specific intestinal
149 epithelial (IEC) and immune cell subpopulations in the ileum of *Atg16*cKO mice at both neonatal and post-
150 weaning stages using flow cytometry (**Figures S2E and S2F**). For this, we applied specific markers to

151 identify various IEC subtypes, including enterocytes and their progenitors (EC), Goblet cells (GC), Paneth
152 cells (PC), and enteroendocrine cells (EEC)[36] (**Figure S3**, middle row). We also focused on cells related to
153 innate immunity (IIC), such as CD11b+ cells (including NK cells, granulocytes, and
154 macrophages/monocytes), as well as adaptive immunity, encompassing B lymphocytes (B cells) and CD4+
155 T helper cells (Th cells). We observed an increase in IIC and IEC populations during the neonatal period,
156 accompanied by a concurrent decrease in GC and EEC in adult IECs (**Figure S2E**). In contrast, post-
157 weaning samples showed a rise in B cells, stabilization in IIC and IEC levels, an increase in GC, and a
158 decrease in PC and EEC (**Figure S2F**). These results corroborate our histological findings regarding GCs
159 and inflammation.

160 Next, we investigated the effect of autophagy inhibition on the absorption of macromolecules in the ileum.
161 We gaveged rhodamine B–dextran (Rd-dextran) as a probe in *Atg16*cKO and WT mice as controls (**Figure**
162 **1H**). Our analysis differentiated between the apical and basal regions of enterocytes to assess the
163 sequential entry of Rd-dextran, according to the internalization dynamics observed in these cells (**Figure**
164 **S1D**). Confocal microscopy demonstrated that at P7, *Atg16*cKO enterocytes internalized Rd-dextran
165 similarly to WT counterparts. Nevertheless, it is worth noting that in *Atg16*cKO enterocytes, Rd-dextran
166 levels were slightly elevated in the apical region but reduced in the basal region compared to WT (**Figure**
167 **1H**). This observation suggests a deceleration in the internalisation of macromolecules during this
168 developmental period. Subsequently, at P14, *Atg16*cKO enterocytes exhibited a complete abrogation of
169 macromolecule absorption, resembling PECs and indicating an advancement in intestinal maturation
170 (**Figure 1H**). To validate the observed decrease in absorption at P14, we probed neonates from both WT
171 and *Atg16*KO groups with mCherry and quantified the internalised mCherry in the ileum via WB. The results
172 confirmed consistently lower levels of nutrient absorption in *Atg16*KO mice (**Figures 1I and 1J**). Altogether,
173 we conclude that blocking autophagy severely disrupts macromolecule absorption in the neonatal ileum.

174 To further investigate this role autophagy in macromolecule absorption, we examined the expression of the
175 endocytic genes *Dab2*, *Amn*, and *Mamdc4*, as well as the lysosomal genes *Mcoln3*, *Lamp2*, and *Ctsl1*.
176 Previous studies have demostrated the specific role of these genes on the endolysosomal function of
177 LREs[7,12,13]. Indeed, we validated their expression during early postnatal intestinal development (**Figure 2A**).
178 As expected, an upregulation of these genes was observed in distal samples at P7, coinciding with the
179 presence of LREs (**Figure 2A**). Moreover, a proximodistal expression pattern was observed, consistent with
180 the antero-posterior maturation of the intestine[29] (**Figure 2A**).

181 Then, we studied the mRNA expression of *Dab2*, *Mcoln3*, and *Lamp2* genes in both the proximal and distal
182 regions of the small intestines of WT and *Atg16*cKO mice at P7 and P14 (**Figures 2B and S2G**). Since LREs
183 predominantly localise in the distal region, the proximal segment was also analysed to assess potential
184 compensatory mechanisms. In distal *Atg16*cKO samples at P7, mRNA levels of these LRE markers were
185 significantly reduced (**Figure 2B**), while the proximal region showed no significant changes compared to
186 WT mice (**Figure S2G**). By P14, a substantial reduction in gene expression was evident in both proximal

187 and distal *Atg16*cKO mice samples (**Figures 2B and S2G**). Additionally, we analysed *Amn*, *Mamdc4,* and
188 *Ctsl1* mRNA expression in the ileum at P14, finding lower expression levels in the *Atg16*cKO samples
189 (**Figure S2H**).

190 To delve deeper into the protein levels of Dab2, we performed WB and immunofluorescence (IF) analysis
191 in the ileum of *Atg16*cKO mice at P7 and P14. While P7 samples exhibited reduced mRNA expression
192 (**Figure 2B**), Dab2 protein levels remained comparable to WT; however, by P14, a marked reduction in
193 Dab2 was observed in *Atg16*cKO samples (**Figures 2C–2F**).

194 Furthermore, we assess the lysosomal occupancy and content in the apical and basal regions of WT and
195 *Atg16*cKO ileal enterocytes using confocal microscopy with an anti-LAMP1 antibody as a lysosomal marker,
196 as the *Lamp1* and *Lamp2* genes exhibit similar expression patterns (data not shown). Post-weaning (P21–
197 30) WT mice were used as controls. At P7, both WT and *Atg16*cKO enterocytes exhibited comparable
198 lysosomal occupancy and content, with peak intensity observed in both conditions (**Figures 2G and 2H**).
199 However, by P14, while lysosomal occupancy remained similar, *Atg16*cKO enterocytes demonstrated
200 reduced intensity in both the apical and basal regions (**Figures 2G and 2H**). Magnified images also revealed
201 that lysosomes in *Atg16*cKO enterocytes were smaller in P14 neonates, resembling those of PECs (**Figure**
202 **2G**, arrowheads). This reduction in lysosomal content in *Atg16*cKO P14 ileum was further confirmed by WB
203 analysis (**Figures 2I and 2J**).

204 In summary, our results indicate that autophagy plays a crucial role in preserving endolysosomal
205 homeostasis of LREs. Disruption of autophagy in LREs using the *Atg16*cKO mice results in significant
206 defects in macromolecule uptake and lysosomal function, accompanied by the downregulation of key
207 endocytic and lysosomal genes, particularly in the distal ileum of late neonatal mice. These outcomes
208 highlight the importance of autophagy in maintaining LRE function and, consequently, ensuring proper
209 postnatal development. However, the precise mechanisms by which autophagy exerts its effects remain
210 unclear.

211

212 ***LREs show a significant induction of mitophagy to control mitochondrial homeostasis***

213 To elucidate the primary type of autophagy in neonatal enterocytes, we defined the gene expression
214 signature of LREs through bulk RNA sequencing. Leveraging the high levels of macromolecular absorption
215 and autophagy in LREs, we probed neonatal GFP-LC3 mice (P7) with Rd-dextran and isolated LREs from
216 the cellular suspension of the ileum by fluorescence-activated cell sorting (FACS), selecting them as the
217 epithelial cells with high levels of autophagy and Rd-dextran (Rd-dext^{+}GFP^{high}). Moreover, to highlight their
218 genetic neonatal signature, LREs were compared to post-weaning enterocytes (PECs) from mice (P42).
219 Following RNA extraction, we conducted next-generation sequencing (NGS) analysis (**Figures 3A and**
220 **S4A**).

221 We detected a total of 1,537 differentially expressed genes (DEGs), of which 1,036 were upregulated and
222 501 were downregulated in LREs (**Figure 3B**). Differential expression analysis and principal component
223 analysis demonstrated that each population exhibited unique enrichment signatures (**Figures S4B and**
224 **S4C**). The computational method of over-representation analysis (ORA) identified which biological
225 processes were overrepresented in the differentially expressed genes (DEGs)[37]. The majority of
226 differentially regulated pathways were associated with lysosomal function, nutrient absorption, processing,
227 and transport (**Figures 3C, 3D, and S4D**). These findings are consistent with earlier RNA-Seq data from
228 LREs in zebrafish[7]. Nonetheless, the regulation of lipid metabolism pathways differed (**Figure 3C and S4D**),
229 suggesting that mammalian LREs significantly modulate these pathways to process lipids from maternal
230 milk.

231 Among the most upregulated genes were those associated with endocytosis, such as *Mamdc4*, *Dab2*, and
232 *Amn*, as well as lysosome-associated genes like *Mcoln3* and *Ctsl1* (**Figure 3B**). The upregulation of *Dab2*,
233 *Amn*, and *Lamp2* genes corresponded with previously published ileum transcriptome data from mice and
234 zebrafish[7]. Additionally, the overexpression of *Mamdc4* and *Mcoln3* genes also aligned with earlier results
235 in LREs from rodents[12,38]. We confirmed elevated levels of *Ctsl1* mRNA expression and lysotracker staining
236 in LREs compared to PECs in WT mice (**Figures S4E and S4F**), which validated the RNA-Seq data and
237 ensured that the lysosome-associated pathway was not positively regulated due to the selection of neonatal
238 enterocytes with high autophagy levels.

239 Interestingly, the 'positive regulation of autophagy of mitochondrion ' and 'mitochondrial outer membrane'
240 pathways appeared significantly enriched in LREs (**Figures 3C and 3D**). These outcomes, along with the
241 upregulation of several genes involved in mitophagy, such as *Bnip3*, *Atg10*, and *Map1lc3a* (**Figure 3B**)[39,40],
242 indicated that mitophagy is a significant component of the elevated autophagic activity observed in LREs.
243 To explore this hypothesis, we examined the mRNA expression of the canonical mitophagy genes *Prkn*
244 (Parkin) and *Pink1*[41], together with *Bnip3* as a control, in ileal samples from WT mice across developmental
245 stages (E18.5-P42). While *Bnip3* exhibited a progressive decrease in expression throughout development,
246 *Prkn* and *Pink1* showed upregulation in neonatal samples, especially *Prkn* (**Figure 3E**). Moreover, we
247 observed that LREs displayed increased Parkin protein levels compared to PECs through IF (**Figure 3F**).

248 Next, we assessed mitophagy in LREs and PECs using the fixable *mito*-QC reporter C57BL/6J mouse[42],
249 which ubiquitously expresses a chimeric protein consisting of pH-insensitive mCherry, a pH-sensitive GFP,
250 and the mitochondria-targeting sequence (MTS) from the outer mitochondrial membrane protein FIS1
251 (amino acids 101–152). This allowed us to differentiate between cytoplasmic mitochondria ($mCherry^{+}GFP^{+}$)
252 and mitochondria degraded by mitophagy in lysosomes ($mCherry^{+}GFP^{-}$) (**Figure 3G**). Confocal images of
253 LREs revealed a high concentration of red-fluorescent mitochondria inside their endolysosomal system
254 (**Figures 3H and 3I**). In fact, when we inhibited autophagic flux by treating the neonates with the protease
255 inhibitor Leupeptin (40 mg/kg for 16 hours)[43], we observed a significant expansion of LVs and a
256 considerable accumulation of red-only mitochondria within them (**Figure 3H**, arrows; **and 3I**). In contrast,

257 PECs exhibited fewer red mitochondria in lysosomes and a uniform distribution of yellow mitochondria
258 throughout the cytoplasm (**Figures 3H and 3I**).

259 Thus, we confirmed the high mitophagic activity of LREs, suggesting severe impairment of mitophagy and
260 mitochondrial integrity in *Atg16*cKO enterocytes. Indeed, we found that mRNA expression levels of both
261 *Bnip3* and *Prkn* (**Figure 3J**), along with Parkin protein levels (**Figure 3K**), were significantly lowered in
262 neonatal *Atg16*cKO enterocytes. To further investigate the robust mitophagic activity of LREs, we generated
263 an autophagy-deficient *mito*-QC mouse line (*mQ-Atg16*cKO). We observed that in *Atg16*cKO LREs
264 exhibited reduced mitochondrial mass within the lysosomes (**Figures 3L and 3M**), consistent with the low
265 mitophagy observed in PECs (**Figures 3H**, lower panels). Therefore, the suppression of autophagy in LREs
266 results in the downregulation of mitophagy-related genes and a reduced uptake of mitochondria into
267 lysosomes.

268 Motivated by these results, we addressed the mitochondrial status of *Atg16*cKO mice. Using transmission
269 electron microscopy (TEM), we analysed mitochondrial damage, quantity, and morphology in ileal
270 enterocytes from neonatal *Atg16*cKO mice (**Figure 4A–4C**). Mitochondria were categorized into three
271 classes based on electron density, cristae appearance, matrix loss, and outer membrane integrity: class I
272 (normal), class II (partially affected), and class III (damaged) (**Figure 4B**)[44]. For each class, the number,
273 percentage, area, and dimensional ratio (aspect ratio, AR: major axis/minor axis) were quantified (**Figure**
274 **4C**). The data showed that number and percentage of mitochondria within each class were similar across
275 both WT and *Atg16*cKO enterocytes. However, while class I mitochondria in *Atg16*cKO enterocytes
276 exhibited a smaller area and a higher AR, class III mitochondria showed a larger area, suggesting an
277 accumulation of damaged mitochondrial mass due to impaired autophagy (**Figure 4C**).

278 To further validate the mitochondrial status, we performed flow cytometry on neonatal *Atg16*cKO
279 enterocytes using mitochondrial probes *ex vivo*: Mitotracker Green for mitochondrial mass, Mitotracker Red
280 CMXROS for membrane potential, and CM-H_2DCFDA for ROS[36,45]. This analysis confirmed an increase in
281 mitochondrial mass, membrane potential, and ROS in *Atg16*cKO enterocytes (**Figure 4D**). In conclusion,
282 the inhibition of mitophagy in LREs leads to an increased in the mass of dysfunctional mitochondrial.

283 Collectively, mitophagy represents a significant component of the heightened autophagic activity observed
284 in LREs. Its inhibition not only contributes to the mitochondrial defects seen in neonatal *Atg16*cKO
285 enterocytes but may also account for the impairment of their endolysosomal system. These findings
286 highlight a compelling link between the mitochondria-lysosomes crosstalk and neonatal development, as
287 well as the associated metabolic adaptations.

288

289 ***Dysfunction of the mitochondria-lysosome axis in the neonatal epithelium causes an early***
290 ***metabolic switch dependent on BLIMP1 and MAFB***

291 An interesting phenotype observed in neonatal *Atg16*cKO enterocytes was their resemblance to PECs,
292 particularly in terms of the abrogation of macromolecule absorption and the reduction in endolysosomal
293 system functionality. This phenotype could suggest an acceleration of their metabolic transition. At the end
294 of lactation, the mammalian intestine becomes capable of digesting nutrients extracellularly, replaces LREs
295 with PECs (without LVs), and regulates the expression of enzymes to adapt to the new solid diet[3,46].
296 Previous studies have demonstrated that the transcriptional factors BLIMP1, MAFB, and c-MAF (two
297 members of the Maf family of proteins) mediate the metabolic shift in enterocytes during neonatal
298 development[47–49]. At weaning, Blimp1 expression decreases, leading to a downregulation of neonatal
299 enzymes such as β-galactosidase (Glb1) and argininosuccinate synthase 1 (Ass1), and an increase in
300 expression of adult enzymes, including sucrase-isomaltase (Sis), trehalase (Treh), and arginase 2
301 (Arg2)[48,49]. Similarly, early inhibition of MAFB and c-MAF in neonatal intestine induces a comparable
302 metabolic switch [47].

303 Our RNA-Seq analysis comparing LREs and PECs confirmed these dynamics: LREs expressed higher
304 levels of *Mafb*, *Blimp1*, *Glb1*, and *Ass1*, along with a decrease of *Sis*, *Treh*, and *Arg2* (**Figure S5A**). *c-maf*
305 showed no significant differences (**Figure S5A**), though transient regulation at specific neonatal stages
306 cannot be excluded. Consistently, RT-qPCR analysis of proximal and distal small intestine samples from
307 WT mice across development (E18.5–P42) revealed neonatal enrichment of transcription factors and
308 neonatal enzymes, whereas post-weaning samples displayed the opposite profile, with strong induction of
309 adult enzymes (**Figures S5B and S5C**). *Arg2* expression levels closely paralleled those of Sis and Treh
310 (data not shown).

311 To investigate whether autophagy deficiency contributes to this transition, we studied the expression of
312 these metabolic genes in our *Atg16*cKO model. Gene expression analysis revealed a moderate
313 downregulation of the transcription factor genes *Blimp1* and *Mafb*, except for *c-maf*, as well as a more
314 pronounced downregulation of neonatal enzyme genes *Ass1* and *Glb1*. In contrast, there was an
315 upregulation of adult enzyme genes *Treh*, *Sis*, and *Arg2* (**Figure 5A**). Similarly, confocal microscopy
316 analysis revealed reduced levels of MAFB, BLIMP1 (**Figures 5B and 5C**), and ASS1, along with increased
317 levels of TREH in neonatal *Atg16*cKO enterocytes (**Figures 5D and 5E**). This later result was also confirmed
318 by WB analysis in neonates (**Figure 5F and 5G**). In summary, *Atg16*cKO mice advance their metabolic
319 transition in enzymes regulated by MAFB/BLIMP1 in their neonatal epithelium.

320 Next, we studied the metabolic profiles of neonatal enterocytes from *Atg16*cKO mice, in comparison with
321 neonatal and post-weaning WT mice. In order to evaluate deeply the metabolic transition during the
322 neonatal development and the impact of autophagy, we used a pioneer technique called Met-flow. The Met-
323 Flow technique is a flow cytometry-based method that examines the metabolic state of cells by evaluating
324 the levels of rate-limiting enzymes across key metabolic pathways. Specifically, we studied ASS1 and GLS
325 as markers of amino acid (AA) metabolism, HK1 as a marker of glycolysis, CPT1A and ACAC as markers
326 of fatty acid (FA) metabolism, CS and IDH2 for the tricarboxylic acid (TCA) cycle, and ATP5A for oxidative

327 phosphorylation (OXPHOS)[45,50] (**Figure S5D**). Met-Flow analysis revealed higher expression of most
328 metabolic pathways in LREs compared to PECs (**Figure S5E**), reflecting a their hyperconsumptive signature
329 aligned with the high energy demands of this developmental period[51]. Notably, neonatal *Atg16*cKO
330 enterocytes exhibited a moderate reduction in enzyme protein levels, positioning them between those of
331 WT neonates and post-weaning mice (**Figure 5H**). This intermediate profile is indicative of a globally
332 accelerated metabolic transition toward a more adult state.

333 In summary, our results reveal that autophagy is essential for coordinating mitochondrial and metabolic
334 remodeling during neonatal ileum development and the weaning transition. Suppression of autophagy
335 perturbs endolysosomal and mitochondrial integrity, thereby altering the transcriptional control of LREs.
336 Consequently, LREs undergo a premature metabolic switch, marked by MAFB and BLIMP1 dysregulation
337 and reduced activity of key metabolic pathways.

338

339 ***Mitochondrial homeostasis is critical for maintaining LREs function and their metabolic transition***

340 After identifying mitochondrial homeostasis defects as a downstream consequence of impaired
341 endolysosomal function in the *Atg16*cKO model, we next investigated whether mitochondria themselves
342 play an intrinsic role in sustaining LRE integrity. For this purpose, we used the *Tfam*cKO mouse model
343 (*Tfam*$^{fl/fl}$*/Villin-creER*^{T2}), which enables inducible deletion of Tfam in the neonatal intestinal epithelium. This
344 approach allowed us to directly test whether mitochondrial dysfunction is sufficient to compromise
345 lysosomal homeostasis in LREs.

346 TFAM is a transcription factor that regulates the transcription and replication of mitochondrial DNA
347 (mtDNA)[52]. While the role of mitochondria in maintaining intestinal homeostasis has been extensively
348 explored[24], and the consequences of Tfam deletion have been reported in both embryonic and adult
349 intestinal epithelium[53], its specific contribution during the neonatal stage, and particularly in nutrient
350 absorption and processing by LREs, remains unexplored.

351 We first characterized the general phenotype of *Tfam*cKO pups during the neonatal period. These mice
352 exhibited developmental defects, a generally poor appearance, and significantly reduced body weight,
353 starting around P8, which ultimately compromised their survival and prevented successful weaning (**Figures**
354 **6A–6C**). Given the severity of the phenotype and in adherence with animal welfare guidelines, euthanasia
355 was performed after two consecutive days without weight gain or upon observing weight loss of around
356 10% (**Figure 6C**). Based on the timing of euthanasia, we defined two experimental groups: mice euthanised
357 between P9–P11 (hereafter referred to as P10), and those euthanised between P13–P15 (hereafter
358 referred to as P14). In the ileum of both groups, we confirmed a marked reduction in *Tfam* mRNA expression
359 (**Figure 6D**), accompanied by decreased levels of mtDNA, as assessed through the quantification of
360 electron transport chain-encoded genes including *mt-Nd1*, *mt-Co*1, *mt-Co2*, and *mt-Atp6* (**Figure S6A**). In
361 addition, *Tfam* deletion resulted in a selective loss of mitochondrial gene expression at P10 (*mt-Nd1*, *mt-*

362 *Co2*), while nuclear *Sdha* expression was unaffected (**Figure S6B**). We also observed a significant reduction
363 in MTCO1 (complex IV subunit) protein levels in ileal sections of *Tfam*cKO at P14 (**Figures S6C and S6D**).
364 These results validated our neonatal *Tfam*cKO model and were consistent with findings from other *Tfam*KO
365 models[45,54,55].

366 Further histological examination of the distal small intestine of *Tfam*cKO mice at P10 and P14 revealed
367 substantial structural alterations. The epithelium exhibited clear signs of disorganization and inflammation,
368 characterised by notably shorter, malformed villi, oedema, reduced GCs, and a thicker submucosa and
369 lower mucosa (**Figures S6E–S6H**). Enterocytes also exhibited aberrant vacuoles, suggesting dysfunctions
370 in nutrient processing (**Figure S6E**, arrows).

371 Moreover, flow cytometry analysis of the ileum at P10 and P14 revealed increased percentages of IIC (B
372 cells, and Th cells) in *Tfam*cKO samples (**Figures S6I–S6K**). Given the elevated OXPHOS activity
373 characteristic of intestinal stem cells (ISCs)[56], we assessed ISC populations in ileal sections from P10 and
374 P14 *Tfam*cKO mice via Olfm4 immunofluorescence (**Figure S6L**, arrows), which revealed a marked
375 reduction in Olfm4^{+} crypts (**Figures S6M**). Additionally, lysozyme staining showed a striking increase in
376 mislocalised PCs (**Figures S6N and S6O**). These PCs exhibited mislocalization, aberrant morphologies and
377 enlarged granules, indicative of disrupted crypt architecture and compromised ISC niche homeostasis
378 (**Figure S6N**, arrowheads).

379 With the systemic and intestinal phenotypes of *Tfam*cKO mice defined, we next investigated how loss of
380 TFAM affects mitochondrial homeostasis in LREs. Firstly, mitochondria from *Tfam*cKO enterocytes at P10
381 and P14 were analyzed by TEM, following the same approach previously used in *Atg16*cKO mice. At P10,
382 *Tfam*cKO enterocytes displayed more class I and II mitochondria, with reduced area and AR (**Figures 6E,
383 6F, and S6P**). By P14, damaged class III mitochondria increased while class I mitochondria decreased in
384 number, size, shape and AR (**Figures 6E, 6F, and S6P**). This progressive mitochondrial damage resembles
385 that observed in a previously described *Tfam*KO model in renal epithelial cells[55]. These data were
386 corroborated by subsequent flow cytometry analysis, which revealed increased mitochondrial mass,
387 membrane potential, and ROS levels in neonatal *Tfam*cKO enterocytes (**Figure 6G**), features reminiscent
388 of those observed in TFAM-deficient lymphocytes[45,54].

389 In summary, deletion of *Tfam* in the neonatal intestinal epithelium severely disrupted mucosal structure and
390 function, leading to developmental defects that culminated in early mortality. Specifically, in LREs, TFAM
391 loss caused the accumulation of damaged mitochondria and increased oxidative stress.

392 We next investigated whether mitochondrial dysfunction could similarly drive an accelerated metabolic
393 transition in neonatal enterocytes, as observed in the *Atg16*cKO model. The microscopy analysis indicated
394 a reduction in the expression levels of BLIMP1 and MAFB, with a more pronounced decrease in BLIMP1
395 (**Figures 6H and 6I**). As a result, we also observed lower levels of ASS1 and elevated expression of TREH
396 in the *Tfam*cKO enterocytes (**Figures 6J and 6K**). These results were further supported by gene expression
397 analyses of metabolic transition genes that are regulated by BLIMP1, MAFB, and c-MAF. We obtained a

398 progressive downregulation of *Mafb*, *c-maf*, *Blimp1*, *Ass1,* and *Glb1*, accompanied by an upregulation of
399 *Treh*, *Sis*, and *Arg2* at P14 (**Figure S7A**). Finally, the activity of key metabolic pathways was assessed in
400 neonatal *Tfam*cKO enterocytes using Met-Flow[45,50], revealing a marked reduction in nearly all metabolic
401 proteins, except for ATP5A (**Figure 6L**), which was increased, possibly due to mitochondrial accumulation
402 or as a compensatory response to mitochondrial dysfunction. Taken together, these findings indicate that
403 neonatal *Tfam*cKO enterocytes undergo a premature metabolic transition, resembling the metabolic profile
404 of PECs.

405 Following the analysis of mitochondrial defects in *Tfam*cKO neonatal enterocytes, we next investigated
406 whether impaired mitochondrial function also perturbs the endolysosomal system of LREs. Although
407 lysosome–mitochondria crosstalk has been predominantly characterized in the context of mitophagy, our
408 findings suggest a reciprocal layer of regulation, whereby mitochondria control lysosomal biogenesis and
409 function. This bidirectional communication implies that mitochondrial dysfunction not only disrupts energy
410 metabolism but also secondarily compromises lysosomal integrity, thereby exacerbating the metabolic and
411 endolysosomal defects observed in neonatal *Atg16*cKO enterocytes. Indeed, neonatal *Tfam*cKO
412 enterocytes exhibited a complete loss of Rd-dextran uptake (**Figures 6M and 6N**) and a progressive
413 downregulation of the endocytic genes *Dab2*, *Amn*, and *Mamdc4* (**Figures S7B–S7D**). Subsequently, we
414 characterised a gradual reduction in the expression of lysosomal genes *Lamp2*, *Mcoln3*, and *Ctsl1* (**Figure**
415 **S7E**), accompanied by a decrease in lysosomal content and size (**Figures 6M, 6O, S7F and S7G**). Thus,
416 neonatal *Tfam*cKO enterocytes recapitulated the phenotype observed in the *Atg16*cKO model, validating a
417 reciprocal interaction between mitochondria and lysosomes in LREs.

418 In conclusion, the *Tfam*cKO model enabled us to establish a bidirectional relationship between mitochondria
419 and lysosomes by recapitulating the endolysosomal defects observed in autophagy-deficient neonatal
420 enterocytes. Furthermore, we confirmed that mitochondrial and lysosomal dysfunction drive an early
421 metabolic switch in LREs. These alterations, alongside epithelial inflammation, developmental delay, and
422 premature death, position the *Tfam*cKO model as a valuable tool for investigating the pathophysiology of
423 childhood malnutrition.

424

425 ***Antioxidant activity in LREs modulates the onset of metabolic switch***

426 After defining the metabolic switch underlying neonatal development, and the early metabolic switch in both
427 *Atg16*cKO and *Tfam*cKO models, we focused on uncovering the mechanisms responsible for this
428 phenotype. The observation that our gene-deficient mice presented heightened ROS levels in enterocytes
429 (**Figures 4D and 6G**) suggested that redox dysregulation may underlie their accelerated metabolic
430 transition. Indeed, the high mitophagic activity observed in LREs may contribute to the control of ROS[19,20].
431 Previous studies have shown that oxidative stress has been reported to repress *c-maf* expression[57] and

that antioxidant treatment can induce *Blimp1* expression[58]. Therefore, we hypothesise ROS regulation could represent a critical mechanism for controlling the timing of the metabolic transition in LREs.

We found that LREs exhibited significantly higher levels of mitochondrial ROS (mROS) compared to PECs (**Figure 7A**), possibly reflecting their elevated OXPHOS activity[59]. In contrast, total ROS levels were lower in LREs than in PECs (**Figure 7A**), indicating the presence of mechanisms that tightly regulate oxidative stress.

Then, we further explored our LREs vs PECs RNA-Seq dataset analysis to identify additional pathways involved in ROS regulation. Numerous pathways related to ROS, ROS response, and antioxidant activity stood out (**Figure 7B and 7C**). Further, there was an overexpression of genes for the antioxidant enzymes Glutathione Peroxidase-3 (Gpx3) and Catalase (Cat) (not shown), suggesting that these antioxidants could be reducing ROS levels in LREs. Indeed, we observed that neonatal ileal samples showed induction of *Gpx3* and *Cat* expression compared to the embryo and post-weaning ileal samples, with the most drastic changes in *Gpx3* (**Figure 7D**). Moreover, in both *Atg16*cKO and *Tfam*cKO neonates, *Gpx3* and *Cat* expression were significantly decreased in the ileum (**Figure 7E and 7F**), and GPX3 protein levels were likewise reduced, as shown by IF (**Figure 7G-J**). Thus, oxidative stress may act as a trigger for the metabolic transition in LREs. To validate this hypothesis, neonatal mice were treated with hydrogen peroxide (H_2O_2) to induce oxidative stress[60]. mRNA expression analysis revealed a downregulation of the transcription factors *Blimp1*, *Mafb*, and *c-maf*, alongside an upregulation of adult enzymes such as *Treh* and *Arg2*. However, the expression of neonatal enzyme genes *Ass1* and *Glb1* remained unchanged (**Figure 7K)**. Subsequently, we characterised a reduction of BLIMP1 and ASS1 levels by both IF and flow cytometry (**Figure 7L–7N**), while TREH expression was found to be increased (**Figure 7L and 7M**).

The data collectively suggest that elevated antioxidant activity is a key characteristic of LREs. When this antioxidant function is compromised in neonatal *Atg16*cKO and *Tfam*cKO enterocytes, alongside mitochondrial dysfunction, the oxyidative stress rise. This increase in ROS contributes to the repression of genes such as *Blimp1*, *Mafb*, and *c-maf*, ultimately triggering an early metabolic transition (**Figure 7O**). Therefore, this study emphasizses the critical role of mitochondrial-lysosomal coordination in mitigating oxidative stress and regulating the transcriptional programs essential for neonatal intestinal development. Additionally, it paves the way for future research into therapeutic strategies aimed at restoring mitochondria-lysosome homeostasis and redox balance in early gut disorders.

DISCUSSION

In this work, we have elucidated new molecular mechanisms fundamental to the function and differentiation of mammalian LREs, highlighting the role of the mitochondria-lysosome axis. Disruption of autophagy in the neonatal gut, either through *Atg16*cKO or mitochondrial dysfunction via *Tfam*cKO, resulted in defective nutrient absorption and a reduction in lysosomal content. Most importantly, *Tfam*cKO neonates exhibited

467 weight loss and premature death, resembling hallmarks of infant malnutrition. Notably, the early enzymatic
468 maturation of *Atg16*cKO and *Tfam*cKO enterocytes indicates a direct connection between autophagic and
469 mitochondrial processes in enterocytic maturation. Additionally, the associated increase in ROS observed
470 in both models may contribute to this metabolic switch by suppressing the expression of transcription factors
471 BLIMP1, MAFB, and c-MAF. These findings are consistent with our transcriptomic data, which reveal
472 upregulation of mitophagy- and antioxidant-related pathways in LREs compared to PECs, supporting the
473 concept that mitochondrial quality control and redox homeostasis are defining features of LRE identity and
474 function. Taken together, our outcomes offer interesting mechanistic insights into the mitochondria-
475 lysosome crosstalk and its role in postnatal intestinal physiology, with implications for understanding the
476 pathophysiology of neonatal malnutrition and related disorders.

477 Autophagy and endocytosis are vesicle-mediated pathways that converge at the lysosome to degrade and
478 recycle intra- and extracellular components. These processes intersect at multiple stages (vesicle
479 formation, trafficking, and fusion) and share several key regulators. Mounting evidence indicates reciprocal
480 dependence between these processes[25,61]. Using GFP-LC3 mice, we demonstrated that neonatal ileal
481 samples exhibit increased autophagosome degradation compared to post-weaning counterparts (**Figures**
482 **1A–1C and S1C**). Consistently, *Atg16*cKO neonates displayed impaired absorption (**Figures 1H–1J**) and
483 showed reduced expression of crucial endocytic genes characteristic of LREs (**Figures 2B–2F, S2G and**
484 **S2H**). Moreover, *Atg16*cKO neonatal enterocytes displayed reduced lysosomal size and content (**Figures**
485 **2G–2J**), along with downregulation of key lysosomal genes (**Figures S2G and S2H**). These outcomes reveal
486 a functional interplay between autophagy and the endolysosomal system in LREs.

487 Despite these endolysosomal defects, *Atg16*cKO mice reached the post-weaning stage without apparent
488 physiological abnormalities, aside from mild signs of intestinal inflammation (**Figures S2A–S2D**). This
489 observation aligns with findings in mice lacking the lysosomal cation channels Mucolipin-1 and -3 (Mcoln1
490 and Mcoln3), which also exhibit pronounced endolysosomal abnormalities in neonatal enterocytes but
491 develop into phenotypically normal adults[12]. Together, these results suggest that endolysosomal and
492 autophagic processes primarily affect LREs. Accordingly, once the neonatal period concludes and LREs
493 are replaced by PECs, the phenotype becomes attenuated or fully resolves. However, further investigations
494 will be needed to assess intestinal physiology and metabolism in adult *Atg16*cKO mice comprehensively.

495 We characterized a significant increase in autophagic activity in LREs as primarily due to the lysosomal
496 degradation of mitochondria, a process known as mitophagy. Indeed, mitophagy-related genes exhibit a
497 higher expression in neonatal ileum compared to post-weaning samples (**Figures 3B–3F**). Correspondingly,
498 neonatal *mito*-QC mice[42] demonstrated enhanced mitochondrial degradation within the LVs of LREs
499 compared to PECs (**Figures 3H and 3I**). Furthermore, this process was inhibited either by leupeptin
500 treatment[43] (**Figures 3H and 3I**) or through genetic ablation of autophagy (*Atg16*cKO) (**Figures 3L and 3M**),
501 confirming the dependence of mitochondrial clearance on lysosomal-autophagic activity. Consistent with
502 this, neonatal *Atg16*cKO enterocytes accumulated dysfunctional mitochondrial mass (**Figure 4**).

503 Specifically, these cells showed an increase in the area of damaged mitochondria (class III), whereas
504 healthy mitochondria (class I) exhibited a smaller area but an increased aspect ratio (**Figures 4A–4C**).
505 These differences possibly reflect not only mitophagy blockade but also alterations in mitochondrial
506 dynamics, such as enhanced fusion or reduced fission, which are aimed at preserving oxidative
507 phosphorylation (OXPHOS) capacity[62]. Future studies should investigate the expression of proteins
508 involved in mitochondrial fusion and fission in the *Atg16*cKO model to define better the molecular landscape
509 that integrates mitochondrial dynamics with mitophagy in LREs.

510 After identifying mitochondrial homeostasis defects secondary to impaired endolysosomal function in the
511 *Atg16*cKO model, we next investigated the reverse relationship by directly disrupting mitochondrial function
512 using the *Tfam*cKO model. *Tfam*cKO neonates exhibited severe growth impairment and premature death
513 (**Figures 6A–6C**), and their enterocytes accumulated markedly damaged mitochondria (**Figures 6E–6G and**
514 **S6P**). These mice also reproduced key features of the *Atg16*cKO phenotype, including loss of uptake
515 capacity, reduced lysosomal content, and downregulation of endolysosomal genes (**Figures 6M–6O and**
516 **S7B–S7G**). Interestingly, these lysosomal defects differ from what has been observed in *Tfam*-deficient T
517 and B lymphocytes, where dysfunctional acidic lysosomal compartments are expanded[45,54]. In neonatal
518 enterocytes, however, Tfam deletion results in diminished lysosomal size and content, highlighting that
519 mitochondria–lysosome interactions are highly cell-type specific. Beyond this bidirectional crosstalk, our
520 data raise the possibility of a retrograde signalling mechanism. Mitochondria are increasingly recognized
521 as signalling hubs that influence nuclear transcriptional programs, as shown in immune cells. In LREs, two
522 interconnected processes may be at play: first, endolysosomal-mediated nutrient internalization, which is
523 defective in both *Atg16*cKO and *Tfam*cKO models; and second, mitophagy-driven mitochondrial
524 degradation, which provides retrograde signals to the nucleus. This latter pathway could be essential for
525 controlling the transcriptional networks that govern the metabolic switch (via BLIMP1 and MAFB) and for
526 sustaining lysosomal functionality itself. In this view, lysosomes must degrade mitochondria not only to
527 preserve organelle quality control but also to control the transcriptional reprogramming required for the
528 neonatal-to-adult metabolic transition.

529 At weaning, the mammalian intestine undergoes a shift to extracellular nutrient digestion and adjusts its
530 enzymatic profile to meet the metabolic demands of a carbohydrate-rich solid diet[3]. At the same time, LREs
531 are replaced by PECs lacking large lysosomal vacuoles[46]. The transcription factors BLIMP1 (PRDM1),
532 along with MAFB and c-MAF (both members of the Maf protein family) have been positioned as central
533 repressors of this switch. Neonatal mice lacking these transcription factors in the intestinal epithelium
534 exhibited impaired nutrient absorption, early downregulation of neonatal enzymes, and upregulation of adult
535 counterparts, ultimately leading to developmental defects[47–49]. Furthermore, our research demonstrated
536 that dysfunctions in autophagic, lysosomal, and mitochondrial processes in LREs —induced by the deletion
537 of *Atg16l1* and *Tfam*— led to a repression of these transcription factors, resulting in similar phenotypes
538 (**Figures 1H, 5, 6H–6N and S7A**).

539 We further analysed the activity of core metabolic pathways in WT, *Atg16*cKO, and *Tfam*cKO neonatal
540 enterocytes, comparing them to PECs (**Figures 5H, 6L, and S5E**). This analysis revealed a moderate
541 reduction in metabolic activity in *Atg16*cKO cells and a more noticeable decline in *Tfam*cKO enterocytes,
542 suggesting a shift toward an adult-like metabolic state. These findings contrast with previous transcriptomic
543 data from neonatal mice lacking MAFB and c-MAF, which reported an upregulation of OXPHOS and fatty
544 acid degradation pathways[47]. However, that study did not include a direct comparison to PECs, leaving
545 open the possibility of compensatory mechanisms. In this context, our results may provide a more accurate
546 reflection of the metabolic trajectory during neonatal-to-adult transition and its dependence on the
547 mitochondria-lysosome axis.

548 We have defined the metabolic evolution of enterocytes during neonatal development beyond the genes
549 classically associated with the transcription factors BLIMP1, MAFB, and c-MAF, and established a
550 functional link between this transition and the maintenance of lysosomal and mitochondrial homeostasis.
551 At the same time, our data reinforce the idea that, in enterocytes, genetic programs prevail over the sensing
552 of external cues: despite the neonatal context (milk-based diet, reduced microbiota, and limited immune
553 activation)[63], the repression of these transcription factors leads to inevitable epithelial maturation. Yet, the
554 cellular mechanisms that regulate these genetic pathways still need to be clarified.

555 Reactive oxygen species (ROS) are oxygen-derived molecules that play a crucial role in various cellular
556 processes, including energy production, mitochondrial signalling, and cell differentiation[64,65]. Their
557 intracellular levels are tightly regulated through multiple mechanisms: the mitochondrial electron transport
558 chain constitutes a major source of ROS, while antioxidant enzymes serve as key systems for neutralizing
559 their excess[59,64,65]. In the intestine, ROS have been primarily associated with more differentiated epithelial
560 cells exhibiting higher OXPHOS activity[24]. However, their role in epithelial maturation during neonatal
561 intestinal development continues to be unexplored.

562 Our results indicate that LREs display a transcriptional signature consistent with elevated antioxidant
563 activity, possibly as a compensatory mechanism to counteract high levels of mitochondrial ROS resulting
564 from hyperactivated OXPHOS (**Figures 7A–7D**). Beyond this homeostatic role, recent studies suggest that
565 this antioxidant signature may also be linked to the repression of transcription factor genes *Blimp1*, *Mafb*,
566 and *c-maf*, and consequently, to the maintenance of LRE identity and function. The antioxidant vitamin
567 ascorbic acid has been shown to increase the expression of Blimp1 in B lymphocytes through the activity
568 of DNA demethylases TET2 and TET3[58]. Conversely, treatment with H_2O_2 decreases the expression of *c-*
569 *maf*, whereas the ROS scavenger N-acetyl cysteine (NAC) can restore its levels in human adipose tissue-
570 derived mesenchymal stem cells[57].

571 This hypothesis is further supported by the elevated ROS levels and the loss of the antioxidant signature
572 observed in our knockout models (**Figures 4D, 6G, 7E–7J**), as well as by our experiments in which H_2O_2
573 treatment of neonatal WT mice accelerated the metabolic transition of enterocytes (**Figures 7K–7N**).
574 Together, these outcomes suggest that both ROS levels and ROS-regulated genetic programs actively

575 shape epithelial differentiation and metabolic programming in the neonatal intestine (**Figure 7O**). This may
576 represent a physiological mechanism to prevent premature transitions until the tissue is developmentally
577 prepared. In this context, therapeutic strategies aimed at fine-tuning redox homeostasis could offer a
578 powerful approach to supporting neonatal intestinal health.

579 In addition to their role in nutrient absorption, LREs may act as immunometabolic sentinels during the
580 neonatal period, integrating microbial cues and intracellular metabolic status to modulate immune
581 responses. Due to their high endolysosomal activity, LREs could internalise and process luminal antigens,
582 including microbial components, thereby contributing to the development of the intestinal immune system[66].
583 In line with this, our RNA-Seq analysis revealed multiple differentially regulated immune-related pathways
584 (data not shown).

585 Disruption of lysosomal and mitochondrial homeostasis in *Atg16*cKO and *Tfam*cKO mice likely impairs
586 these immune functions, as suggested by the inflammatory status observed in both models (**Figures S2D–**
587 **S2F, S6E, and S6H–S6K**). In fact, mice with autophagy defects also exhibit gut microbiota alterations and
588 immune dysregulation[17]. Furthermore, cytosolic mtDNA resulting from mitochondrial damage due to TFAM
589 deficiency has been shown to activate the cGAS–STING inflammatory pathway[55], while mitophagy
590 induction, along with improved mitochondrial status, attenuates this response[43]. Additionally, *c-maf* KO
591 mice exhibit changes in intraepithelial lymphocytes and microbiota composition[67], suggesting that genetic
592 programs involved in epithelial maturation, affected in our KO models, may be tightly linked to intestinal
593 immune and microbial homeostasis.

594 Given the immunometabolic imbalance observed in *Atg16*cKO and *Tfam*cKO neonates, it is plausible that
595 these models experience alterations in their gut microbiota. These changes may not only reflect enterocytic
596 dysfunction but could also actively contribute to the phenotype by disrupting microbial-derived cues
597 essential for LRE maintenance and programming. Future studies involving microbiota profiling and
598 transplantation will help determine whether restoring a balanced microbial ecosystem can rescue LRE
599 function.

600 Finally, the potential microbiota alterations described above, together with the inflammation and oxidative
601 stress observed in our KO models, suggest parallels with known hallmarks of children's malnutrition
602 disorders. Particularly, *Tfam*cKO mice display a more pronounced phenotype and marked developmental
603 defects, resembling features of Kwashiorkor, a severe form of protein deficiency prevalent in low-income
604 settings [68,69]. This redox imbalance—marked by low antioxidant levels and increased ROS—in our KO
605 models closely mirrors that seen in malnourished children, and may contribute to the broader clinical
606 phenotype of undernutrition[68]. Accordingly, pilot studies have demonstrated that antioxidant
607 supplementation may provide therapeutic benefit in conditions such as Kwashiorkor[70]. Moreover, our H_2O_2
608 treatment experiments, which replicated the epithelial maturation phenotype characterized in our gene-
609 deficient mice, might similarly induce nutritional, microbial, and inflammatory disturbances. Indeed,
610 intestinal tissues from H_2O_2-treated neonates displayed signs of inflammation (data not shown).

611 Collectively, these considerations suggest that malnourished children may also experience premature
612 intestinal maturation and highlight the need for deeper investigation into antioxidant therapies as potential
613 interventions. Furthermore, our KO models may serve as valuable experimental platforms to investigate
614 the mechanisms underlying neonatal malnutrition and to explore interesting avenues for its treatment.
615 Altogether, future studies aimed at restoring LRE mitophagy and metabolism, as well as modulating the
616 redox balance, could yield promising strategies to counteract the devastating consequences of malnutrition-
617 related disorders in early life.

618 In conclusion, our study uncovers novel mechanisms underlying the function and metabolic transition of
619 neonatal enterocytes. We demonstrate that lysosomal and mitochondrial homeostasis is indispensable for
620 efficient nutrient absorption and for sustaining the high metabolic activity required during this energy-
621 demanding stage of life. Further investigation of the mitochondria-lysosome axis in LREs will not only
622 advance our understanding of neonatal intestinal physiology but also contribute significantly to the
623 development of targeted interventions against childhood malnutrition.

624

625 ***Limitations of the study***

626 This work demonstrates that neonatal intestinal deficits in autophagy and mitochondrial homeostasis lead
627 to endolysosomal dysfunction in enterocytes, impairing development and ultimately triggering inflammation
628 and early lethality. However, since we used *Villin-cre*-based models, where gene deletion occurs in all
629 intestinal epithelial cells, we cannot exclude their contribution to the observed phenotypes. Indeed, we
630 detected altered abundance and morphology of these cells in both *Atg16*cKO (**Figures 1F, 1G, and S2E–**
631 **S2F**) and *Tfam*cKO mice (**Figures S6G, S6L–S6O**). Previous studies support this interpretation: defects in
632 GCs and PCs are linked to intestinal inflammatory diseases[71,72], and intestinal autophagy loss has been
633 associated with increased oxidative stress in ISCs[36], which could partially explain the elevated ROS levels
634 in *Atg16*cKO enterocytes (**Figure 4D**). Similarly, *Tfam* deletion in the adult intestinal epithelium causes ISC
635 loss and lethality[53], suggesting that depletion of ISCs may contribute to the early death of neonatal
636 *Tfam*cKO mice, limiting our ability to study mitochondrial function in enterocytes at later developmental
637 stages.

638 To address these limitations, we plan to develop an LRE-specific tamoxifen-induced conditional knockout
639 model to target critical genes specifically in neonatal enterocytes. Although selectively targeting neonatal
640 enterocytes would yield a more precise model, this is hindered by the lack of fully specific promoters and
641 the technical difficulty of isolating and culturing LREs, which are highly sensitive to dissociation-induced cell
642 death. To overcome these challenges, we are also studying *in vitro* systems that recapitulate the properties
643 of LREs and may serve as a platform for future functional validation.

644

645 **RESOURCE AVAILABILITY**

646 ***Lead contact***

647 Further information and requests for resources and reagents should be directed to and will be fulfilled by
648 the lead contact, Fernando Martin-Belmonte (fmartin@cbm.csic.es).

649 ***Materials availability***

650 This study did not generate new unique reagents.

651 ***Data and code availability***

652 RNA-seq Illumina paired-end reads (FASTQ) generated for this study are available at the European
653 Nucleotide Archive (ENA; http://www.ebi.ac.uk/ena/) under the study accession number PRJEB46511.

654

655 **ACKNOWLEDGMENTS**

656 We thank Carmen M. Ruiz-Jarabo for her comments on the manuscript and members of the Martin-
657 Belmonte and Martinez-Martin labs for their support and helpful discussions. This work was supported by
658 MICINN (BFU2017-83243-P; PID2020-120367GB-I00; PID2023-151844OB-I00; RED2022-134927-T),
659 Fondos FEDER investigación (Horizon-MSCA-2022-DN-101119504**)** and Fundación Ramon Areces
660 (CIVP18A3904). HR22-00447 from ¨La Caixa¨, RTI2018-101586-A-I00, PID2021-126298OB-100 to N.M.-
661 M. G.H. and M.I.-P. were supported by FPI fellowships BES-2018-077789 and PRE2019-089076,
662 respectively, funded by the Spanish Ministry of Science and Innovation and the State Research Agency
663 (MCIN/AEI /10.13039/501100011033). D.A.L was supported by FPU and JAE fellowships FPU23/03569
664 and JAEINT_22_01549. L.A was supported by Horizon-MSCA-2022-DN -101119504. I.G.G. was funded
665 by the Medical Research Council, UK (MC_UU_00038/2). We thank Victor Lazaro Morato (currently at IMN-
666 CNM, CSIC, Madrid, Spain) for his contribution to the initial analyses of the general phenotype and
667 mitochondrial status by TEM in the *Tfam*cKO model. We acknowledge Michel Bagnat (Duke University,
668 USA) for the generous donation of mCherry plasmid, and Juan M. Serrador, Catalina Grabowski and
669 Dionisio Ureña (CBM), for their essential contribution to the protocol for the growth and purification of
670 mCherry plasmid. We are thankful to the Animal, Flow Cytometry, Advanced Optical Microscopy, and
671 Electron microscopy facilities at the CBM, as well as the Histology Service at the Centro Nacional de
672 Biotecnologia (CNB, CSIC, Madrid, Spain), for their excellent technical support. We acknowledge the
673 Centro de Análisis Genómico (CNAG-CRG, Barcelona, Spain) for the RNA sequencing, and to
674 Biocomputational Analysis Core Facility at the CBM, specially to Sandra González de la Fuente, for the
675 NGS data analysis and plotting. We thank the computational resources and support provided by the Centro
676 de Computación Científica at Universidad Autónoma de Madrid (CCC-UAM).

677 Certain Figures were inspired by or adapted from previously published sources, some of which are licensed
678 under Creative Commons (CC BY 4.0) (https://creativecommons.org/licenses/by/4.0/). While every effort
679 has been made to credit original sources, any omissions are unintentional and will be corrected in future
680 revisions if identified. Some figures were created with BioRender.com.

681

682 **DECLARATION OF INTERESTS**

683 The authors declare no competing interests.

684

685 **FIGURE TITLES AND LEGENDS**

686 **Figure 1. High Autophagic Activity of LREs Is Required for Nutrient Absorption**

687 **(A and B)** Assessment of autophagic flux and protein absorption along the small intestine of GFP-LC3 mice
688 during postnatal development. GFP-LC3 mice at postnatal days (P) 1, 7, 14, and 21 were orally gavaged
689 with mCherry and sacrificed 3 hours later (n = 3) (A). Proximal and distal intestinal segments were harvested
690 (A), and epithelial cell lysates analysed by immunoblotting for mCherry and GFP-LC3 isoforms (B). The
691 representative western blot in (B) distinguishes cytosolic LC3-I, membrane-bound LC3-II, and cleaved "free
692 GFP," a marker of autolysosomal degradation. The pink rectangle highlights mCherry and free GFP in
693 distal-P7, indicating maximal protein uptake and autophagic degradation. USP7, loading control. Figure 1A
694 includes images adapted from Birchenough et al.[73] (CC BY 4.0) and Zhao et al.[74], and the GFP-LC3
695 isoforms scheme is based on Ni et al.[28].

696 **(C)** Quantification of mCherry and free GFP levels in lysates of ileal epithelial cells from P7 (n = 4) and P21
697 (n = 5) GFP-LC3 mice. Data derived from Figure S1C.

698 **(D and E)** Generation and validation of *Atg16l1* intestinal knockout (*Atg16*cKO) mice. Ileal epithelial cell
699 lysates from WT and *Atg16*cKO P14 mice were immunoblotted for ATG16L1, LC3, and P62 (D). (E)
700 Quantification of ATG16L1 (n = 5,6) and P62 (n = 6,7), and LC3-II/LC3-I ratio (n = 17). In ATG16L1 and
701 P62 graphs, data relative to WT.

702 **(F and G)** Ileal architecture in *Atg16*cKO neonates. Periodic acid-Schiff (PAS)-haematoxylin staining of P14
703 ileal sections from WT and *Atg16*cKO mice (F) shows villus shortening (double red arrow) and a decrease
704 in goblet cells (PAS+, arrowheads) in *Atg16*cKO sections (n = 3). L, lumen; scale bar, 100 μm. (G)
705 Quantification of villus length and goblet cells per villus. Dots represent individual villi (n = 30 villi from 3
706 mice; 10 villi per mouse).

707 **(H)** Confocal analysis of Rd-dextran uptake in ileal *Atg16*cKO enterocytes. WT and *Atg16*cKO neonates at
708 P7 (early) and P14 (late), and post-weaning (P21–30) WT mice were gavaged with rhodamine B–dextran
709 (Rd-dext, red) 16 hours prior to sacrifice (n = 3). Ileal sections labelled with β-catenin (βcat, white) and DAPI
710 for DNA (blue). Dashed-line squares indicate magnified areas. Arrows point to lysosomal vacuoles;
711 arrowheads, apical endosomes. L, lumen. Scale bars: 10 μm (main); 5 μm (insets). Dot plot shows the
712 quantification of Rd-dextran intensity (integrated density) in the apical and basal regions of enterocytes.
713 Dots represent individual enterocytes (n = 25–40).

714 **(I and J)** *Atg16*cKO mice show impaired mCherry absorption. P14 mice were gavaged with mCherry and
715 ileal epithelial cell lysates collected 16 hours later for immunoblotting (I). Actin, loading control. (J)
716 Quantification of mCherry signal, normalised to WT (n = 9,11).

717 In (C, E, J), dots represent individual mice and charts depict mean + SEM. In (G, H), dot plots show mean
718 ± SEM (black lines).

719 (C, E, G): Student's t-test (mCherry, ATG16L1, P62, villus length) and Mann–Whitney test (free GFP, LC3
720 ratio, goblet cells/villus). (J): Mann–Whitney test. (H): Kruskal–Wallis test; only statistically significant
721 comparisons between WT and *Atg16*cKO are shown within each region (apical or basal). *$p < 0.05$; ****$p <$
722 0.0001.

723 **See also Figure S1.**

724

725 **Figure 2. Loss of Autophagy Compromises the Endolysosomal System in LREs**

726 **(A)** Reverse transcription quantitative polymerase chain reaction (RT-qPCR) analysis of *Dab2*, *Mcoln3*,
727 *Lamp2* and *Ctsl1* genes in epithelial cells from proximal and distal samples of small intestines from WT
728 mice at the indicated time points (n = 3). Data relative to values of proximal region of small gut from
729 embryonic day (E) 18.5 mice embryos, and presented as $\log_{10}$ fold changes ($\log_{10}$FC).

730 **(B)** RT-qPCR of *Dab2*, *Mcoln3*, and *Lamp2* in ileal epithelial cells from WT and *Atg16*cKO mice at P7 and
731 P14. Sample sizes: *Dab2* and *Lamp2* (n = 10,6,6,6), *Mcoln3* (n = 9,8,6,6).

732 **(C and D)** Immunoblot analysis of Dab2 protein in ileal epithelial cell lysates from WT and *Atg16*cKO mice
733 at P7 and P14 (C). Actin, loading control. (D) Quantification of Dab2 protein levels (n = 6,8,9,14).

734 **(E and F)** Confocal images of ileal sections from WT and *Atg16*cKO mice at P7 and P14 (n = 3) labelled
735 with anti-Dab2 (green), β-catenin (magenta), and DAPI (blue) (E). Arrowheads mark apical Dab2
736 localization. (F) Violin plot quantifying apical Dab2 intensity (integrated density) of P14 sections, normalised
737 to epithelial area (n = 10,8; 2–4 images per mouse).

738 **(G and H)** Lysosomal occupation and content in WT and *Atg16*cKO mice at P7 and P14, and in post-
739 weaning (P21–30) WT mice. Confocal sections labelled with anti-LAMP1 (green), β-catenin (white), and
740 DAPI (blue) (G). Arrows: endolysosomal system in WT LREs; arrowheads: reduced $LAMP1^+$ vesicles in
741 *Atg16*cKO and post-weaning enterocytes. (H) Dot plots quantify the percentage of $LAMP1^+$ area and
742 LAMP1 intensity (integrated density) within apical and basal regions of interest (ROIs) (n = 26–36).

743 **(I and J)** Immunoblot analysis of LAMP1 protein in ileal epithelial cell lysates from WT and *Atg16*cKO mice
744 at P14 (I). Actin, loading control. (J) Quantification of LAMP1 protein levels (n = 10,13).

745 In (E, F), dashed-line squares indicate magnified areas; L, lumen. Scale bars: 10 μm (main); 5 μm (insets).

Dots represent individual mice (B, D, J) or images (F) or cells (H). In (B, D, F, J), data relative to WT values. Graphs of (A) represent mean + SD; graphs of (B, D, J), mean + SEM; violin plot of (F), median (thick line) and interquartile range (IQR, thin lines); dot plots of (H), mean ± SEM (black lines).

Statistical analyses: Kruskal–Wallis test (A [*Dab2*, *Mcoln3*], H), two-way ANOVA (A: *Lamp2*, *Ctsl1*), Student's *t*-test (B, D, J), Mann–Whitney test (F). In (A), only the most relevant statistically significant comparisons are shown. In (H), only statistically significant comparisons are displayed within each group (apical or basal). *$p < 0.05$, **$p < 0.01$, ***$p < 0.001$, ****$p < 0.0001$.

See also Figure S2.

Figure 3. LREs Present High Levels of Mitophagy

(A) Workflow of RNA sequencing (RNA-seq) analysis comparing LREs from P7 GFP-LC3 mice gavaged with rhodamine B–dextran (Rd-dext) (16 hours prior) to PECs from P42 GFP-LC3 mice. Enterocytes were isolated from ileal samples by fluorescence-activated cell sorting (FACS) and used for RNA-seq. See Figure S4A for gating strategy. Scheme includes images adapted from Treuting et al.[75] and Park et al.[7].

(B) Volcano plot of differentially expressed genes (DEGs) between LREs and PECs. Each point represents a gene, plotted by $\log_2$ fold change (x-axis) and $-\log_{10}$ adjusted p-value (padj) (y-axis). DEGs (n = 1537; shown in steel blue) were defined as genes with padj < 0.05 and $|\log_2 FC| > 1$. Upregulated genes associated with endocytosis (amber), lysosome (purple), and mitophagy (red) are highlighted. Dashed lines indicate significance (padj < 0.05) and fold-change thresholds (±1). Genes with $-\log_{10}(\text{padj}) > 60$ are not shown.

(C) Bubble plot of selected Gene Ontology (GO) terms from over-representation analysis (ORA) of the differential gene expression data from the LREs vs PECs. Note the presence of regulation of autophagy, positive regulation of autophagy of mitochondrion and mitochondrial outer membrane pathways. The x-axis represents the z-score, bubble size reflects the number of associated genes, and bubble colour indicates statistical significance (adjusted p-value), with a red-to-blue gradient from most to least significant. GO terms are grouped into three categories: BP, biological process; CC, cellular component; MF, molecular function.

(D) Enrichment plots of lysosome organization and mitochondrial outer membrane gene sets from gene set enrichment analysis (GSEA) comparing LREs and PECs**.** The top panel shows the Enrichment Score (ES) across ranked genes, with the peak indicating maximum enrichment. The middle panel marks gene positions in the ranked list. The bottom colour bar reflects gene correlation with phenotype (red: positive, blue: negative).

(E) RT-qPCR analysis of *Bnip3*, *Prkn*, and *Pink1* genes in ileal epithelial cells from WT mice at indicated time points (n = 3). Values are expressed as $\log_{10}$ fold change relative to E18.5 embryonic levels.

779 **(F)** Confocal images of ileal sections from WT mice at P7 (LREs) and P21–30 (PECs), labelled with anti-
780 Parkin (green) and DAPI (blue). Left: violin plot of Parkin intensity (integrated density) normalised to
781 epithelial area.

782 **(G)** Schematic of the *mito*-QC reporter mouse model. Mitochondria are tagged with the chimeric protein
783 mCherry-GFP-FIS1$^{101–152}$. Upon mitophagy, mitochondria are delivered to the lysosome where acidic pH
784 quenches GFP but not mCherry, allowing identification of mitolysosomes as mCherry-only puncta.

785 **(H)** Confocal images of ileal sections from *mito*-QC mice at P7 (LREs) (± leupeptin, LP) and P21–30 (PECs).
786 Samples stained with anti-LAMP1 (white) and DAPI (blue). Arrows indicate enlarged, blocked lysosomes
787 with red-only mitochondrial aggregates in LREs+LP; arrowheads point to LAMP1^{+}/mCherry^{+} puncta lacking
788 GFP, validating the *mito*-QC model.

789 **(I)** Violin plot of lysosomal mCherry intensity normalised to cellular mCherry intensity from (H), based on
790 integrated density measurements.

791 **(J)** RT-qPCR of *Bnip3* and *Prkn* in ileal epithelial cells from WT and *Atg16*cKO mice at P14. Dots represent
792 individual mice. Sample sizes: *Bnip3* (n = 6, 6), *Prkn* (n = 5, 6).

793 **(K)** Confocal images of ileal sections from WT and *Atg16*cKO mice at P14 stained with anti-Parkin (green)
794 and DAPI. Left: violin plot of Parkin intensity (Integrated Density) normalised to epithelial area.

795 **(L)** Confocal images of ileal sections from *mQ*-WT and *mQ-Atg16*cKO mice at P14 (n = 3), labelled with
796 anti-LAMP1 (white) and DAPI (blue).

797 **(M)** Violin plot of lysosomal mCherry intensity normalised to cellular mCherry intensity from (L), based on
798 integrated density measurements (n = 12–11; 3–4 images per mouse).

799 In images of (F, H, K, L), L, lumen. Scale bars: 5 µm. Images of (H, L) deconvolved with Huygens software.

800 In (A–I) and (K–M), n = 3; in (F, I, K), n = 9 images from 3 mice (3 images per mouse). In graphs of (F, I),
801 data relative to LREs values; in (J, K, M), relative to WT values. In (E), graph represents mean + SD; in (J),
802 mean + SEM. In violin plots of (F, I, K, M), the median (thick line) and IQR (thin lines) are shown and dots
803 represent individual images.

804 Statistical analyses: Kruskal–Wallis test (E: *Bnip3*), one-way ANOVA (E [*Prkn*, *Pink1*], I), Student's *t*-test
805 (F, J, K, M). *p< 0.05, **p< 0.01, ***p < 0.001.

806 **See also Figure S4.**

807

808 **Figure 4. *Atg16*cKO Neonatal Mice Exhibit Increased Mitochondrial Damage and Oxidative Stress in**
809 **Enterocytes**

810 **(A)** Representative transmission electron microscopy (TEM) micrographs of ileal sections from WT and
811 *Atg16*cKO mice at P14 (n = 3). Note the reduction of the endolysosomal system and the absence of

812 lysosomal vacuole in the *Atg16*cKO enterocytes. Dashed boxes indicate magnified areas. N, nucleus; LV,
813 lysosomal vacuole; AEC, apical endosomal complex; L, lumen. Asterisks indicate damaged mitochondria.
814 Scale bars: 2 μm (main); 500 nm (insets).

815 **(B)** TEM-based classification of mitochondria into three categories based on electron density and cristae
816 integrity: Class I (normal), Class II (partially affected), and Class III (damaged). Classification based on
817 Moschandrea et al. [44]. See Electron Microscopy Section in Methods. Scale bar: 500 nm.

818 **(C)** Distribution of mitochondrial integrity classes in *Atg16*cKO neonatal enterocytes. Quantification of the
819 number, percentage, area and aspect ratio (long axis / short axis) of each mitochondria class in (A), as
820 defined in (B). In count and percentage graphs, dots represent individual enterocytes; in area and aspect
821 ratio graphs, dots represent individual mitochondria. Sample sizes are indicated in Table S1.

822 **(D)** Flow cytometry analysis of mitochondrial status of *Atg16*cKO neonatal enterocytes. Graphs show
823 relative mean fluorescence intensity (MFI) for Mitotracker Green (mitochondrial mass, MM), Mitotracker
824 Red CMXROS (mitochondrial membrane potential, MMP) and CM-H_2DCFDA (ROS) in ileal EpCAM$^+$CD24$^-$
825 cKit$^-$ cells from WT and *Atg16*cKO mice at P14. See Figure S3 for gating strategy. Dots represent individual
826 mice (MM, n = 23,17; MMP, n = 10,9; ROS, n = 19,13).

827 In (C), dot plots represent mean ± SEM (black lines). In (D), bar chart show mean + SEM.

828 Statistics analyses: Mann–Whitney test (C, D [MM]), Student's *t*-test (D: MMP, ROS). *p < 0.05, **p < 0.01,
829 ***p < 0.001, ****p < 0.0001.

830 **See also Figure S3 and Table S1.**

831

832 **Figure 5. Autophagy Deficiency Causes Early Metabolic Transition in LREs**

833 **(A)** RT-qPCR analysis of transcription factor (*Mafb*, *c-maf*, *Blimp1*), neonatal (*Ass1*, *Glb1*) and adult (*Treh*,
834 *Sis*, *Arg2*) enzyme genes in ileal epithelial cells from WT and *Atg16*cKO mice at late neonatal stage (P14)
835 and from WT mice at post-weaning stage (P21–30). Sample sizes: *Mafb* (n = 8, 9, 3), *c-maf* (n = 8, 11, 3),
836 *Blimp1* (n = 11, 9, 4), neonatal enzymes (n = 6, 5, 4), *Treh* (n = 5, 3, 4), *Sis* (n = 5, 5, 4), *Arg2* (n = 5, 6, 4).

837 **(B)** Confocal images of ileal sections from WT and *Atg16*cKO mice at P14 (n = 5), and from post-weaning
838 (P21–30) WT mice (n = 2–3), labelled with anti-MAFB (green, top) or anti-BLIMP1 (green, bottom), and with
839 phalloidin for F-actin (magenta) and DAPI (blue). Arrowheads point to nuclear localization of MAFB and
840 BLIMP1 in WT LREs.

841 **(C)** Violin plot of nuclear MAFB (n = 20, 21, 11) and BLIMP1 (n = 21, 16, 9) intensity (integrated density) in
842 (B), normalised to epithelial nuclear area.

843 **(D)** Confocal images of ileal sections from WT and *Atg16*cKO mice at P14, labelled with anti-ASS1 (green,
844 top) (n = 3) or anti-TREH (green, bottom) (n = 5), anti-E-cadherin (Ecad, magenta), and DAPI (blue).

845 **(E)** Violin plots of ASS1 (top; n = 12, 10) and TREH (bottom; n = 15,16) intensity (integrated density) in (D),
846 normalised to epithelial area.

847 **(F)** Western blot of TREH protein from ileal epithelial cells of WT and *Atg16*cKO mice at P14. USP7, loading
848 control.

849 **(G)** Bar chart quantifying TREH protein levels from (F) (n = 5, 4).

850 **(H)** Met-Flow profiling of ileal $EpCAM^{+}CD24^{-}$ cells from WT (n = 10–13) and *Atg16*cKO (n = 7–9) mice at
851 P14, and from post-weaning (P21–30) WT mice (n = 8). Bubble colour and size reflect group means for
852 each marker. See Figure S3 for the gating strategy and Table S2 for statistical significance.

853 In (B, D), dashed boxes indicate magnified areas; L, lumen. Scale bars: 10 µm (main); 5 µm (insets).

854 In (A, C, E, G, H), data relative to WT P14 values. In (A, G), graphs show mean + SEM and dots represent
855 individual mice. In (C, E), violin plots depict the median (thick line) and IQR (thin lines) and dots are
856 individual images (2–5 images per mouse, 2–5 mice per group).

857 Statistical analyses: one-way ANOVA (A, C [MAFB], H), Kruskal–Wallis test (C: BLIMP1), Mann–Whitney
858 test (E), Student's t test (G). *p < 0.05, **p < 0.01, ***p < 0.001, ****p < 0.0001.

859 **See also Figures S3 and S5, and Table S2.**

860

861 **Figure 6. *Tfam*cKO Neonates Recapitulate Endolysosomal and Metabolic Defects Observed in**
862 ***Atg16*cKO Enterocytes, and Exhibit Weight Loss and Early Lethality**

863 **(A)** Representative images of WT and *Tfam*cKO mice at postnatal day 14 (P14).

864 **(B)** Kaplan–Meier survival curves of WT and *Tfam*cKO mice. Animals were euthanized if they failed to gain
865 weight for two consecutive days or exhibited marked weight loss beginning at P9.

866 **(C)** Relative body weight of WT and *Tfam*cKO mice at P8, P10, P12, and P14, expressed as percentage.
867 Sample sizes are indicated at the bottom of the graph.

868 **(D)** RT-qPCR analysis of *Tfam* mRNA in ileal epithelial cells from WT and *Tfam*cKO mice at P10 and P14
869 (n = 12,12,12,10).

870 **(E)** *Tfam*cKO neonatal enterocytes show damaged mitochondria. TEM micrographs of ileal sections from
871 WT (n = 3) and *Tfam*cKO (n = 4) mice at P10 and P14. Asterisks indicate damaged mitochondria. Scale
872 bar, 1 µm.

873 **(F)** Quantification of mitochondrial classes in (E), as defined in Figure 4B. Dots represent individual
874 enterocytes. Sample sizes are indicated in Table S1.

875 **(G)** Flow cytometry analysis of mitochondrial status of *Tfam*cKO neonatal enterocytes. Bar charts show
876 relative MFI for Mitotracker Green (mitochondrial mass, MM), Mitotracker Red CMXROS (mitochondrial

877 membrane potential, MMP) and CM-H_2DCFDA (ROS) in ileal EpCAM$^+$CD24$^-$cKit$^-$ cells from WT and
878 *Tfam*cKO mice at P10 and P14. Sample sizes: MM (n = 5, 5, 8, 14), MMP (n = 3, 4, 10, 13), ROS (n = 9, 6,
879 10, 9). See Figure S3 for gating strategy.

880 **(H)** Confocal images of ileal sections from WT and *Tfam*cKO mice at P14 (n = 3–4), stained with anti-MAFB
881 (green, top) or anti-BLIMP1 (green, bottom), phalloidin (magenta), and DAPI (blue). Arrowheads mark
882 nuclear localization of MAFB and BLIMP1 in WT LREs.

883 **(I)** Violin plots quantifying nuclear MAFB (top; n = 15, 10) and BLIMP1 (bottom; n = 16, 16) intensity in (H),
884 normalised to epithelial nuclear area.

885 **(J)** Confocal images of ileal sections from WT and *Tfam*cKO mice at P14 (n = 3–4). Top: labelled with anti-
886 ASS1 (green), anti-E-cadherin (Ecad, magenta), and DAPI (blue). Bottom: labelled with anti-TREH (green)
887 and anti-Ecad (magenta).

888 **(K)** Violin plots quantifying ASS1 (top; n = 14, 16) and TREH (bottom; n = 9, 10) intensity in (J), normalised
889 to epithelial area.

890 **(L)** Met-Flow profiling of ileal EpCAM$^+$CD24$^-$ cells from WT (n = 6) and *Tfam*cKO (n = 5) mice at P14. Bubble
891 colour and size reflect group means for each marker. See Figure S3 for the gating strategy and Table S2
892 for statistical significance.

893 **(M)** Confocal images of ileal sections from WT (n = 4) and *Tfam*cKO (n = 3) mice at P14 gavaged with
894 rhodamine B–dextran (Rd-dext, red) 3 hours before sacrifice. Sections were stained with anti-LAMP1
895 (green), anti-β-catenin (white), and DAPI (blue). Arrow: endolysosomal system in WT LREs; arrowhead:
896 reduced LAMP1$^+$ vesicles in *Tfam*cKO enterocytes. Images deconvolved with Huygens software.

897 **(N)** Violin plot quantifying Rd-dextran uptake (integrated density) in (M), normalised to epithelial area (n =
898 11, 7).

899 **(O)** Quantification of lysosomal occupation and content in (M). Dot plots show the LAMP1$^+$ area as a
900 percentage of cell area (n = 167, 145) and LAMP1 intensity (integrated density) per enterocyte (n = 148,
901 139).

902 In (D–O), mice aged P9–11 and P13–15 were grouped as “P10” and “P14,” respectively.

903 In (H, J, M), dashed boxes indicate magnified areas; L, lumen. Scale bars: 10 μm (main); 5 μm (insets).

904 In (C, D, G, I, K, L, N), data relative to WT values. In (C, D, G), graphs depict mean + SEM and dots
905 represent individual mice. In (F, O), dot plots show mean ± SEM (red lines) and dots represent individual
906 enterocytes. In (I, K, N), violin plots show median (thick line) and IQR (thin lines) and dots represent
907 individual images (2–4 per mouse).

908 Statistical analyses: Gehan–Breslow–Wilcoxon test (B), Student’s *t*-test (C, D, F [P14 Class III only], G, K,
909 L, N), Mann–Whitney test (F [except P14 Class III], I, O). *$p < 0.05$, **$p < 0.01$, ***$p < 0.001$, ****$p < 0.0001$.

910 **See also Figures S3, S6 and S7, and Tables S1 and S2.**

911

912 **Figure 7. High Antioxidant Activity in LREs Regulates the Timing of Metabolic Transition**

913 **A)** Bar chart showing the relative mean fluorescence intensity (MFI) of MitoSOX (mitochondrial ROS) and
914 CM-H_2DCFDA (total ROS) in ileal EpCAM$^+$CD24$^-$ cells from WT mice at P7 (LREs) and P21–30 (PECs) (n
915 = 4). Data relative to LREs values. See Figure S3 for gating strategy.

916 **(B)** Bubble plot and list of ROS-related GO terms from over-representation analysis (ORA) of DEGs
917 between LREs and PECs. The x-axis represents the z-score, the y-axis shows the significance as –
918 $\log_{10}$(adjusted p-value), bubble size reflects the number of associated genes, and colours indicate GO
919 categories (BP, biological process; CC, cellular component; MF, molecular function).

920 **(C)** GSEA enrichment plot of antioxidant activity gene set (LREs vs PECs).

921 **(D)** RT-qPCR analysis of *Gpx3* and *Cat* genes in ileal epithelial cells from WT mice at the indicated time
922 points (n = 3). Values are expressed as $\log_{10}$ fold change relative to E18.5 embryonic levels.

923 **(E)** RT-qPCR analysis of *Gpx3* and *Cat* genes in ileal epithelial cells from WT and *Atg16*cKO mice at P14
924 (n = 6).

925 **(F)** RT-qPCR analysis of *Gpx3* (n = 7, 5) and *Cat* (n = 5, 7) in ileal epithelial cells from WT and *Tfam*cKO
926 mice at P14.

927 **(G)** Confocal images of ileal sections from WT and *Atg16*cKO mice at P14 (n = 3), stained with anti-GPX3
928 (green), anti-E-cadherin (Ecad, magenta), and DAPI (blue).

929 **(H)** Violin plot of GPX3 intensity from (G), normalised to epithelial area (n = 12, 9).

930 **(I)** Confocal images of ileal sections from WT and *Tfam*cKO mice at P14 (n = 4), labelled as in (F).

931 **(J)** Violin plot of GPX3 intensity from (H), normalised to epithelial area (n = 16).

932 **(K)** RT-qPCR analysis of transcription factor (*Mafb*, *c-maf*, *Blimp1*), neonatal (*Ass1*, *Glb1*) and adult (*Treh*,
933 *Arg2*) enzyme genes in ileal epithelial cells from control and H_2O_2 treated mice at P12. Sample sizes: *Mafb*
934 (n = 7, 6), *c-maf* (n = 7, 6), *Blimp1* (n = 7, 7), neonatal enzymes (n = 7, 7), *Treh* (n = 5, 6), *Arg2* (n = 6, 6).

935 **(L)** Confocal images of ileal sections from control (n = 4) and H_2O_2-treated (n = 4–5) mice at P12, stained
936 with anti-BLIMP1 (green, left) or anti-ASS1 (green, centre) or anti-TREH (green, right), and DAPI (blue). L,
937 lumen. Scale bars, 10 µm.

938 **(M)** Violin plots of BLIMP1, ASS1 and TREH intensity (integrated density) from (L). BLIMP1 data were
939 normalised to epithelial nuclear area; ASS1 and TREH data, to epithelial area. Sample sizes: BLIMP1 (n =
940 12, 15), ASS1 (n = 12, 16), TREH (n = 13, 12).

941 **(N)** Flow cytometry analysis of BLIMP1 (n = 7, 7) and ASS1 (n = 6, 7) in control and H_2O_2-treated mice at
942 P12. Bar charts show relative median fluorescent intensity of BLIMP1 and ASS1 in ileal EpCAM$^+$CD24$^-$cKit$^-$
943 cells. See Figure S3 for gating strategy.

944 **(O)** Working model: In *Atg16*cKO and *Tfam*cKO neonatal enterocytes, mitochondrial dysfunction and
945 reduced antioxidant activity elevate ROS levels, which repress *Blimp1* and *Mafb* expression and drive early
946 metabolic transition. Enterocyte's design inspired by Fujita et al.[9]. Figure created with BioRender.com.

947 In (G, I), dashed boxes indicate magnified areas; L, lumen. Scale bars: 10 μm (main); 5 μm (insets).

948 In (E, F, H, J), data relative to WT values; in (K, M, N), relative to control values. In (A, E, F, K, N), graphs
949 represent mean + SEM and dots represent individual mice; in (D), mean + SD. In (H, J, M), violin plots show
950 median (thick line) and IQR (thin lines) and dots represent individual images (2–4 per mouse, 3–5 mice per
951 group).

952 Statistical analyses: Student's t test (A, E, F, H, K, M [ASS1], N), one-way ANOVA (D), Mann–Whitney test
953 (J, M [BLIMP1, TREH]). *$p < 0.05$, **$p < 0.01$, ***$p < 0.001$, ****$p < 0.0001$.

954 **See also Figure S3.**

955

956 **SUPPLEMENTAL INFORMATION**

957 **Figure S1. Characterization of LREs in the Neonatal Mouse Ileum**
958 ***Related to Figures 1 and 2***

959 (**A**) Representative TEM image of LREs from the distal small intestine of a P7 mice (n = 3). The profile of
960 an LRE is outlined by a dashed line. Dashed boxes indicate magnified areas. N, nucleus; LV, lysosomal
961 vacuole; AEC, apical endosomal complex; e, endosome; mvb, multivesicular body; L, lumen. Scale bars:
962 5 μm (main); 2 μm (insets).

963 (**B**) Confocal microscopy images of ileal sections from P7 mice (n = 3), stained with anti-LAMP1 (green),
964 anti-Dab2 (magenta), anti-β-catenin (white), and DAPI (cyan). Dashed boxes highlight magnified areas.
965 Arrows indicate the endolysosomal system; arrowheads point to apical Dab2 localization. Scale bars: 20 μm
966 (main); 10 μm (first magnification); 5 μm (second magnification).

967 (**C**) Western blot of mCherry and GFP-LC3 isoforms in ileal epithelial cells from GFP-LC3 mice at P7 and
968 P21, gavaged with mCherry 3 hours before sacrifice. USP7, loading control.

969 (**D**) Sequential fluorescent dextran uptake assay. P7 mice were gavaged with Alexa 647-dextran (FR-dext,
970 green), followed by rhodamine B–dextran (Rd-dext, red) 3 hours later. Mice were sacrificed at 4 and 8 hours
971 post-initial gavage to assess uptake via confocal microscopy (n = 3). Arrows point to lysosomal vacuoles
972 containing both dextrans at 8 hours. Arrowheads indicate endosomes. Scale bars: 5 μm (main); 2 μm
973 (insets).

974

975 **Figure S2. Phenotype of *Atg16*cKO Mice**

976 ***Related to Figures 1 and 2***

977 **(A)** Relative body weight of WT and *Atg16*cKO mice at postnatal days P7, P14, and P30. Sample sizes are
978 indicated in the graph.

979 **(B)** Representative images of intestines from WT and *Atg16*cKO mice at the post-weaning stage (P30).

980 **(C)** Quantification of intestinal lengths shown in (B). Bar graphs show the relative lengths of the small
981 intestine (SI) and the colon–rectum (CR) segments (n = 7, 9).

982 **(D)** Representative histological images of ileum and colon sections from WT and *Atg16*cKO post-weaning
983 (P30) mice (n = 3). Ileal sections are stained with periodic acid-Schiff (PAS) and haematoxylin; colon
984 sections are stained with haematoxylin and eosin (H&E). Asterisks denote oedema in *Atg16*cKO ileum;
985 arrowheads indicate goblet cells. Scale bars: 200 µm (ileum), 400 µm (colon).

986 **(E and F)** Flow cytometry analysis of immune and epithelial cell populations in the ileum of WT and
987 *Atg16*cKO mice at P14 (E) and P30 (F). Left: B lymphocytes (LB) and T-helper lymphocytes (LTh)
988 percentages. Centre: Innate immune cells (IIC) and intestinal epithelial cells (IEC) percentages. Right:
989 Enterocyte and enterocytic progenitors (EC), goblet cell (GC), Paneth cell (PC), and enteroendocrine cell
990 (EEC) percentages. See Figure S3 for gating strategy. (E): Left, n = 17,8–11; Centre, n = 22,16–17; Right,
991 n = 15,12–13. (F): n = 6–7, 9–10.

992 **(G)** RT-qPCR analysis of *Dab2* (n = 10,6,6,5), *Mcoln3* (n = 9,8,6,5), and *Lamp2* (n = 10,6,6,6) in epithelial
993 cells from the proximal small intestine of WT and *Atg16*cKO mice at P7 and P14.

994 **(H)** RT-qPCR analysis of *Amn* (n = 6,5), *Mamdc4* (n = 9,10), and *Ctsl1* (n = 9,11) in ileal epithelial cells
995 from WT and *Atg16*cKO mice at P14.

996 In (A, C, G, H), graphs represent mean + SEM. In (E, F), violin plots depict median (thick line) and
997 interquartile range (IQR, thin lines). In all graphs, data relative to WT values, dots represent individual mice
998 and Student's t test was conducted. *p < 0.05, **p < 0.01, ***p < 0.001, ****p < 0.0001.

999

1000 **Figure S3. Gating Strategies Used for Cell Population Characterization by Flow Cytometry**

1001 ***Related to Figures 4–7, S2 and S4–S6***

1002 Biopool is the combination of immune cell markers anti-CD11c, anti-CD3e, anti-CD11b, anti-CD19, and
1003 anti-CD45.2. The strategy for selecting IEC subtypes is based on Asano et al. [36]. GD, ghost dye; LT_h, T-
1004 helper lymphocytes; LB, B lymphocytes; IIC, innate immune cells; IEC, intestinal epithelial cells; EEC,
1005 enteroendocrine cells; PC, Paneth cells; EC, enterocytes and enterocytic progenitors; GC, goblet cells.

1006

1007 **Figure S4. RNA-seq Analysis Comparing Gene Expression of LREs and PECs**

1008 ***Related to Figure 3***

1009 **(A)** FACS gating strategy used to isolate LREs and PECs from GFP-LC3 mice at P7 (gavaged with Rd-
1010 dextran, 16 hours) and P42, respectively, for RNA-seq analysis. Single-living $EpCAM^{+}CD24^{-}Biopool^{-}$ cells
1011 were gated. For LREs, $Rd\text{-}dext^{+}GFP^{high}$ cells were selected.

1012 **(B)** Heatmap with hierarchical clustering of differentially expressed genes (DEGs) with q-value < 0.05
1013 reveals distinct expression patterns between LREs and PECs. Each row represents a single gene and each
1014 column represents a condition sample. Each sub-column represents an individual sample (3 samples per
1015 group). Gene expression intensities were log_2-transformed and visualized as a colour gradient from yellow
1016 to light blue, representing the shift from downregulation to upregulation, as indicated in the key.

1017 **(C)** Principal component analysis (PCA) plotting for 2 groups based on normalised overall transcriptomic
1018 reads. The PCA figure represents a two-dimensional scatterplot of the first two principal components of the
1019 RNA-Seq data. Analyses in panels (B) and (C) show that replicates of the same cell population are more
1020 similar to each other than to replicates from a different population.

1021 (**D**) Bubble plot of selected Kyoto Encyclopaedia of Genes and Genomes (KEGG) pathways from over-
1022 representation analysis (ORA) of the differential gene expression data from the LREs vs PECs. The x-axis
1023 represents the z-score, the y-axis shows the significance as –log10(adjusted p-value), bubble size reflects
1024 the number of associated genes, and colours indicate KEGG pathway categories.

1025 **(E)** RT-qPCR validation of *Ctsl1* expression in LREs and PECs from WT mice at P7 (gavaged with Rd-
1026 dextran, 16 hours) and P42, respectively. FACS was used for cell sorting, selecting single-living
1027 $EpCAM^{+}CD24^{-}Biopool^{-}$ cells, with $Rd\text{-}dext^{+}$ cells further gated for LREs. In LREs, each dot represents one
1028 of three pooled samples (n = 3), each composed of multiple mice; in PECs, each dot corresponds to an
1029 individual mouse (n = 3). Data relative to LREs values.

1030 **(F)** Analysis of lysosomal content in LREs and PECs by measuring Lysotracker MFI by flow cytometry. Bar
1031 chart depicts Lysotracker MFI of LREs and PECs from WT mice at P7 (gavaged with mCherry, 16 hours)
1032 and P42 respectively. Single-living $EpCAM^{+}CD24^{-}Biopool^{-}$ cells were gated. For LREs, $mCherry^{+}$ cells were
1033 selected. See Figure S3 for gating strategy. Dots represent individual mice (n = 3).

1034 Graphs in (E, F) represent mean + SEM. In (E), Student's t test; in (F), Mann–Whitney test. *p < 0.05, **p
1035 < 0.01.

1036

1037 **Figure S5. Metabolic Transition in the Small Gut During Postnatal Development**

1038 ***Related to Figure 5***

1039 (**A)** Expression and statistical data of selected genes encoding transcription factors (TFs: *Mafb, c-maf,*
1040 *Blimp1*), neonatal enzymes (*Ass1, Glb1*), and adult enzymes (*Treh, Sis, Arg2*) from the LREs vs PECs
1041 RNA-seq analysis.

1042 **(B and C)** RT-qPCR analysis of *Mafb* and *Blimp1* (B), and of *Ass1, Glb1, Treh,* and *Sis* (C) genes in
1043 epithelial cells isolated from proximal and distal small intestinal segments of WT mice at the indicated
1044 postnatal time points (n = 3). Data are normalised to the expression levels in the proximal small intestine of
1045 E18.5 embryos and expressed as $\log_{10}$fold change ($\log_{10}$FC).

1046 **(D)** Schematic representation of the cellular metabolic pathways. Enzymes used in the Met-flow panel are
1047 shown in red. Scheme adapted from Iborra et al. [45] (CC BY 4.0).

1048 **(E)** Met-Flow analysis of ileal $EpCAM^{+}CD24^{-}$ cells from WT mice at P7 (LREs) and P42 (PECs) (n = 2–4).
1049 Data relative to LREs values. Bubble colour and size reflect group means for each marker. See Figure S3
1050 for the gating strategy and Table S2 for statistical significance.

1051 In (B, C), graphs represent mean + SD, two-way ANOVA was conducted and only the most relevant
1052 statistically significant comparisons are shown. In (E), Student's *t*-test. *p < 0.05, **p < 0.01, ***p < 0.001,
1053 ****p < 0.0001.

1054

1055 **Figure S6. Validation and Intestinal Phenotype of *Tfamc*KO Neonatal Mice**
1056 ***Related to Figure 6***

1057 **(A)** Relative mitochondrial DNA (mtDNA) levels of *Nd1*, *Co1*, *Co2*, and *Atp6* in ileal epithelial cells from WT
1058 and *Tfam*cKO mice at P10 (n = 2) and P14 (n = 4), measured by qPCR.

1059 **(B)** RT-qPCR analysis of mitochondrial genes *mt-Nd1*, *mt-Co2*, and *Sdha* in ileal epithelial cells from WT
1060 and *Tfam*cKO mice at P10 (n = 5–6).

1061 **(C)** Confocal images of ileal sections from WT (n = 3) and *Tfam*cKO (n = 2) mice at P14, labelled with anti-
1062 MTCO1 (green) and anti-β-catenin (magenta). Arrows point to mitochondria in WT LREs.

1063 **(D)** Violin plot shows MTCO1 intensity (integrated density) from (C), normalised to epithelial area. Dots
1064 represent individual images (n = 9,7; 3–4 images per mouse).

1065 **(E)** PAS and haematoxylin staining of ileal sections from WT and *Tfam*cKO mice at P10 and P14 (n = 4–6)
1066 shows inflamed and disorganized epithelium in *Tfam*cKO mice. Phenotypes include shortened villi (double
1067 red arrows), thickened submucosa and lower mucosa (double black arrows), oedema (asterisks), reduced
1068 PAS+ goblet cells (arrowheads), and abnormal vacuoles in enterocytes (arrows).
1069 Scale bars: 200 µm (main); 100 µm (insets).

1070 **(F–H)** Quantification of villi length (F), percentage of villi with goblet cells (G), and the maximum thickness
1071 of submucosa and lower mucosa (H) from (E). In (F), each dot represents a villus (n = 50,60,50,50; 10 villi
1072 per mouse). For (G–H), n = 4–6 mice.

1073 **(I–K)** Flow cytometry analysis of innate immune cells (IIC, I), B lymphocytes (LB, J), and T-helper cells (LT_h,
1074 K) percentages in the ileal of WT and *Tfam*cKO mice at P10 and P14 (n = 3–5). See Figure S3 for gating
1075 strategy.

1076 **(L–O)** Confocal imaging and quantification of stem and Paneth cells in WT and *Tfam*cKO ileal at P10 and
1077 P14:

1078 - (**L**) Olfm4 (green) labels crypt stem cells; arrows point to $Olfm4^+$ crypts.
1079 - (**M**) Quantification of $Olfm4^+$ crypts (30-100 crypts/mouse).
1080 - (**N**) Lysozyme (green) marks Paneth cells; arrows show normal crypt localization, arrowheads
1081 indicate mislocalised Paneth cells in villi.
1082 - (**O**) Quantification Paneth cells/mm^2 of epithelial area.

1083 For (L, N), sections are also stained with anti-Ecad (white) and DAPI (blue). Scale bars: 200 µm (main);
1084 50 µm (insets). For all panels, n = 3 mice.

1085 **(P)** Distribution of mitochondrial integrity classes in *Tfam*cKO neonatal enterocytes. Quantification of the
1086 percentage, area and aspect ratio (long axis / short axis) of each mitochondria class in Figure 6E, as defined
1087 in Figure 4B. In percentage graph, dots represent individual enterocytes; in area and aspect ratio graphs,
1088 dots are individual mitochondria. Sample sizes are indicated in Table S1.

1089 In (C, E, L, N), dashed boxes indicate magnified areas; L, lumen.

1090 In (A, B, D, I–K), data relative to WT values. In (A, G–K, M, O), graphs represent mean + SEM and dots
1091 represent individual mice. In (B, D), violin plots show the median (thick line) and IQR (thin lines). In (F, P),
1092 dot plots show mean ± SEM (red lines).

1093 Statistical analyses: Student's t test (A, B, I–K, M, O), Mann–Whitney test (D, P), two-way ANOVA (F, H),
1094 Kruskal–Wallis test (G). In (F–H), only statistically significant comparisons between WT and *Tfam*cKO are
1095 indicated within each time group. *$p < 0.05$, **$p < 0.01$, ***$p < 0.001$, ****$p < 0.0001$.

1096

1097 **Figure S7. *Tfam*cKO Neonatal Enterocytes Exhibit a Decreased Endolysosomal System and**
1098 **Undergo an Early Metabolic Switch**
1099 ***Related to Figure 6***

1100 **(A)** RT-qPCR analysis of transcription factor (*Mafb*, *c-maf*, *Blimp1*), neonatal (*Ass1*, *Glb1*) and adult (*Treh*,
1101 *Sis*, *Arg2*) enzyme genes in ileal epithelial cells from WT and *Tfam*cKO mice at P10 and P14.

1102 **(B)** RT-qPCR analysis of *Dab2*, *Amn*, and *Mamdc4* genes in ileal epithelial cells from WT and *Tfam*cKO
1103 mice at P10 and P14.

1104 **(C)** Confocal images of ileal sections from WT and *Tfam*cKO mice at P10 (n = 3) and P14 (n = 2–3), labelled
1105 with anti-Dab2 (green), anti-β-catenin (white), and DAPI (blue). Arrowheads indicate apical Dab2
1106 localisation.

1107 **(D)** Violin plot shows apical Dab2 intensity (integrated density) from (C), normalised to epithelial area and
1108 relative to WT values. Dots represent individual images (n = 6, 6, 6, 4; 2 images per mouse).

1109 **(E)** RT-qPCR analysis of *Lamp2*, *Mcoln3*, and *Ctsl1* in ileal epithelial cells from WT and *Tfam*cKO mice at
1110 P10 and P14.

1111 **(F)** Confocal images of ileal sections from WT and *Tfam*cKO mice at P10 (n = 3), labelled with anti-LAMP1
1112 (green), anti-β-catenin (white), and DAPI (blue). Arrows indicate endolysosomal system in WT cells;
1113 arrowheads highlight the reduced lysosomal vesicles in *Tfam*cKO enterocytes.

1114 **(G)** Quantification of lysosomal occupation and content in (E). Dot plots show the LAMP1$^+$ area as a
1115 percentage of cell area (n = 157,99) and LAMP1 intensity (integrated density) per enterocyte (n = 117,74).
1116 Dots represent individual enterocytes.

1117 In (C, F), dashed boxes indicate magnified areas; L, lumen. Scale bars: 10 μm (main); 5 μm (insets).

1118 In (A, B, E), data relative to WT-P10 values, dots represent individual mice (n = 4–7), and graphs represent
1119 mean + SEM. In (D), violin plot shows the median (thick line) and IQR (thin lines). In (G), dot plots depict
1120 mean ± SEM (red lines).

1121 Statistical analyses: Kruskal–Wallis test (A [*Treh*], B [*Dab2*], E [*Lamp2*]), two-way ANOVA (A, B, E; except
1122 *Treh*, *Dab2*, *Lamp2*), Student's t test (D), Mann–Whitney test (G). In (A, B, E), only statistically significant
1123 comparisons between WT and *Tfam*cKO are indicated within each time group. *p < 0.05, **p < 0.01, ***p <
1124 0.001, ****p < 0.0001.

1125

1126 **Table S1. Sample sizes in TEM graphs**
1127 ***Related to Figures 4, 6 and S6***
1128 Values in the number (No.) and percentage columns correspond to enterocytes; in the area and aspect
1129 ratio columns, values correspond to individual mitochondria. For more detailed information on sample size
1130 of the analyses, see the TEM section in the Methods.

1131

1132 **Table S2. Statistical Significance of Met-Flow Experiments**
1133 ***Related to Figures 5, 6 and S5***
1134 For Figure 5H, statistical results are shown only for comparisons between WT and the two other groups.
1135 No statistical test was applied for HK1 of Figure S5E (n = 2). *p < 0.05, **p < 0.01, ***p < 0.001, ****p <
1136 0.0001. NS, not significant.
1137

1138 **REFERENCES**

1139 1. Beumer, J. & Clevers, H. Cell fate specification and differentiation in the adult mammalian intestine.
1140 *Nat. Rev. Mol. Cell Biol.* **22**, 39–53 (2021).

1141 2. Choo, J., Glisovic, N. & Matic Vignjevic, D. Gut homeostasis at a glance. *J. Cell Sci.* **135**, (2022).

1142 3. Henning, S. J. Postnatal development: coordination of feeding, digestion, and metabolism. *Am. J.*
1143 *Physiol.-Gastrointest. Liver Physiol.* (1981) doi:10.1152/ajpgi.1981.241.3.G199.

1144 4. Henning, S. J. Ontogeny of Enzymes in the Small Intestine. *Annu. Rev. Physiol.* **47**, 231–245 (1985).

1145 5. Rombout, J. H., Lamers, C. H., Helfrich, M. H., Dekker, A. & Taverne-Thiele, J. J. Uptake and transport
1146 of intact macromolecules in the intestinal epithelium of carp (Cyprinus carpio L.) and the possible
1147 immunological implications. *Cell Tissue Res.* **239**, 519–530 (1985).

1148 6. Kleinman, R. E. & Walker, W. A. Antigen processing and uptake from the intestinal tract. *Clin. Rev.*
1149 *Allergy* **2**, 25–37 (1984).

1150 7. Park, J. *et al.* Lysosome-Rich Enterocytes Mediate Protein Absorption in the Vertebrate Gut. *Dev. Cell*
1151 (2019) doi:10.1016/j.devcel.2019.08.001.

1152 8. Rodríguez-Fraticelli, A. E. *et al.* Developmental regulation of apical endocytosis controls epithelial
1153 patterning in vertebrate tubular organs. *Nat. Cell Biol.* **17**, 241–250 (2015).

1154 9. Fujita, M., Reinhart, F. & Neutra, M. Convergence of apical and basolateral endocytic pathways at
1155 apical late endosomes in absorptive cells of suckling rat ileum in vivo. *J. Cell Sci.* **97**, 385–394 (1990).

1156 10. Gonnella, P. A. & Neutra, M. R. Membrane-bound and fluid-phase macromolecules enter separate
1157 prelysosomal compartments in absorptive cells of suckling rat ileum. *J. Cell Biol.* **99**, 909–917 (1984).

1158 11. Kulkarni, D. H. & Newberry, R. D. Intestinal Macromolecular Transport Supporting Adaptive Immunity.
1159 *Cell. Mol. Gastroenterol. Hepatol.* **7**, 729–737 (2019).

1160 12. Remis, N. N. *et al.* Mucolipin Co-deficiency Causes Accelerated Endolysosomal Vacuolation of
1161 Enterocytes and Failure-to-Thrive from Birth to Weaning. *PLoS Genet.* **10**, (2014).

1162 13. Cox, C. M., Lu, R., Salcin, K. & Wilson, J. M. The Endosomal Protein Endotubin Is Required for
1163 Enterocyte Differentiation. *Cell. Mol. Gastroenterol. Hepatol.* **5**, 145–156 (2018).

1164 14. He, C. Balancing nutrient and energy demand and supply via autophagy. *Curr. Biol.* **32**, R684–R696
1165 (2022).

1166 15. Kaur, J. & Debnath, J. Autophagy at the crossroads of catabolism and anabolism. *Nat. Rev. Mol. Cell*
1167 *Biol.* **16**, 461–472 (2015).

1168 16. Foerster, E. G. *et al.* How autophagy controls the intestinal epithelial barrier. *Autophagy* **18**, 86–103
1169 (2022).

1170 17. Larabi, A., Barnich, N. & Nguyen, H. T. T. New insights into the interplay between autophagy, gut
1171 microbiota and inflammatory responses in IBD. *Autophagy* **16**, 38–51 (2020).

1172 18. Kuma, A. *et al.* The role of autophagy during the early neonatal starvation period. *Nature* **432**, 1032–
1173 1036 (2004).

1174 19. Wang, S. *et al.* The mitophagy pathway and its implications in human diseases. *Signal Transduct.*
1175 *Target. Ther.* **8**, 304 (2023).

1176 20. Zhong, Y. *et al.* The interplay between mitophagy and mitochondrial ROS in acute lung injury.
1177 *Mitochondrion* **78**, 101920 (2024).

1178 21. Lennicke, C. & Cochemé, H. M. Redox metabolism: ROS as specific molecular regulators of cell
1179 signaling and function. *Mol. Cell* **81**, 3691–3707 (2021).

1180 22. Morris, O. & Jasper, H. Reactive Oxygen Species in intestinal stem cell metabolism, fate and function.
1181 *Free Radic. Biol. Med.* **166**, 140–146 (2021).

1182 23. Popov, L.-D. Mitochondria as intracellular signalling organelles. An update. *Cell. Signal.* **109**, 110794
1183 (2023).

1184 24. Rath, E., Moschetta, A. & Haller, D. Mitochondrial function — gatekeeper of intestinal epithelial cell
1185 homeostasis. *Nat. Rev. Gastroenterol. Hepatol.* **15**, 497–516 (2018).

1186 25. Yim, W. W.-Y. & Mizushima, N. Lysosome biology in autophagy. *Cell Discov.* **6**, 6 (2020).

1187 26. Mizushima, N., Yamamoto, A., Matsui, M., Yoshimori, T. & Ohsumi, Y. In vivo analysis of autophagy in
1188 response to nutrient starvation using transgenic mice expressing a fluorescent autophagosome marker.
1189 *Mol. Biol. Cell* **15**, 1101–1111 (2004).
1190 27. Mizushima, N., Yoshimorim, T. & Levine, B. Methods in Mammalian Autophagy Research. *Cell* **140**,
1191 313–326 (2010).
1192 28. Ni, H.-M. *et al.* Dissecting the dynamic turnover of GFP-LC3 in the autolysosome. *Autophagy* **7**, 188–
1193 204 (2011).
1194 29. Spence, J. R., Lauf, R. & Shroyer, N. F. Vertebrate intestinal endoderm development. *Dev. Dyn.* (2011)
1195 doi:10.1002/dvdy.22540.
1196 30. Hansson, J. *et al.* Time-resolved Quantitative Proteome Analysis of *In Vivo* Intestinal Development.
1197 *Mol. Cell. Proteomics* **10**, M110.005231 (2011).
1198 31. Fujita, N. *et al.* The Atg16L complex specifies the site of LC3 lipidation for membrane biogenesis in
1199 autophagy. *Mol. Biol. Cell* **19**, 2092–2100 (2008).
1200 32. Mizushima, N. *et al.* Mouse Apg16L, a novel WD-repeat protein, targets to the autophagic isolation
1201 membrane with the Apg12-Apg5 conjugate. *J. Cell Sci.* **116**, 1679–1688 (2003).
1202 33. Hwang, S. *et al.* Nondegradative role of Atg5-Atg12/ Atg16L1 autophagy protein complex in antiviral
1203 activity of interferon gamma. *Cell Host Microbe* **11**, 397–409 (2012).
1204 34. el Marjou, F. *et al.* Tissue-specific and inducible Cre-mediated recombination in the gut epithelium.
1205 *Genes. N. Y. N 2000* **39**, 186–193 (2004).
1206 35. Cadwell, K. *et al.* A key role for autophagy and the autophagy gene Atg16l1 in mouse and human
1207 intestinal Paneth cells. *Nature* **456**, 259–263 (2008).
1208 36. Asano, J. *et al.* Intrinsic Autophagy Is Required for the Maintenance of Intestinal Stem Cells and for
1209 Irradiation-Induced Intestinal Regeneration. *Cell Rep.* **20**, 1050–1060 (2017).
1210 37. Boyle, E. I. *et al.* GO::TermFinder—open source software for accessing Gene Ontology information
1211 and finding significantly enriched Gene Ontology terms associated with a list of genes. *Bioinformatics*
1212 **20**, 3710–3715 (2004).
1213 38. Wilson, J. M., Whitney, J. A. & Neutra, M. R. Biogenesis of the apical endosome–lysosome complex
1214 during differentiation of absorptive epithelial cells in rat ileum. *J. Cell Sci.* **100**, 133–143 (1991).
1215 39. Li, A. *et al.* Mitochondrial autophagy: molecular mechanisms and implications for cardiovascular
1216 disease. *Cell Death Dis.* **13**, 444 (2022).
1217 40. Yang, Y. *et al.* Identification of MAP1LC3A as a promising mitophagy-related gene in polycystic ovary
1218 syndrome. *Sci. Rep.* **14**, 16982 (2024).
1219 41. Picca, A., Faitg, J., Auwerx, J., Ferrucci, L. & D'Amico, D. Mitophagy in human health, ageing and
1220 disease. *Nat. Metab.* **5**, 2047–2061 (2023).
1221 42. McWilliams, T. G. *et al.* mito-QC illuminates mitophagy and mitochondrial architecture in vivo. *J. Cell*
1222 *Biol.* **214**, 333–345 (2016).
1223 43. Jiménez-Loygorri, J. I. *et al.* Mitophagy curtails cytosolic mtDNA-dependent activation of cGAS/STING
1224 inflammation during aging. *Nat. Commun.* **15**, 830 (2024).
1225 44. Moschandrea, C. *et al.* Mitochondrial dysfunction abrogates dietary lipid processing in enterocytes.
1226 *Nature* 1–8 (2023) doi:10.1038/s41586-023-06857-0.
1227 45. Iborra-Pernichi, M. *et al.* Defective mitochondria remodelling in B cells leads to an aged immune
1228 response. *Nat. Commun.* **15**, 2569 (2024).
1229 46. Skrzypek, T. *et al.* Gradual disappearance of vacuolated enterocytes in the small intestine of neonatal
1230 piglets. *J. Physiol. Pharmacol. Off. J. Pol. Physiol. Soc.* **58 Suppl 3**, 87–95 (2007).
1231 47. Bara, A. M. *et al.* Maf family transcription factors are required for nutrient uptake in the mouse neonatal
1232 gut. *Dev. Camb. Engl.* **149**, dev201251 (2022).
1233 48. Harper, J., Mould, A., Andrews, R. M., Bikoff, E. K. & Robertson, E. J. The transcriptional repressor
1234 Blimp1/Prdm1 regulates postnatal reprogramming of intestinal enterocytes. *Proc. Natl. Acad. Sci. U.*
1235 *S. A.* (2011) doi:10.1073/pnas.1105852108.

1236 49. Muncan, V. *et al.* Blimp1 regulates the transition of neonatal to adult intestinal epithelium. *Nat.*
1237 *Commun.* (2011) doi:10.1038/ncomms1463.
1238 50. Ahl, P. J. *et al.* Met-Flow, a strategy for single-cell metabolic analysis highlights dynamic changes in
1239 immune subpopulations. *Commun. Biol.* **3**, 305 (2020).
1240 51. Hulzebos, C. V. & Sauer, P. J. J. Energy requirements. *Semin. Fetal. Neonatal Med.* **12**, 2–10 (2007).
1241 52. Campbell, C. T., Kolesar, J. E. & Kaufman, B. A. Mitochondrial transcription factor A regulates
1242 mitochondrial transcription initiation, DNA packaging, and genome copy number. *Biochim. Biophys.*
1243 *Acta* **1819**, 921–929 (2012).
1244 53. Srivillibhuthur, M. *et al.* TFAM is required for maturation of the fetal and adult intestinal epithelium. *Dev.*
1245 *Biol.* **439**, 92–101 (2018).
1246 54. Baixauli, F. *et al.* Mitochondrial Respiration Controls Lysosomal Function during Inflammatory T Cell
1247 Responses. *Cell Metab.* **22**, 485–498 (2015).
1248 55. Chung, K. W. *et al.* Mitochondrial Damage and Activation of the STING Pathway Lead to Renal
1249 Inflammation and Fibrosis. *Cell Metab.* **30**, 784-799.e5 (2019).
1250 56. Rodríguez-Colman, M. J. *et al.* Interplay between metabolic identities in the intestinal crypt supports
1251 stem cell function. *Nature* **543**, 424–427 (2017).
1252 57. Chen, P.-M. *et al.* c-Maf regulates pluripotency genes, proliferation/self-renewal, and lineage
1253 commitment in ROS-mediated senescence of human mesenchymal stem cells. *Oncotarget* **6**, 35404–
1254 35418 (2015).
1255 58. Qi, T. *et al.* Ascorbic Acid Promotes Plasma Cell Differentiation through Enhancing TET2/3-Mediated
1256 DNA Demethylation. *Cell Rep.* **33**, (2020).
1257 59. Murphy, M. P. How mitochondria produce reactive oxygen species. *Biochem. J.* **417**, 1–13 (2008).
1258 60. Liang, H. *et al.* Establishment of a mouse model of ovarian oxidative stress induced by hydrogen
1259 peroxide. *Front. Vet. Sci.* **11**, (2024).
1260 61. Birgisdottir, Å. B. & Johansen, T. Autophagy and endocytosis – interconnections and
1261 interdependencies. *J. Cell Sci.* **133**, jcs228114 (2020).
1262 62. Zemirli, N., Morel, E. & Molino, D. Mitochondrial Dynamics in Basal and Stressful Conditions. *Int. J.*
1263 *Mol. Sci.* **19**, 564 (2018).
1264 63. Walker, W. A. Initial Intestinal Colonization in the Human Infant and Immune Homeostasis. *Ann. Nutr.*
1265 *Metab.* **63**, 8–15 (2013).
1266 64. Sena, L. A. & Chandel, N. S. Physiological roles of mitochondrial reactive oxygen species. *Mol. Cell*
1267 **48**, 158–167 (2012).
1268 65. Sies, H., Berndt, C. & Jones, D. P. Oxidative Stress. *Annu. Rev. Biochem.* **86**, 715–748 (2017).
1269 66. Massaquoi, M. S. & Guillemin, K. Packing in the Proteins. *Dev. Cell* **51**, 1–2 (2019).
1270 67. Cosovanu, C. *et al.* Intestinal epithelial c-Maf expression determines enterocyte differentiation and
1271 nutrient uptake in mice. *J. Exp. Med.* **219**, e20220233 (2022).
1272 68. Bhutta, Z. A. *et al.* Severe childhood malnutrition. *Nat. Rev. Dis. Primer* **3**, 17067 (2017).
1273 69. Trehan, I. & Manary, M. J. Management of severe acute malnutrition in low-income and middle-income
1274 countries. (2015) doi:10.1136/archdischild-2014-306026.
1275 70. Becker, K. *et al.* Effects of antioxidants on glutathione levels and clinical recovery from the malnutrition
1276 syndrome kwashiorkor--a pilot study. *Redox Rep. Commun. Free Radic. Res.* **10**, 215–226 (2005).
1277 71. Hodzic, Z., Bolock, A. M. & Good, M. The Role of Mucosal Immunity in the Pathogenesis of Necrotizing
1278 Enterocolitis. *Front. Pediatr.* **5**, (2017).
1279 72. Wallaeys, C., Garcia-Gonzalez, N. & Libert, C. Paneth cells as the cornerstones of intestinal and
1280 organismal health: a primer. *EMBO Mol. Med.* **15**, e16427 (2023).
1281 73. Birchenough, G. M. H. *et al.* Muc2-dependent microbial colonization of the jejunal mucus layer is diet
1282 sensitive and confers local resistance to enteric pathogen infection. *Cell Rep.* **42**, 112084 (2023).
1283 74. Zhao, Y. G., Codogno, P. & Zhang, H. Machinery, regulation and pathophysiological implications of
1284 autophagosome maturation. *Nat. Rev. Mol. Cell Biol.* **22**, 733–750 (2021).

1285 75. Treuting, P. M., Arends, M. J. & Dintzis, S. M. 11 - Upper Gastrointestinal Tract. in *Comparative*
1286 *Anatomy and Histology (Second Edition)* (eds Treuting, P. M., Dintzis, S. M. & Montine, K. S.) 191–
1287 211 (Academic Press, San Diego, 2018). doi:10.1016/B978-0-12-802900-8.00011-7.
1288 76. Larsson, N.-G. *et al.* Mitochondrial transcription factor A is necessary for mtDNA maintance and
1289 embryogenesis in mice. *Nat. Genet.* **18**, 231–236 (1998).
1290 77. Gong, G. *et al.* Parkin-mediated mitophagy directs perinatal cardiac metabolic maturation in mice.
1291 *Science* **350**, aad2459 (2015).
1292 78. Kawamura, N. *et al.* Delivery of endosomes to lysosomes via microautophagy in the visceral endoderm
1293 of mouse embryos. *Nat. Commun.* **3**, 1071 (2012).
1294 79. Schneider, C. A., Rasband, W. S. & Eliceiri, K. W. NIH Image to ImageJ: 25 years of image analysis.
1295 *Nat. Methods* **9**, 671–675 (2012).
1296 80. Stirling, D. R. *et al.* CellProfiler 4: improvements in speed, utility and usability. *BMC Bioinformatics* **22**,
1297 433 (2021).
1298 81. Subramanian, A. *et al.* Gene set enrichment analysis: A knowledge-based approach for interpreting
1299 genome-wide expression profiles. *Proc. Natl. Acad. Sci.* **102**, 15545–15550 (2005).
1300 82. Yu, G., Wang, L.-G., Han, Y. & He, Q.-Y. clusterProfiler: an R Package for Comparing Biological
1301 Themes Among Gene Clusters. *OMICS J. Integr. Biol.* **16**, 284–287 (2012).
1302 83. Walter, W., Sánchez-Cabo, F. & Ricote, M. GOplot: an R package for visually combining expression
1303 data with functional analysis. *Bioinformatics* **31**, 2912–2914 (2015).
1304

1305 **METHODS**

1306 **KEY RESOURCES TABLE**

REAGENT or RESOURCE	SOURCE	IDENTIFIER
Antibodies		
Mouse monoclonal anti-GFP, HRP-conjugated (clone GG4-2C2.12.10)	Miltenyi Biotec	130-091-833
Rat monoclonal anti-RFP (clone 5F8)	Chromotek	5F8
Rabbit polyclonal anti-USP7	Bethyl	A300-033A
Rabbit polyclonal anti-ATG16L1	MBL	PM040
Mouse monoclonal anti-LC3C (clone E5Q2K)	CST	83506
Rabbit polyclonal anti-Actin	Sigma	A2103
Mouse monoclonal anti-SQSTM1 (clone 2C11)	Abnova	H00008878-M01
Mouse monoclonal anti-Dab2 (clone 52/p96)	BD Biosciences	610464
Rat monoclonal anti-LAMP1 (clone 1D4B)	DSHB	1D4B
Rabbit polyclonal anti-Trehalase	GeneTex	GTX109979
Rabbit polyclonal anti-β-catenin	Santa Cruz Biotechnology	sc-7199
Rabbit polyclonal anti-Parkin	Abcam	ab15494
Rabbit polyclonal anti-MafB	Novus Biologicals	NBP1-81342
Rabbit polyclonal anti-Blimp1	Invitrogen	PA5-20310
Mouse monoclonal anti-E-Cadherin (clone 36/E)	BD Biosciences	610181
Goat polyclonal anti-GPX3	R&D Systems	AF4199
Mouse monoclonal anti-MTCO1 (clone 1D6E1A8)	Thermo Fisher Scientific	459600
Rabbit monoclonal anti-Olfm4 (clone D6Y5A)	CST	39141
Rabbit polyclonal anti-Lysozyme	Dako	A0099
Alexa Fluor 647 rabbit monoclonal anti-ASS1 (clone EPR12398)	Abcam	ab311083
Rat monoclonal anti-CD16/32 (clone 93)	Biolegend	101330
PerCP-eFluor710 rat monoclonal anti-EpCAM (clone G8.8)	Invitrogen	46-5791-82

APC rat monoclonal anti-EpCAM (clone G8.8)	Biolegend	118214
BV605 rat monoclonal anti-EpCAM (clone G8.8)	Biolegend	118227
Pacific Blue rat monoclonal anti-CD24 (Clone M1/69)	Biolegend	101820
PE rat monoclonal anti-c-Kit (clone 2B8)	Biolegend	105807
BV785 rat monoclonal anti-c-Kit (clone 2B8)	Biolegend	105841
Alexa Fluor 700 rat monoclonal anti-CD11b (clone M1/70)	Biolegend	101222
Biotin rat monoclonal anti-CD11c (clone N418)	Biolegend	105841
APC-Fire810 rat monoclonal anti-B220 (clone RA3-6B2)	Biolegend	103278
APC-Fire810 rat monoclonal anti-CD4 (clone GK1.5)	Biolegend	100480
RY586 rat monoclonal anti-CD4 (clone GK1.5)	BD Biosciences	568162
Biotin rat monoclonal anti-CD19 (clone 6D5)	Biolegend	115504
Biotin rat monoclonal anti-CD3e (clone 145-2C11)	Biolegend	79751
Biotin rat monoclonal anti-CD45.2 (clone 104)	Biolegend	109804
Rabbit polyclonal anti-GLS	Thermo Fisher Scientific	PA5-35365
Alexa Fluor 647 rabbit monoclonal anti-HK1 (clone EPR10134(B))	Abcam	ab197864
Alexa Fluor 488 mouse monoclonal anti-CPT1A (clone 8F6AE9)	Abcam	ab171449
Rabbit monoclonal anti-ACAC (clone EPR23235-147)	Abcam	ab269273
Alexa Fluor 488 rabbit monoclonal anti-CS (clone EPR8067)	Abcam	ab197488
PE rabbit monoclonal anti-IDH2 (clone EPR7577)	Abcam	ab212122
Alexa Fluor 594 rabbit monoclonal anti-ATP5A (clone EPR23235- 147)	Abcam	ab216385
BB700 rat monoclonal anti-BLIMP1 (clone 5E7)	BD Biosciences	567830
Alexa Fluor 488 donkey polyclonal anti-mouse IgGs	Thermo Fisher Scientific	A-21202
Alexa Fluor 488 donkey polyclonal anti-rabbit IgGs	Thermo Fisher Scientific	A-21206
Alexa Fluor 488 donkey polyclonal anti-rat IgGs	Thermo Fisher Scientific	A-21208
Alexa Fluor 555 donkey polyclonal anti-mouse IgGs	Thermo Fisher Scientific	A-31570
Alexa Fluor 647 donkey polyclonal anti-rabbit IgGs	Thermo Fisher Scientific	A-31573
Alexa Fluor 647 donkey polyclonal anti-mouse IgGs	Thermo Fisher Scientific	A-31571
Peroxidase AffiniPure donkey polyclonal Anti-Mouse IgG	Jackson Immunoresearch	715-035-151
HRP donkey anti-rabbit IgG	Cytiva	NA934
Peroxidase AffiniPure goat polyclonal Anti-Rat IgG	Jackson Immunoresearch	112-035-003
Chemicals, peptides, and recombinant proteins		
Tamoxifen	Merck	T5648
Leupeptin	Sigma	L2884
Hydrogen Peroxide 30%	Merck	108597
Dextran rhodamine B, 10000MW, neutral	Invitrogen	D1824
Dextran Alexa Fluor 647, 10000MW, anionic, fixable	Invitrogen	D22914
Paraformaldehyde, powder, TECHNICAL	VWR Chemicals	28794.295
Tissue-Tek O.C.T. Compound	Sakura	4583
Sucrose	Merck	1076511000
DAPI	Merck	268298
Phalloidin Alexa Fluor™ 488	ThermoFisher	A12379
Phalloidin Alexa Fluor™ 647	ThermoFisher	A22287

ProLong™ Glass Antifade Mountant	Thermo Fisher	P36984
Ghost Dye Violet 540	TONBO Biosciences	13-0879-T100
Ghost Dye Red 780	TONBO Biosciences	13-0865-T100
Streptavidin-BV421	Biolegend	405225
CM-H2DCFDA	Invitrogen	C6827
MitoTracker Green FM	Invitrogen	M7514
MitoTracker Red CMXRos	Invitrogen	M7512
MitoSOX	Invitrogen	M36008
LysoTracker Green DND-26	Invitrogen	L7526
eBioscience FOXP3/Transcription Factor Staining Buffer Set	Invitrogen	00-5523-00
ECL Western Blotting Reagents	Cytiva	RPN2106
DTT	Thermo Scientific	R0861
Oligonucleotides		
Genotyping primers for *Atg16l1*$^{fl/fl}$: forward: 5' CTTTCTCAACAGAACCAGCAGTAC 3'	IDT	N/A
Genotyping primers for *Atg16l1*$^{fl/fl}$: reverse: 5' GTTCAGGTCAATCACCAACTGAGC 3'	IDT	N/A
Genotyping primers for *Tfam*$^{fl/fl}$: forward: 5' CTGCCTTCCTCTAGCCCGGG 3'	IDT	N/A
Genotyping primers for *Tfam*$^{fl/fl}$: reverse: 5' GTAACAGCAGACAACTTGTG 3'	IDT	N/A
Genotyping primers for *Tfam*$^{fl/fl}$: reverse-2: 5' CTCTGAAGCACATGGTCAAT- 3'	IDT	N/A
Genotyping primers for *Villin-creER*^{T2}: forward: 5'- CAAGCCTGGCTCGACGGCC -3'	Sigma	N/A
Genotyping primers for *Villin-creER*^{T2}: reverse: 5'-CGCGAACATCTTCAGGTTCT-3'	Sigma	N/A
Genotyping primers for m*ito-QC*: forward: 5'- CAAAGACCCCAACGAGAAGC -3'	IDT	N/A
Genotyping primers for *mito-QC*: forward-2: 5'- CCCAAGGCACACAAAAAACC -3'	IDT	N/A
Genotyping primers for *mito-QC*: reverse: 5'-CTCTTCCCTCGTGACCTGCAACTCC-3'	IDT	N/A
Genotyping primers for *mito-QC*: reverse-2: 5'- CATGTCTTTAATCTACCTCGATGG -3'	IDT	N/A
Genotyping primers for *GFP-LC3*: forward: 5'-ATAACTTGCTGGCCTTTCCACT -3'	IDT	N/A
Genotyping primers for *GFP-LC3*: reverse: 5'- CGGGCCATTTACCGTAAGTTAT-3'	IDT	N/A
Genotyping primers for *GFP-LC3*: reverse-2: 5'-GCAGCTCATTGCTGTTCCTCAA-3'	IDT	N/A
RT-qPCR primers for *Atg16l1*: forward: 5' ACATGATGGTGCGTGGAATG 3'	Sigma	N/A
RT-qPCR primers for *Atg16l1*: reverse: 5' TCCTTGTCCTTCTGCTGCAT 3'	Sigma	N/A
RT-qPCR primers for *Tfam*: forward: 5' CAGGAGGCAAAGGATGATTC 3'	Sigma	N/A
RT-qPCR primers for *Tfam*: reverse: 5' CCAAGACTTCATTTCATTGTCG 3'	Sigma	N/A
RT-qPCR primers for *Dab2*: forward: 5' CGAAAGCGCCATCAAAGAAG 3'	IDT	N/A

RT-qPCR primers for *Dab2*: reverse: 5' CCTTTGAACCTGGCCAACAA 3'	IDT	N/A
RT-qPCR primers for *Mcoln3*: forward: 5' ATGGAGTTCATCAACGGGTG 3'	IDT	N/A
RT-qPCR primers for *Mcoln3*: reverse: 5' ATAGTTGACGTCCCGAGAAG 3'	IDT	N/A
RT-qPCR primers for *Lamp2*: forward: 5' TGCAGAATGGGAGATGAATTT 3'	IDT	N/A
RT-qPCR primers for *Lamp2*: reverse: 5' GGCACTATTCCGGTCATCC 3'	IDT	N/A
RT-qPCR primers for *Ctsl1*: forward: 5' CCAGCTACACAACGGGGAAT 3'	IDT	N/A
RT-qPCR primers for *Ctsl1*: reverse: 5' AGCATCAGCGGTTCCTGAAA 3'	IDT	N/A
RT-qPCR primers for *Bnip3*: forward: 5' TGTTGGATGCCCAGCATGAA 3'	IDT	N/A
RT-qPCR primers for *Bnip3*: reverse: 5' AATCTTCCTCAGACAGAGTGCT 3'	IDT	N/A
RT-qPCR primers for *Prkn*: forward: 5' AAACCGGATGAGTGGTGAGT 3'	IDT	N/A
RT-qPCR primers for *Prkn*: reverse: 5' AGCTACCGACGTGTCCTTGT 3'	IDT	N/A
RT-qPCR primers for *Pink1*: forward: 5' GCTGATCGAGGAGAAGCAG 3'	IDT	N/A
RT-qPCR primers for *Pink1*: reverse: 5' GATAATCCTCCAGACGGAAGC 3'	IDT	N/A
RT-qPCR primers for *Mafb*: forward: 5' AGAGGCGGACCCTGAAAAAC 3'	IDT	N/A
RT-qPCR primers for *Mafb*: reverse: 5' GTTTTCTCGGAAGCCGTTGC 3'	IDT	N/A
RT-qPCR primers for *c-maf*: forward: 5' GCATGCTGGACATGTATGGT 3'	IDT	N/A
RT-qPCR primers for *c-maf*: reverse: 5' ATGTACAACGGGAGGCTGAA 3'	IDT	N/A
RT-qPCR primers for *Blimp1*: forward: 5' TTCTTGTGTGGTATTGTCGGGACTT 3'	Sigma	N/A
RT-qPCR primers for *Blimp1*: reverse: 5' TTGGGGACACTCTTTGGGTAGAGTT 3'	Sigma	N/A
RT-qPCR primers for *Ass1*: forward: 5' CATTGGAATGAAGTCCCGAG 3'	IDT	N/A
RT-qPCR primers for *Ass1*: reverse: 5' GATTTTGCGTACTTCCCGAT 3'	IDT	N/A
RT-qPCR primers for *Glb1*: forward: 5' ACTGCTGCAACTGCTGGG 3'	Sigma	N/A
RT-qPCR primers for *Glb1*: reverse: 5' AATGGCTGTCCATCCTTGAG 3'	Sigma	N/A
RT-qPCR primers for *Treh*: forward: 5' GCACCTGCTGCTTCTGCT 3'	Sigma	N/A
RT-qPCR primers for *Treh*: reverse: 5' CATCTGAACTTGGTGCAGGA 3'	Sigma	N/A
RT-qPCR primers for *Sis*: forward: 5' GCCCACGCGTTTGGTGAGAC 3'	Sigma	N/A
RT-qPCR primers for *Sis*: reverse: 5' ATCAGCAGTGCAGGGCCCCA 3'	Sigma	N/A

RT-qPCR primers for *Arg2*: forward: 5' TGATTGGCAAAAGGCAGAGG 3'	Sigma	N/A
RT-qPCR primers for *Arg2*: reverse: 5' CTAGGAGTAGGAAGGTGGTC 3'	Sigma	N/A
RT-qPCR primers for *Gpx3*: forward: 5' AATTAGGCACAAAGCCCCCA 3'	IDT	N/A
RT-qPCR primers for *Gpx3*: reverse: 5' CATTCTGGGCTTCCCTTCCA 3'	IDT	N/A
RT-qPCR primers for *Cat*: forward: 5' GAACGGCAATAGGGGTCCTC 3'	IDT	N/A
RT-qPCR primers for *Cat*: reverse: 5' TGGTACACGCAAAAGGAGCA 3'	IDT	N/A
RT-qPCR primers for *Amn*: forward: 5' ATCTGTGAGAGCCTCGGCG 3'	IDT	N/A
RT-qPCR primers for *Amn*: reverse: 5' GTTGGAGGCAGTATCGAAGGA 3'	IDT	N/A
RT-qPCR primers for *Mamdc4*: forward: 5' TCACCACTGCCAGAACAAGG 3'	IDT	N/A
RT-qPCR primers for *Mamdc4*: reverse: 5' CTAACTGGTTCCACGGTCCC 3'	IDT	N/A
RT-qPCR primers for *mt-Nd1*: forward: 5' TCCCCTACCAATACCACACC 3'	Sigma	N/A
RT-qPCR primers for *mt-Nd1*: reverse: 5' TGAAATTGTTTGGGCTACGG 3'	Sigma	N/A
RT-qPCR primers for *mt-Co2*: forward: 5' ACGAAATCAACAACCCCGTA 3'	Sigma	N/A
RT-qPCR primers for *mt-Co2*: reverse: 5' GGCAGAACGACTCGGTTATC 3'	Sigma	N/A
RT-qPCR primers for *Sdha*: forward: 5' GCGGCTTTCACTTCTCTGTT 3'	IDT	N/A
RT-qPCR primers for *Sdha*: reverse: 5' CTCAGAAAGGCCAAATGCAG 3'	IDT	N/A
qPCR primers for *mt-Co1*: forward: 5' ATCCCTTGACATCGTGCTTC 3'	Sigma	N/A
qPCR primers for *mt-Co1*: reverse: 5' AAGTGGGCTTTTGCTCATGT 3'	Sigma	N/A
qPCR primers for *mt-Atp6*: forward: 5' ACAGGCTTCCGACACAAACT 3'	Sigma	N/A
qPCR primers for *mt-Atp6*: reverse: 5' GGTAGCTGTTGGTGGGCTAA 3'	Sigma	N/A
qPCR primers for *Hk2*: forward: 5' GCCAGCCTCTCCTGATTTTAGTGT 3'	Sigma	N/A
qPCR primers for *Hk2*: reverse: 5' GGGAACACAAAAGACCTCTTCTGG 3'	Sigma	N/A
RT-qPCR primers for *Ppib*: forward: 5' CACCAATGGCTCACAGTTCTT 3'	IDT	N/A
RT-qPCR primers for *Ppib*: reverse: 5' ATGACATCCTTCAGTGGCTTG 3'	IDT	N/A

Mice

Atg16l1$^{fl/fl}$[33], *Tfam*$^{fl/fl}$ [76], and GFP-LC3[26] mice were kindly provided by N. Martínez-Martín (Centro de Biología Molecular "Severo Ochoa", CBM, CSIC-UAM, Madrid, Spain). The *mito*-QC mouse line[42] was obtained from P. Boya (Centro de Investigaciones Biológicas Margarita Salas, CSIC, Madrid, Spain; University of

1312 Fribourg, Switzerland). *Villin-creER*^{T2} mice[34] were provided by N. Djouder (Spanish National Cancer
1313 Research Centre, CNIO, Madrid, Spain). *Atg16l1* $^{fl/fl}$, *Tfam* $^{fl/fl}$ mice were crossed at the CBM animal facility
1314 with *Villin-creER*^{T2} mice to generate intestinal epithelial-specific conditional knockout (cKO) mice:
1315 *Atg16*cKO and *Tfam*cKO, respectively. In turn, *Atg16*cKO mice were crossed with *mito*-QC mice to establish
1316 *the mQ-Atg16*cKO mouse line. Tamoxifen (0.12–0.5 mg in corn oil containing 10% ethanol) was
1317 administered subcutaneously at postnatal days 1 and 2 to pups from *Atg16*cKO, *mQ-Atg16*cKO, and
1318 *Tfam*cKO litters, following a protocol similar to that described by Gong et al.[77]. Cre-positive animals were
1319 classified as KO, and Cre-negative mice as WT. To confirm the absence of spontaneous recombination in
1320 WT mice, expression levels of Atg16l1 and Tfam were assessed by Western blot and RT-qPCR. Mice were
1321 genotyped by PCR using DNA extracted from tail biopsies following standard protocols. Genotyping primers
1322 are listed in the Key Resources Table. Neonatal mice were humanely sacrificed by decapitation; adult mice
1323 were euthanized via CO_2 inhalation. *Tfam*cKO neonates were sacrificed after two consecutive days without
1324 weight gain or upon observing approximately a 10% weight loss, in accordance with humane endpoint
1325 criteria. No test was performed to determine the influence of sex, as no apparent differences were found.
1326 Mouse colonies were maintained at CBM under specific pathogen-free conditions and on a C57BL/6 genetic
1327 background. Mice were housed four/five per cage with food and water available ad libitum and maintained
1328 in a temperature-controlled environment on a 12 h–12 h light–dark cycle with light onset at 08:00. Animal
1329 experiments were performed under protocols approved by the CBM and Comunidad Autónoma de Madrid
1330 ethical committees under the following protocol approval number (PROEX 307.2/21). All animal procedures
1331 conformed to EU Directive 86/609/EEC and Recommendation 2007/526/EC regarding the protection of
1332 animals used for experimental and other scientific purposes, enforced in Spanish law under Real Decreto
1333 1201/2005.
1334
1335 **mCherry / fluorescent-dextran uptake assay**
1336 Mice from GFP-LC3, *Atg16*cKO, and *Tfam*cKO lines were fasted for 1 hour and orally gavaged with either
1337 mCherry or 10 kDa fluorescent-dextran (0.3–1 mg/ml in PBS; 10 µl/g body weight). Following gavage, mice
1338 were sacrificed either 3 or 16 hours later, adapted from the protocol reported by Remis et al.[12]. To test the
1339 endocytic function in neonatal enterocytes, WT mice at postnatal day 7 (P7) were sequentially gavaged
1340 with two distinct 10 kDa fluorescent-dextrans (0.7 mg/ml in PBS; 10 µl/g body weight), following a modified
1341 version of the protocol established in mouse embryos by Kawamura et al.[78]. After a 1-hour fasting period,
1342 pups were first gavaged with Alexa Fluor 647-dextran and then returned to their mother. Three hours later,
1343 they were given rhodamine B–dextran again. Pups were subsequently sacrificed either 1 or 5 hours after
1344 the second gavage, and ileal enterocytes were analysed by confocal microscopy to assess dextran uptake
1345 and intracellular localization.
1346
1347 **Leupeptin and hydrogen peroxide treatment**

1348 To inhibit lysosomal proteases and block autophagy, mice were injected subcutaneously with 40 mg/Kg
1349 leupeptin (Sigma) dissolved in PBS and sacrificed after 16h[43]. To assess the effect of ROS on intestinal
1350 epithelial maturation, mice were injected intraperitoneally with hydrogen peroxide (5.1 µmol/g body weight;
1351 Merck) once daily from P5 to P12 (day of sacrifice), following a protocol adapted from Liang et al.[60].
1352

1353 **Histology and Immunofluorescence**

1354 Portions of the distal small intestine from mice were fixed in 4% PFA for 16 hours at 4 °C, embedded in
1355 paraffin resin, and cut transversely into 5-µm sections. Some samples were stained with hematoxylin-eosin
1356 (HE&E; Sigma and Merck, respectively), while others underwent Periodic Acid-Schiff (PAS) staining.
1357 Additionally, some samples were used for immunofluorescence. For immunofluorescence, sections were
1358 deparaffinized using xylene and then rehydrated through a series of decreasing ethanol concentrations
1359 (100%, 96%, 70%, 50%). For antigen retrieval, tissue was boiled at 100 °C on a heat block in sodium citrate
1360 buffer (10 mM Sodium citrate, 0.05% Tween 20, pH 6.0) for 20 min. Next, the slides were washed with
1361 water and PBS containing calcium and magnesium, and then incubated for 1 hour at room temperature
1362 with 3% bovine serum albumin (BSA) as a blocking solution. For O.C.T. embedded sections, portions of
1363 the distal small intestine were previously fixed in 4% PFA for 16 hours at 4 °C, incubated in 30% sucrose
1364 in PBS for 48-72 hours at 4 °C, and then embedded in O.C.T. compound and stored at -80 °C until use.
1365 O.C.T. blocks were cut transversely into 15 µm sections using Superfrost Plus Adhesion Microscope Slides
1366 (Epredia) and stored at -80 °C. For immunofluorescence, sections were dried at room temperature for 30
1367 minutes, washed with 0.1% Tween 20, and blocked for 1 hour at room temperature with BGT buffer (0.3%
1368 BSA, 0.75% Glycine, 0.3% Triton X-100 in PBS). For both paraffin-embedded and O.C.T.-embedded
1369 samples, the primary antibody was added and incubated overnight at 4 °C in the respective blocking buffer.
1370 After washing with PBS, the secondary antibody was incubated with DAPI for 1h at RT. Lastly, slides were
1371 assembled with coverslips with Prolong Glass Antifade (Thermo Fisher). Antibodies used are specified in
1372 the key resources table.
1373

1374 **Image Acquisition and Analysis**

1375 HE&E and PAS staining images were acquired using an Axio Imager M1 vertical wide-field microscope,
1376 coupled with a Leica DMC6200 CMOS Colour camera. The objective used was 10X/0.3 Air EC Plan-Neo.
1377 LASXv4.13 software was used to stitch the tiles into an image. The analysis of goblet cells, villi length, and
1378 submucosa–lower mucosa thickness was performed using Fiji (ImageJ 1.54f; https://fiji.sc/) (Wayne
1379 Rasband, NIH, USA)[79]. Lower mucosa was defined as the sum of the *muscularis mucosae*, *lamina propria*
1380 and epithelial compartment of the crypts. For villi length analysis, the 10 longest villi per section were
1381 chosen. One section per mouse was analysed from 3–6 mice per genotype. For immunofluorescence,
1382 images were acquired using a Zeiss LSM 900 confocal microscope mounted on an Axio Imager Z2 upright
1383 stand, with sequential acquisition and bidirectional scanning. For individual fields, a 63×/1.4 NA oil-
1384 immersion Plan-Apochromat objective was used, with a voxel size of 50 × 50 × 520 nm. For tile scans,

1385 images were acquired using a 20×/0.8 NA air Plan-Apochromat objective, with a voxel size of 0.624 × 0.624
1386 × 1.9 µm, and stitched using ZEN Blue software version 3.4 (Zeiss; https://www.zeiss.com/zen). For the
1387 analysis of Paneth cells and Olfm4^{+} crypts in the ileum of *Tfam*cKO mice, all cells and all crypts were
1388 quantified per section (one section per mouse; 3 mice per genotype). For intensity analysis, all images were
1389 acquired with 16-bit resolution and under the same conditions. An average intensity projection was made,
1390 and the endothelial cells (lacteal vessel) were cropped. The same threshold was applied to all images to
1391 select positive areas. Images were analysed using CellProfiler 4.2.8 (https://cellprofiler.org/)[80] and Fiji
1392 (ImageJ 1.54f)[79]. Intensity values correspond to the integrated density, normalized to the epithelial nuclear
1393 area (defined by DAPI in epithelial cells) for BLIMP1 and MAFB, or to the epithelial area (delimited by β-
1394 catenin, E-cadherin, or F-actin) for all other markers, except for LAMP1 (in both KO models) and Rd-dextran
1395 (only in *Atg16*cKO mice), which were not normalized. For LAMP1 intensity and area analysis in *Tfam*cKO
1396 mice, images were deconvolved using Huygens Professional software (version 24.10; Scientific Volume
1397 Imaging, https://svi.nl/Huygens-Professional). For the analysis of Rd-dextran intensity and LAMP1 area and
1398 intensity in *Atg16*cKO mice, 25–40 and 26–36 enterocytes per condition were analysed, respectively. For
1399 LAMP1 area and intensity analysis in *Tfam*cKO mice, a minimum of 30 enterocytes per mouse were
1400 quantified, across 3 mice per group (99–167 enterocytes per group). For all other intensity analyses, 2–5
1401 random images per mouse were acquired from comparable villi, each containing approximately 50 cells,
1402 with 2–5 mice per group.
1403
1404 **Transmission Electron Microscopy**
1405 Samples were processed by the Electron Microscopy Unit at CBM. Distal small intestine portions were fixed
1406 using 4% PFA (paraformaldehyde) and 2% glutaraldehyde in phosphate buffer 0.1M, pH 7.4, for 2 hours at
1407 room temperature. Then they were washed 3 times for 10 minutes with phosphate buffer. After fixation, the
1408 material was post-fixed in 1% osmium tetroxide and potassium ferricyanide for 1 hour at 4 °C, then
1409 embedded in tannic acid for 1 minute and block-stained with 2% uranyl acetate for 1 hour in the dark. Next,
1410 they were dehydrated in crescent concentrations of ethanol (30%, 50%, 70%, 95%, 3x100%; 10 minutes
1411 each) and infiltrated in propylene oxide for 45 minutes and Epon 100% for 1 hour. Finally, the samples were
1412 introduced into BEEM capsules (ESBE Scientific). Samples were observed using a JEM1400 Flash
1413 Transmission Electron Microscope (JEOL) equipped with a CMOS OneView camera (Gatan). Fiji (ImageJ
1414 1.54f)[79] was used for image analysis. Mitochondria were classified into three categories, as in Moschandrea
1415 et al.[44]: class I (normal), characterized by mitochondria with narrow and well-defined cristae; class II (partly
1416 affected), with mitochondria exhibiting undefined cristae; and class III (damaged), including mitochondria
1417 with wide, short, and less electron-dense cristae, or those with ruptured membranes or internal inclusions.
1418 For the analysis of mitochondrial status in *Atg16*cKO mice, 291–340 mitochondria were analysed from 10–
1419 11 enterocytes (3 mice per genotype). For *Tfam*cKO mice, in the analysis of number and percentage of
1420 mitochondrial classes, 444–1040 mitochondria from 13–24 enterocytes (3–4 mice per group) were used;

1421 for area and aspect ratio analysis, 261–520 mitochondria from 11–17 enterocytes (2–4 mice per group)
1422 were analysed. The graphs show data after outlier exclusion.
1423
1424 **Isolation of IEC**
1425 Mice were euthanized, and the abdominal cavity was opened to expose the intestine. The region of interest
1426 (proximal or distal intestine) was dissected, removed, and rinsed in PBS. The tissue was cut transversely
1427 into ~5 mm fragments, which were then opened longitudinally and incubated in epithelial dissociation buffer
1428 (1 mM DTT, 1 mM EDTA, 2% FBS in PBS) at 37°C with agitation for 20 minutes. After incubation, the
1429 samples were centrifuged at 1200 rpm for 5 minutes. The supernatant was discarded, and the pellet was
1430 resuspended in 10 mL of DMEM supplemented with 10% FBS at 4 °C. The suspension was passed through
1431 70 µm cell strainers (Falcon) and then centrifuged again at 1,200 rpm for 5 minutes. The resulting pellet
1432 was resuspended in FACS buffer (1 mM EDTA, 2% FBS in PBS) at 4 °C and centrifuged again under the
1433 same conditions. The final pellet containing epithelial cells was used for western blotting, flow cytometry,
1434 and RT-qPCR analysis.
1435
1436 **Immunoblotting**
1437 IECs pellets were lysed with lysis buffer (50 mM Tris-HCl, 150 mM NaCl, 1% NP-40, 50 mM NaF, 0.1%
1438 SDS, 1 mM Na_3VO_4, 30 mM β-glycerophosphate, 5 mM EDTA, protease inhibitors) and centrifuged for 10
1439 minutes at 4 °C, 15,000 rpm. Supernatants were collected and quantified using the Bradford protein assay
1440 (Biorad Protein Assay, Biorad). 25 µg of protein was loaded in 10 or 12% acrylamide gels for SDS-PAGE.
1441 After electrophoresis, proteins were transferred to an Immobilon-P transfer membrane (Millipore), blocked
1442 for 1 hour, and incubated overnight with primary antibodies at 4 °C. After washing with 0.05% Tween 20,
1443 they were incubated with HRP-conjugated secondary antibodies for 1 hour at room temperature. ECL
1444 western blotting reagents (Cytiva) were used for the chemiluminescence reaction. Bands were analysed
1445 using Fiji (ImageJ 1.54f)[79]. Antibodies used are specified in the key resources table.
1446
1447 **Flow Cytometry**
1448 Disaggregated epithelial cells were plated into a 96-well plate and incubated with FACS buffer with anti-
1449 CD16/CD32 Fc block and viability markers (Ghost Dye) for 10 min at room temperature. After centrifugation,
1450 cells were incubated for 20 min at 4ºC with the appropriate combination of the antibodies in FACS buffer to
1451 discern between the different epithelial and immune populations. Following protocols adapted from
1452 immunometabolic [45,54] and intestinal studies[36], we assessed mitochondrial mass and membrane potential,
1453 cellular and mitochondrial ROS levels, and lysosomal content labelling cells with MitoTracker Green FM
1454 (50 nM), MitoTracker Red CMXRos (100 nM), CM-H2DCFDA (2.5 µM), MitoSOX (1 µM), and Lysotracker
1455 Green DND-26 (100 nM), respectively. Probes were incubated for 15 min at room temperature and 15 min
1456 at 37 °C in DMEM with 5% FBS (Lysotracker), without FBS (MitoTracker and CM-H2DCFDA), or in HBSS
1457 (MitoSOX). Antibodies used are specified in the key resources table. Data were acquired using a Cytek

1458 Aurora full-spectrum cytometer at the CBM, and analysed with FlowJo software (versions 10 and 10.8.1;
1459 BD Biosciences). See Figure S3 for details on the gating strategies.
1460
1461 **Met-flow cytometry staining**
1462 Based on recent works on immune cell metabolism[45,50], we selected eight key metabolic enzymes to
1463 analyse their expression by flow cytometry in our epithelial cells: ASS1, GLS, HK1, CPT1A, ACAC, CS,
1464 IDH2, and ATP5A. After the disaggregated epithelial cells were incubated with surface antibodies according
1465 to the flow cytometry protocol, they were fixed and permeabilized using the eBioscience
1466 Foxp3/Transcription Factor Staining Buffer Set (Invitrogen). Next, they were washed in the provided wash
1467 buffer and blocked with 20% FBS in wash buffer and incubated for 2h at room temperature with the
1468 appropriate antibodies to detect the rate-limiting enzymes from different metabolic pathways. Lastly, they
1469 were rewashed with wash buffer. Antibodies used are specified in the key resources table. Data were
1470 acquired using a Cytek Aurora full-spectrum cytometer at the CBM, and analysed with FlowJo software
1471 (versions 10 and 10.8.1; BD Biosciences).
1472
1473 **RNA Sequencing and Bioinformatic Analyses**
1474 The FACS gating strategy used to isolate LREs and PECs for RNA sequencing (RNA-seq) is shown in
1475 Figure S4A. Cell sorting was performed using a FACSAria Fusion cytometer (BD Biosciences). Each
1476 population was collected in biological triplicate samples of 300,000–500,000 cells. For LREs, each replicate
1477 consisted of pooled cells from multiple neonatal litters; for PECs, each replicate corresponded to a single
1478 mouse at postnatal day 42 (P42). Cells were collected in RLT buffer (Qiagen), and total RNA was extracted
1479 using the RNeasy Plus Micro Kit (Qiagen). Samples with an RNA integrity number (RIN) >7.0 were selected
1480 for RNA-seq. Ultra-low input poly(A)-selected libraries (single-end) were prepared in triplicate and
1481 sequenced using the Illumina HiSeq 2500 platform (50 bp, single-end reads) at the Centro de Análisis
1482 Genómico (CNAG-CRG, Barcelona, Spain). Reads were aligned to the Mus musculus reference genome
1483 (mm39) using HISAT2 (v2.1.0), and gene counts were obtained using HTSeq-count (v0.11.2). Differential
1484 gene expression analysis was performed with DESeq2. Gene Set Enrichment Analysis (GSEA)[81] was
1485 conducted using the clusterProfiler [82] and enrichplot packages within the R environment. Predefined gene
1486 sets from the Gene Ontology (GO) database were assessed for statistically significant enrichment based
1487 on a ranked list of gene expression values. The full gene dataset, annotated with ENSEMBL identifiers and
1488 their associated statistical metrics (stat), was utilized as input for the GSEA. Enrichment was quantified by
1489 normalized enrichment scores (NES), with significance determined at an adjusted p-value threshold of <
1490 0.05 following Benjamini-Hochberg correction. Over-Representation Analysis (ORA)[37] was performed in R
1491 using the clusterProfiler package. Differentially expressed genes (DEGs) with an adjusted p-value < 0.05
1492 and mapped using ENTREZID identifiers were used. Enriched GO terms and KEGG pathways were also
1493 filtered at an adjusted p-value < 0.05 (Benjamini-Hochberg correction). Selected GO and KEGG terms were
1494 visualized using bubble plots generated in R with the GOplot package (GOBubble function) [83]. The

1495 biocomputational data analysis was carried out by the Biocomputational Analysis Service (SABio) at the
1496 Centro de Biologia Molecular "Severo Ochoa" (CSIC-UAM).
1497
1498 **RNA Extraction, cDNA Synthesis, and RT-qPCR**
1499 Epithelial cells were lysed in 500 µL of TRIzol (Invitrogen) and stored at -80 °C until RNA extraction. RNA
1500 was isolated using the RNeasy Micro Kit (Qiagen) according to the manufacturer's instructions. For cDNA
1501 synthesis, 500 ng of RNA was reverse transcribed using the High-Capacity cDNA Reverse Transcription
1502 Kit (Applied Biosystems). Gene expression was assessed by quantitative PCR (qPCR) using gene-specific
1503 primer pairs (listed in Key Resources Table). Reactions were performed in 384-well plates using either the
1504 CFX384 Real-Time System (Bio-Rad) or the ABI 7900HT Fast Real-Time PCR System (Applied
1505 Biosystems), with SYBR Green Master Mix (Agilent, Santa Clara, CA). Each well contained 10 ng of cDNA
1506 and 2.5 µM of each primer in a final volume of 10 µL. All reactions were run in technical triplicates.
1507 Cyclophilin B (*Ppib*) was used as the reference gene for normalisation.
1508
1509 **mtDNA Quantification**
1510 Genomic DNA (gDNA) was extracted using the NZY Tissue gDNA Isolation Kit (NZYTech). Relative
1511 mitochondrial DNA (mtDNA) content was determined by qPCR using primers for the following mitochondrial
1512 genes: NADH dehydrogenase 1 (*mt-Nd1*), cytochrome c oxidase subunits 1 and 2 (*mt-Co1* and *mt-Co2*),
1513 and ATP synthase subunit 6 (*mt-Atp6*). Reactions were performed in 384-well plates using the CFX384
1514 Real-Time System (Bio-Rad) with SYBR Green Master Mix (Agilent, Santa Clara, CA). Each well contained
1515 10 ng of gDNA and 2.5 µM of each primer in a final volume of 10 µL. All reactions were run in technical
1516 triplicates. Hexokinase 2 (*HK2*) was used as the reference gene for normalization, with primers listed in the
1517 Key Resources Table.
1518
1519 **QUANTIFICATION AND STATISTICAL ANALYSIS**
1520 GraphPad software (versions 8.0.1 and 9.5.1) and Microsoft Excel were used for data analysis and plotting.
1521 Results shown are either representative or cumulative from at least two independent experiments. Except
1522 for gene expression analyses during development, RT-qPCR and WB data were normalized to the average
1523 of at least two WT or control mice of their corresponding litter. Sample size, statistical tests, and the meaning
1524 of the dots in each graph are specified in figure legends, except for TEM graphs (Figures 4C, 6F and S6O;
1525 samples sizes indicated in Table S1). In violin plots, median and interquartile range (IQR) are shown; in dot
1526 plots, mean ± SEM; in bar plots with dots, the mean + SEM; and in standard bar plots, the mean + SD.
1527 Outliers were identified using the ROUT method (Q = 5%) or Grubbs' test ($\alpha = 0.05$) for datasets with $n \geq$
1528 6. Normality was assessed using the Shapiro–Wilk test ($n < 50$) or the Kolmogorov–Smirnov test ($n > 50$).
1529 Statistical significance between two groups was determined using Student's t-test for parametric data or
1530 the Mann–Whitney test for nonparametric data. Welch's correction was applied when variances between
1531 groups were unequal. For comparisons among more than two groups, one-way ANOVA or two-way ANOVA

with Tukey's post hoc test was used for parametric data, and the Kruskal–Wallis test, followed by Dunn's multiple comparison test, was used for nonparametric data. Survival curves were compared using the Gehan–Breslow–Wilcoxon test. A critical value for significance of $p < 0.05$ was used throughout the study (*$p < 0.05$, **$p < 0.01$, ***$p < 0.001$, ****$p < 0.0001$). In Figures 1H, 2A, 2H, S5B–C, S6F–H, S7A, S7B, S7E, and Table S2, only the most relevant statistically significant comparisons are shown; non-significant results are not displayed. In all other figures, statistical significance is indicated only when differences are significant.

Figure 1

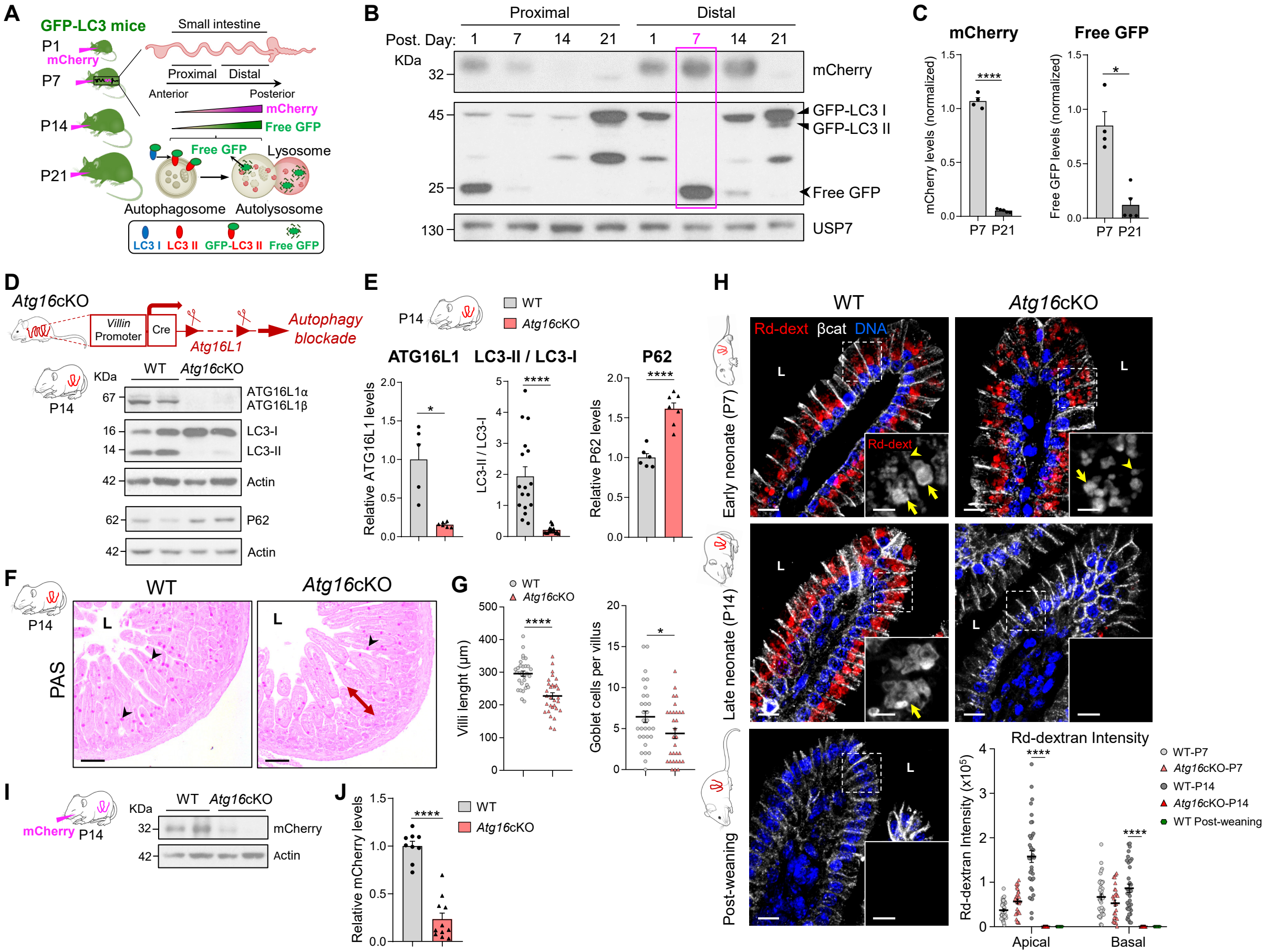
A
GFP-LC3 mice
P1
mCherry
P7
P14
P21
Small intestine
Proximal
Distal
Anterior
Posterior
mCherry
Free GFP
Free GFP
Lysosome
Autophagosome
Autolysosome
LC3 I
LC3 II
GFP-LC3 II
Free GFP
B
Proximal
Distal
Post. Day:
1
7
14
21
1
7
14
21
KDa
32
45
25
130
mCherry
GFP-LC3 I
GFP-LC3 II
Free GFP
USP7
C
mCherry
Free GFP
mCherry levels (normalized)
Free GFP levels (normalized)
****
*
P7
P21
D
Atg16cKO
Villin Promoter
Cre
Atg16L1
Autophagy blockade
P14
WT
Atg16cKO
KDa
67
16
14
42
62
42
ATG16L1α
ATG16L1β
LC3-I
LC3-II
Actin
P62
Actin
E
P14
WT
Atg16cKO
ATG16L1
LC3-II / LC3-I
P62
Relative ATG16L1 levels
LC3-II / LC3-I
Relative P62 levels
*
****
****
F
P14
WT
Atg16cKO
PAS
L
L
G
WT
Atg16cKO
Villi lenght (µm)
Goblet cells per villus
****
*
H
WT
Atg16cKO
Rd-dext
βcat
DNA
Early neonate (P7)
Late neonate (P14)
Post-weaning
L
Rd-dext
Rd-dextran Intensity
Rd-dextran Intensity (x10^5)
WT-P7
Atg16cKO-P7
WT-P14
Atg16cKO-P14
WT Post-weaning
****
****
Apical
Basal
I
mCherry
P14
KDa
WT
Atg16cKO
32
42
mCherry
Actin
J
Relative mCherry levels
WT
Atg16cKO
****

Figure 2

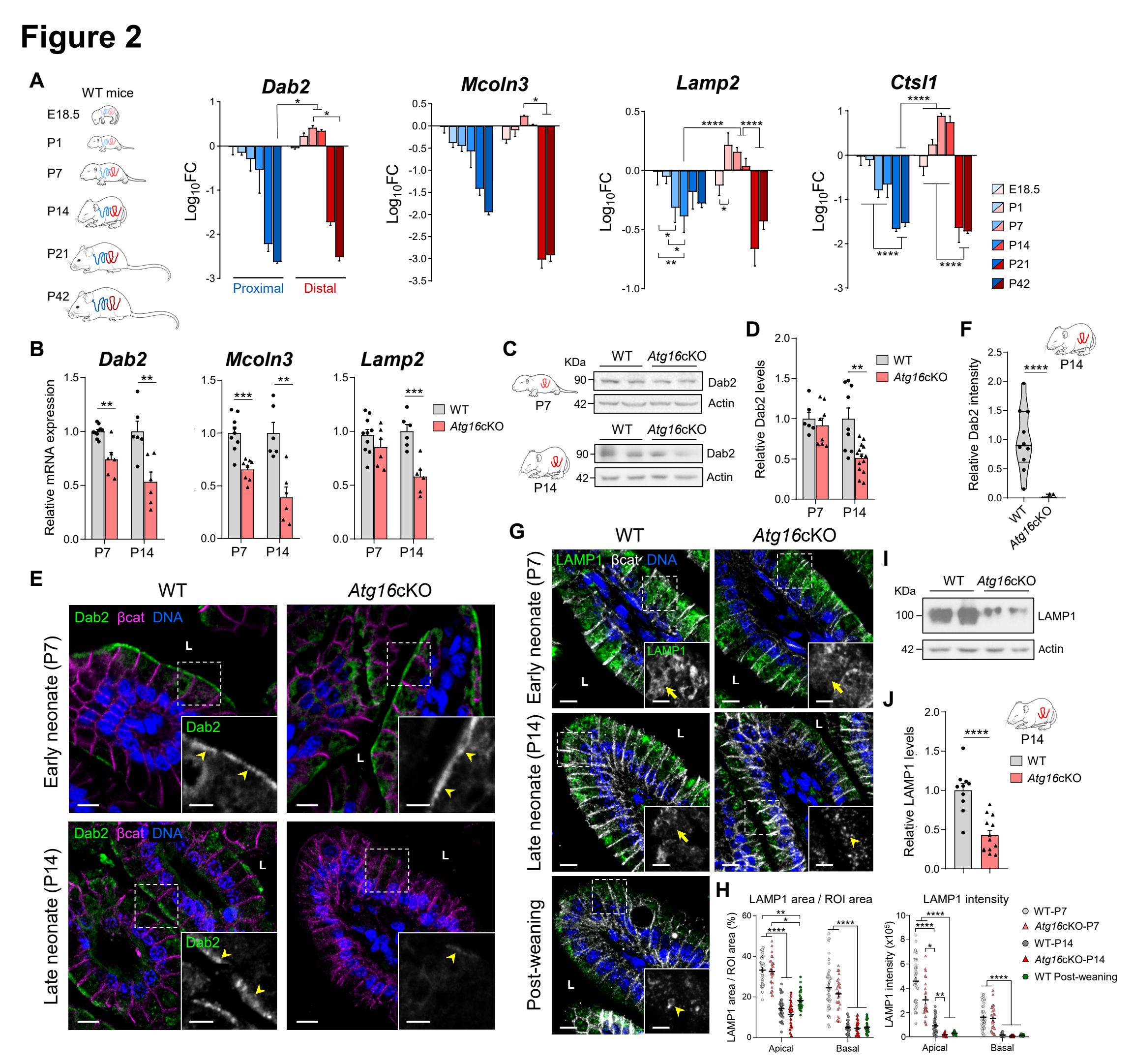
A
WT mice
E18.5
P1
P7
P14
P21
P42
Dab2
Mcoln3
Lamp2
Ctsl1
Log10FC
Proximal
Distal
E18.5
P1
P7
P14
P21
P42
B
Relative mRNA expression
WT
Atg16cKO
C
KDa
WT
Atg16cKO
90
42
Dab2
Actin
P7
P14
D
Relative Dab2 levels
F
Relative Dab2 intensity
WT
Atg16cKO
E
Dab2 βcat DNA
L
Early neonate (P7)
Late neonate (P14)
G
LAMP1 βcat DNA
LAMP1
Post-weaning
I
100
LAMP1
J
Relative LAMP1 levels
H
LAMP1 area / ROI area
LAMP1 intensity
LAMP1 intensity (x10^5)
Apical
Basal
WT-P7
Atg16cKO-P7
WT-P14
Atg16cKO-P14
WT Post-weaning

Figure 3

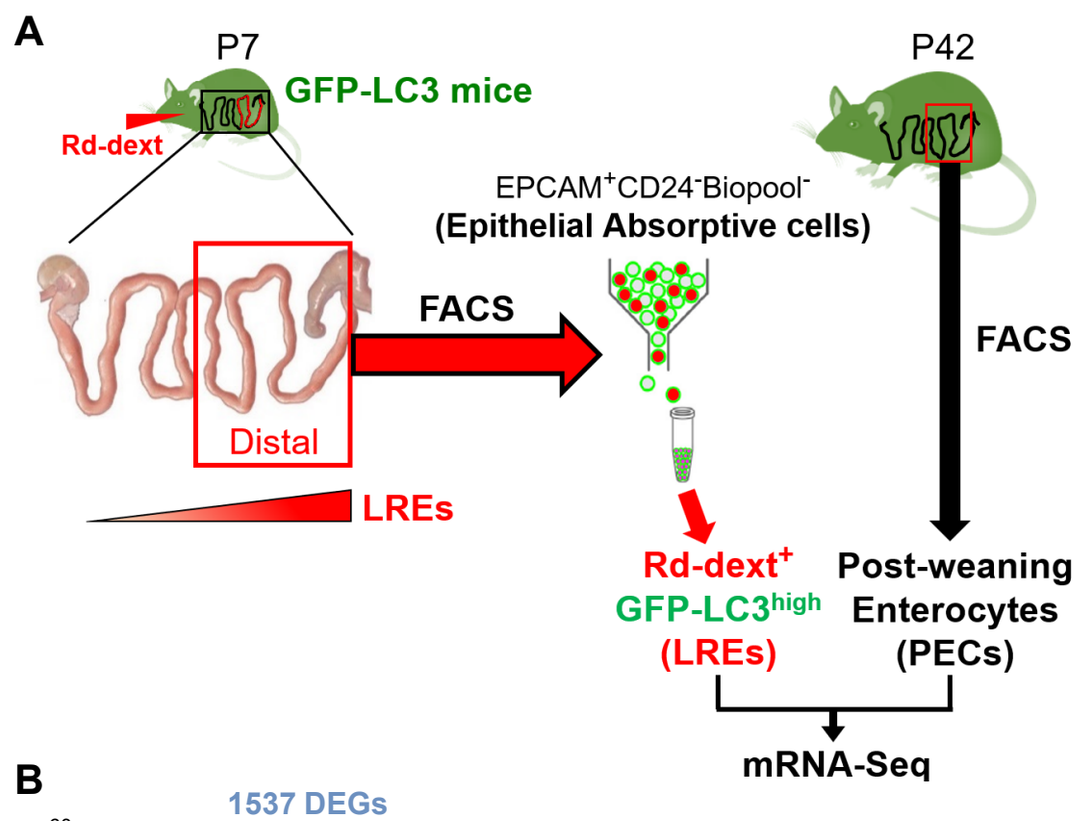
A
P7
GFP-LC3 mice
Rd-dext
Distal
LREs
FACS
EPCAM+CD24-Biopool-
(Epithelial Absorptive cells)
P42
FACS
Rd-dext+
GFP-LC3high
(LREs)
Post-weaning
Enterocytes
(PECs)
mRNA-Seq

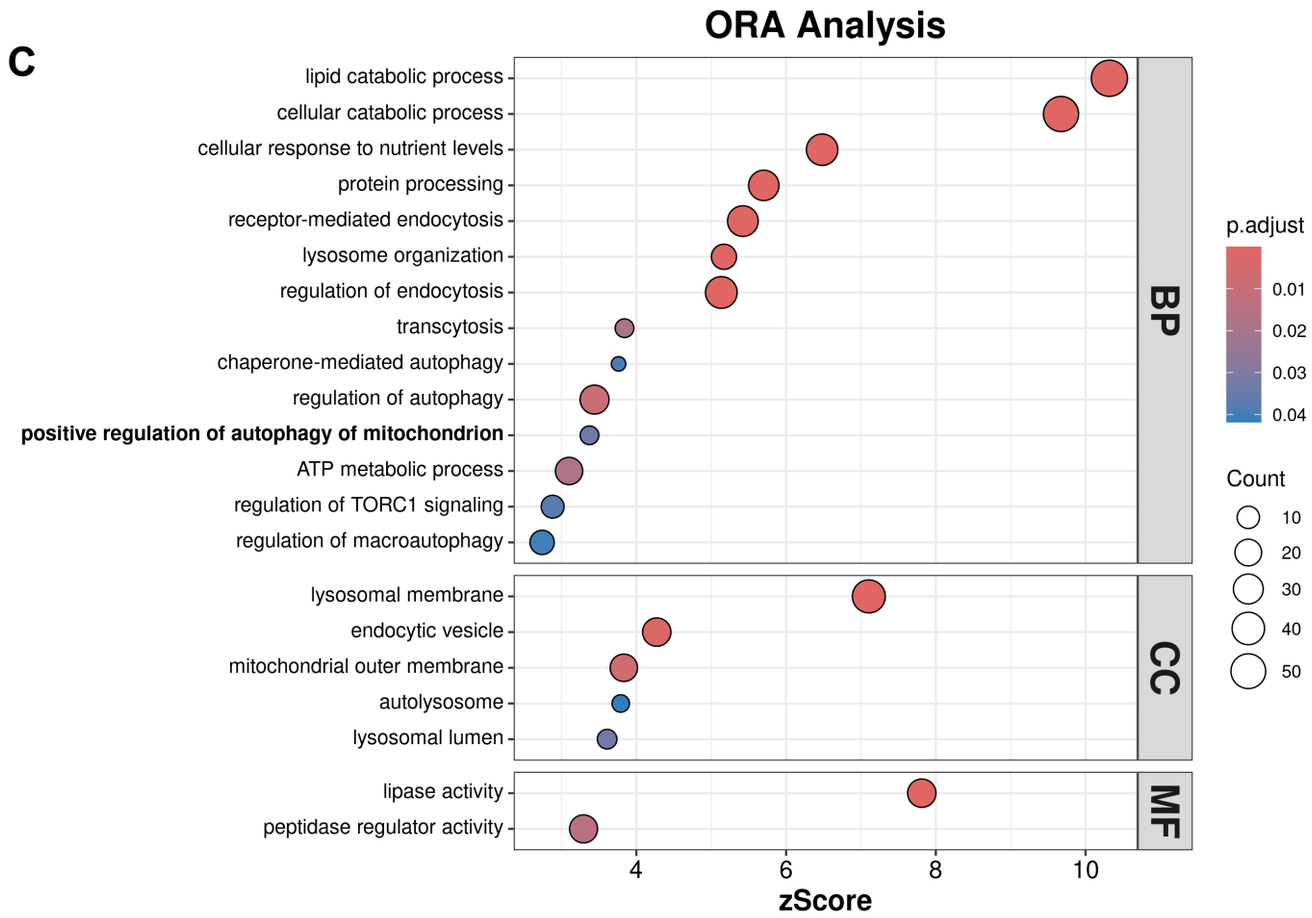
C
ORA Analysis
lipid catabolic process
cellular catabolic process
cellular response to nutrient levels
protein processing
receptor-mediated endocytosis
lysosome organization
regulation of endocytosis
transcytosis
chaperone-mediated autophagy
regulation of autophagy
positive regulation of autophagy of mitochondrion
ATP metabolic process
regulation of TORC1 signaling
regulation of macroautophagy
lysosomal membrane
endocytic vesicle
mitochondrial outer membrane
autolysosome
lysosomal lumen
lipase activity
peptidase regulator activity
BP
CC
MF
zScore
p.adjust
Count

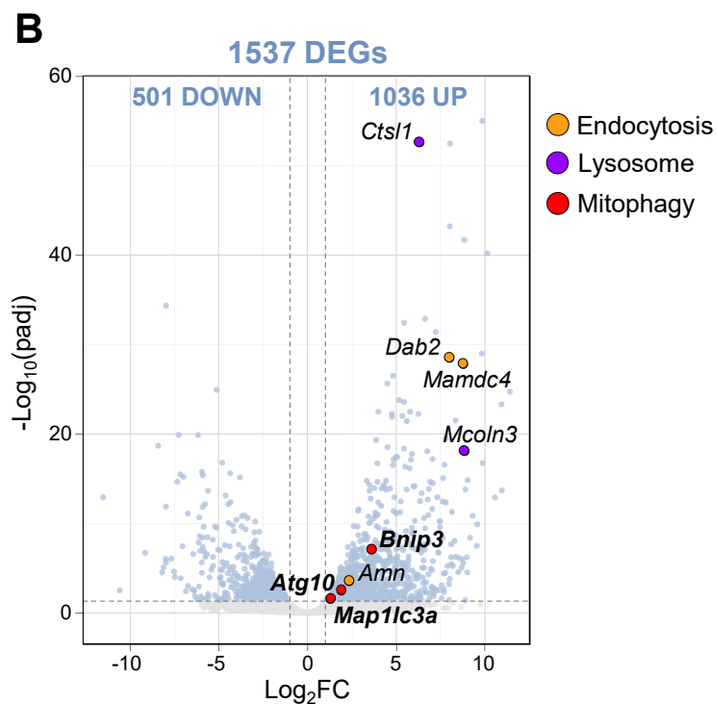
B
1537 DEGs
501 DOWN
1036 UP
Ctsl1
Dab2
Mamdc4
Mcoln3
Bnip3
Amn
Atg10
Map1lc3a
Endocytosis
Lysosome
Mitophagy
-Log10(padj)
Log2FC

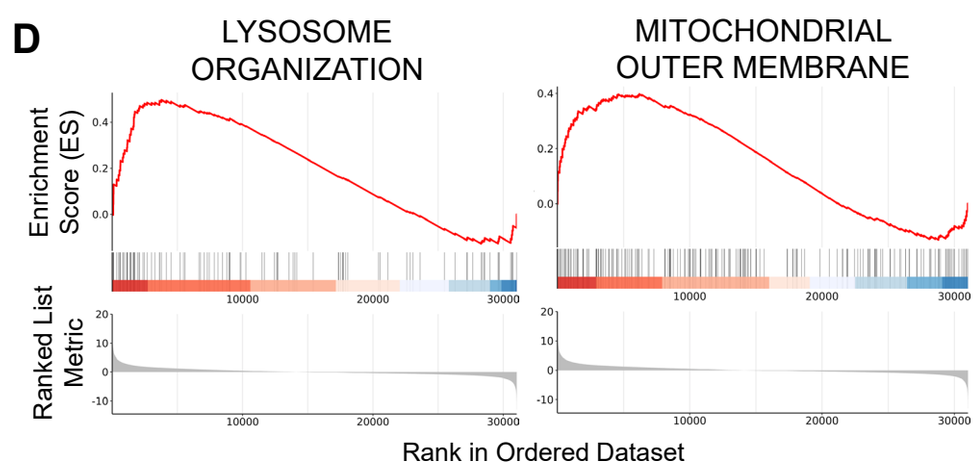
D
LYSOSOME ORGANIZATION
MITOCHONDRIAL OUTER MEMBRANE
Enrichment Score (ES)
Ranked List Metric
Rank in Ordered Dataset

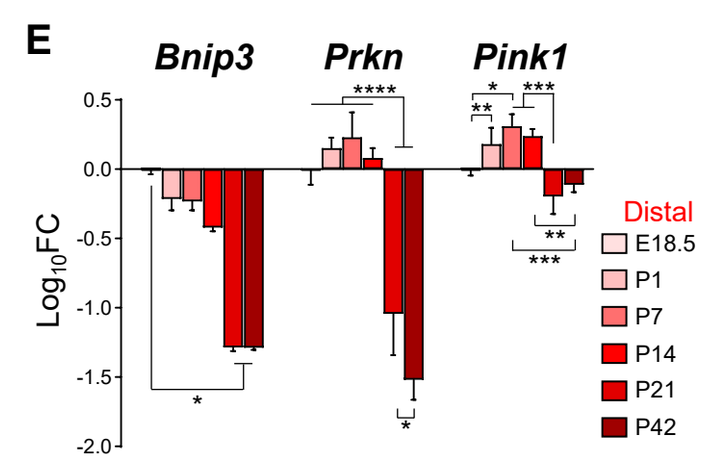
E
Bnip3
Prkn
Pink1
Log10FC
Distal
E18.5
P1
P7
P14
P21
P42

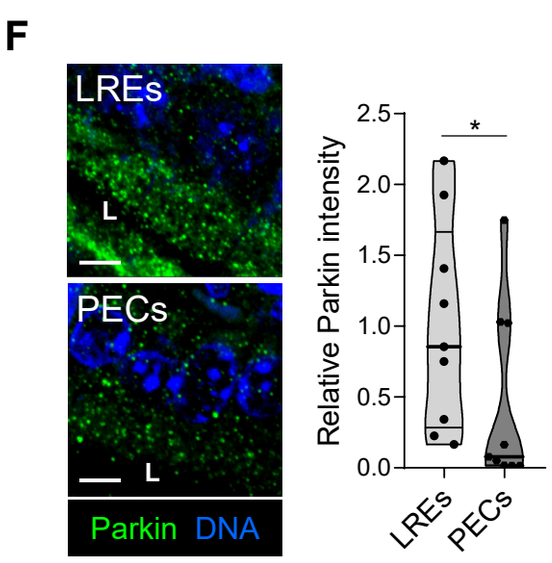
F
LREs
PECs
Parkin DNA
Relative Parkin intensity
LREs
PECs

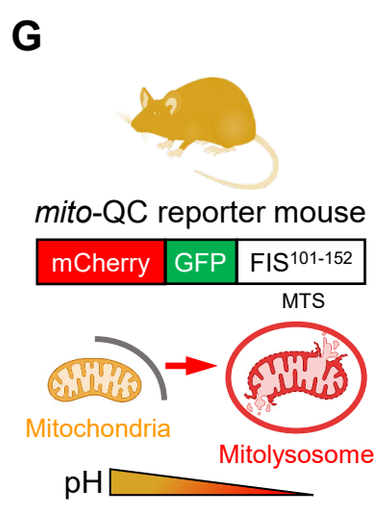
G
mito-QC reporter mouse
mCherry
GFP
FIS101-152
MTS
Mitochondria
Mitolysosome
pH

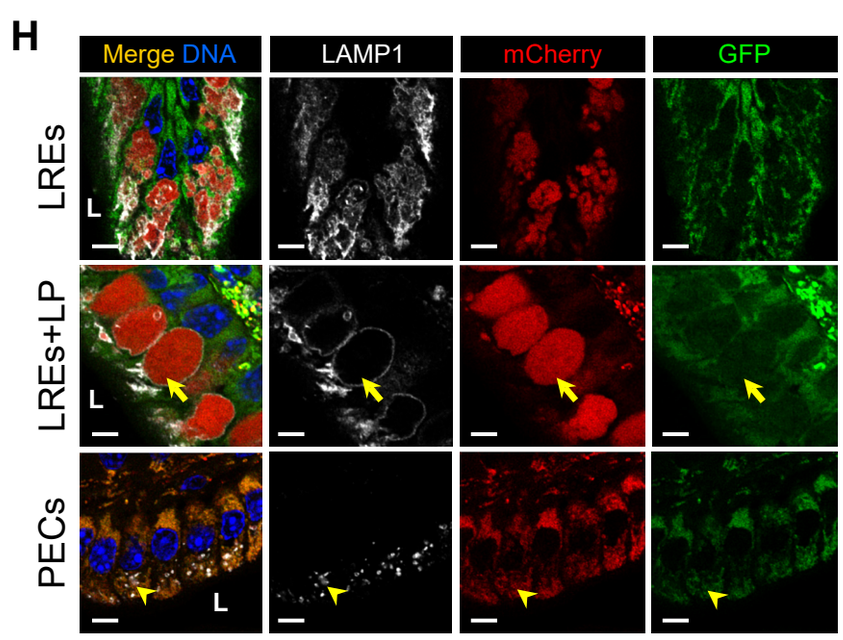
H
Merge DNA
LAMP1
mCherry
GFP
LREs
LREs+LP
PECs

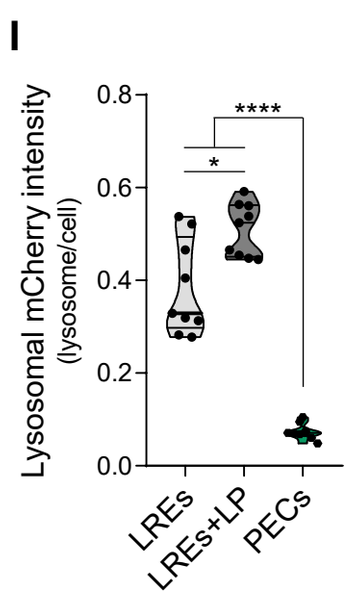
I
Lysosomal mCherry intensity
(lysosome/cell)
LREs
LREs+LP
PECs

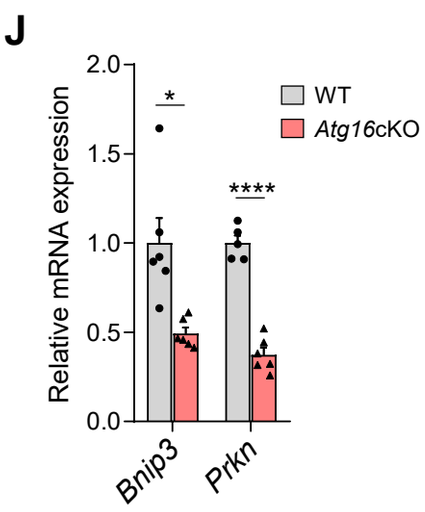
J
Relative mRNA expression
WT
Atg16cKO
Bnip3
Prkn

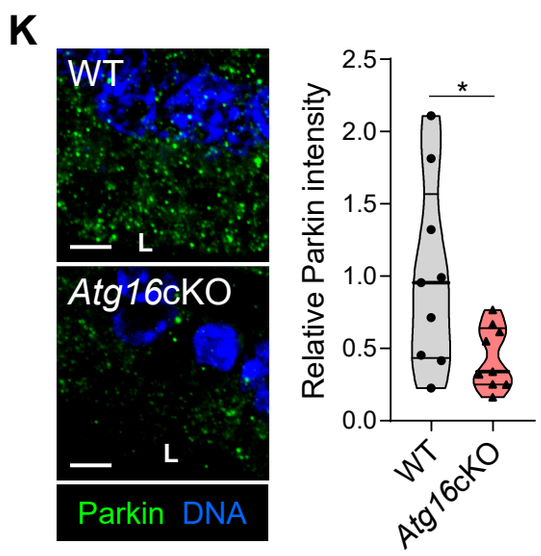
K
WT
Atg16cKO
Parkin DNA
Relative Parkin intensity
WT
Atg16cKO

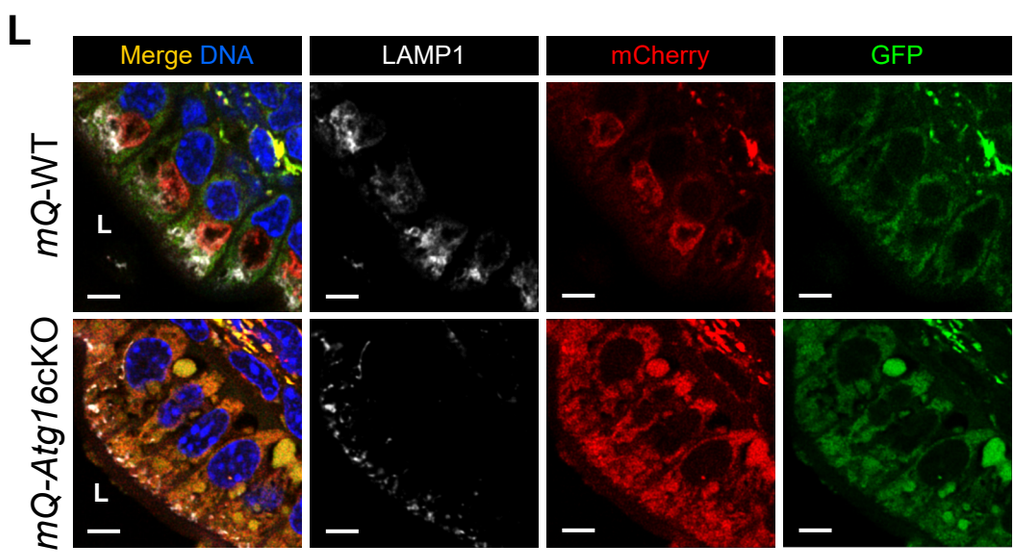
L
Merge DNA
LAMP1
mCherry
GFP
mQ-WT
mQ-Atg16cKO

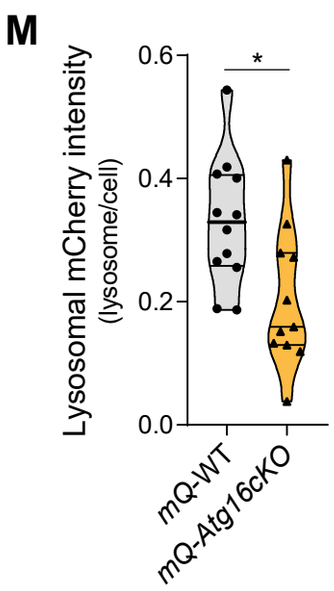
M
Lysosomal mCherry intensity
(lysosome/cell)
mQ-WT
mQ-Atg16cKO

Figure 4

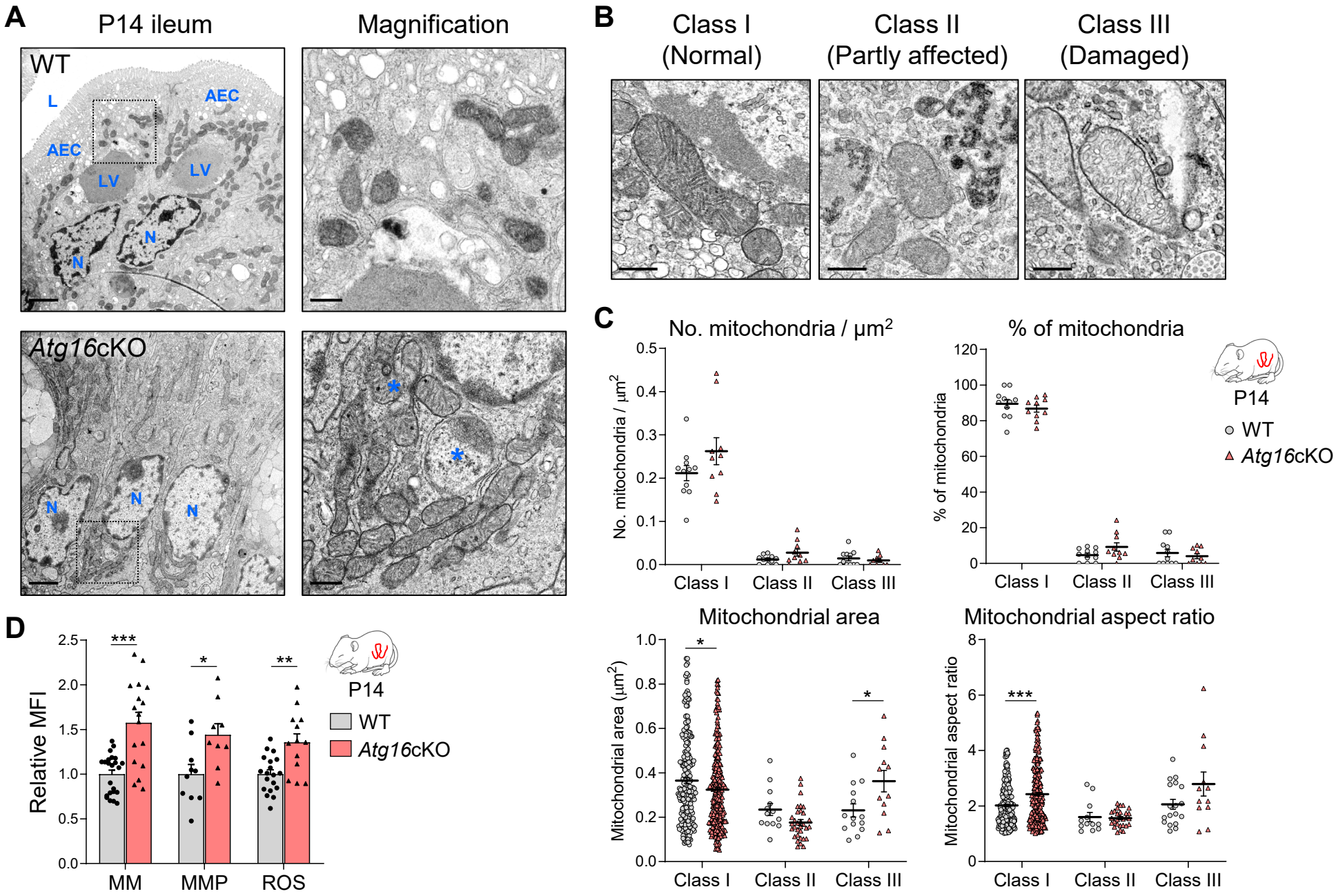
A
P14 ileum
Magnification
WT
L
AEC
AEC
LV
LV
N
N
Atg16cKO
N
N
N
B
Class I
(Normal)
Class II
(Partly affected)
Class III
(Damaged)
C
No. mitochondria / μm²
No. mitochondria / μm²
Class I
Class II
Class III
% of mitochondria
% of mitochondria
P14
WT
Atg16cKO
Mitochondrial area
Mitochondrial area (μm²)
Mitochondrial aspect ratio
Mitochondrial aspect ratio
D
Relative MFI
MM
MMP
ROS
P14
WT
Atg16cKO

Figure 5

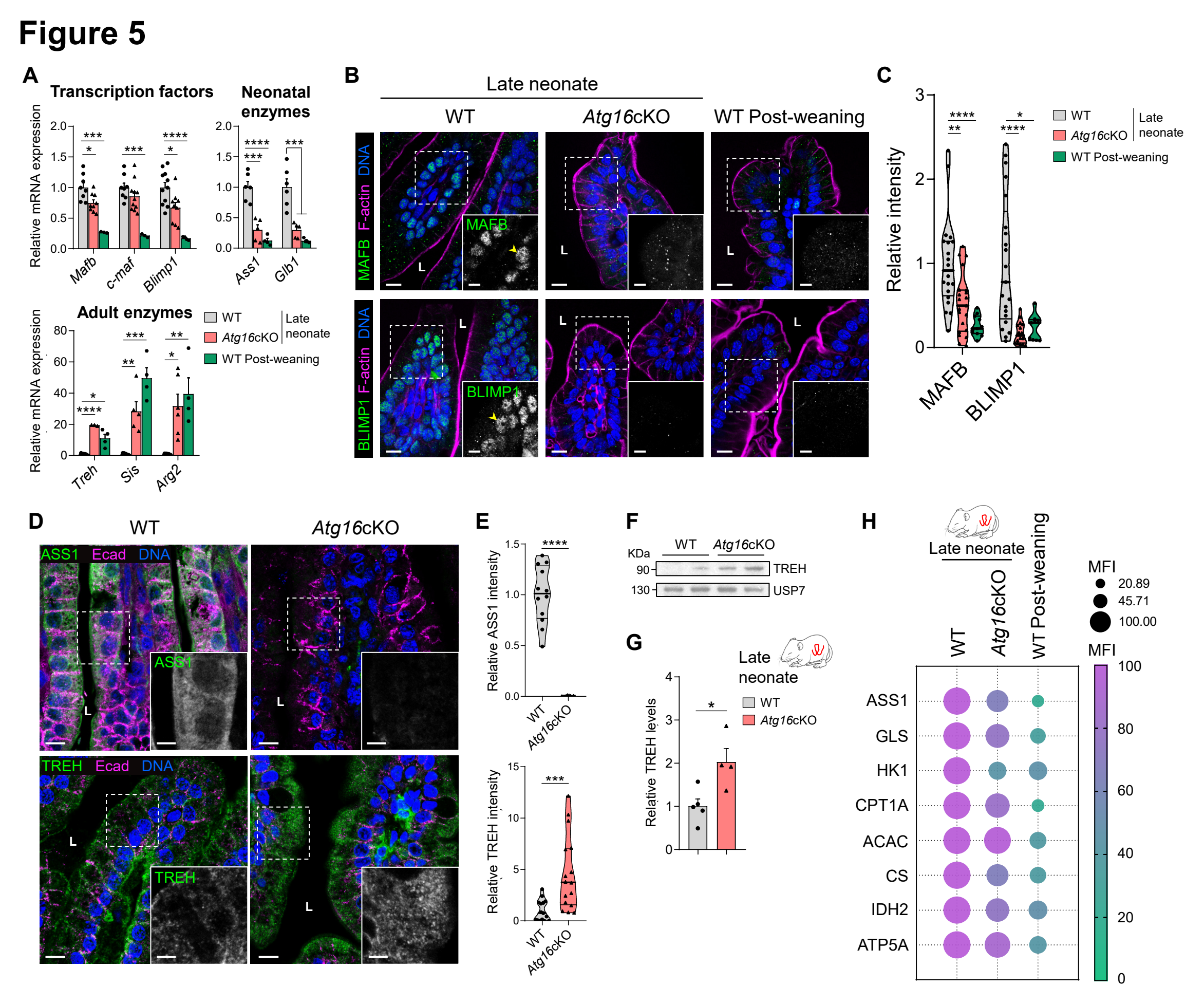
A
Transcription factors
Neonatal enzymes
Relative mRNA expression
Mafb
c-maf
Blimp1
Ass1
Glb1
Adult enzymes
Treh
Sis
Arg2
WT
Atg16cKO
WT Post-weaning
Late neonate
B
Late neonate
WT
Atg16cKO
WT Post-weaning
MAFB F-actin DNA
BLIMP1 F-actin DNA
MAFB
BLIMP1
L
C
Relative intensity
MAFB
BLIMP1
D
WT
Atg16cKO
ASS1 Ecad DNA
TREH Ecad DNA
ASS1
TREH
E
Relative ASS1 intensity
Relative TREH intensity
F
KDa
WT
Atg16cKO
90
130
TREH
USP7
G
Late neonate
Relative TREH levels
H
Late neonate
WT
Atg16cKO
WT Post-weaning
MFI
20.89
45.71
100.00
ASS1
GLS
HK1
CPT1A
ACAC
CS
IDH2
ATP5A

Figure 6

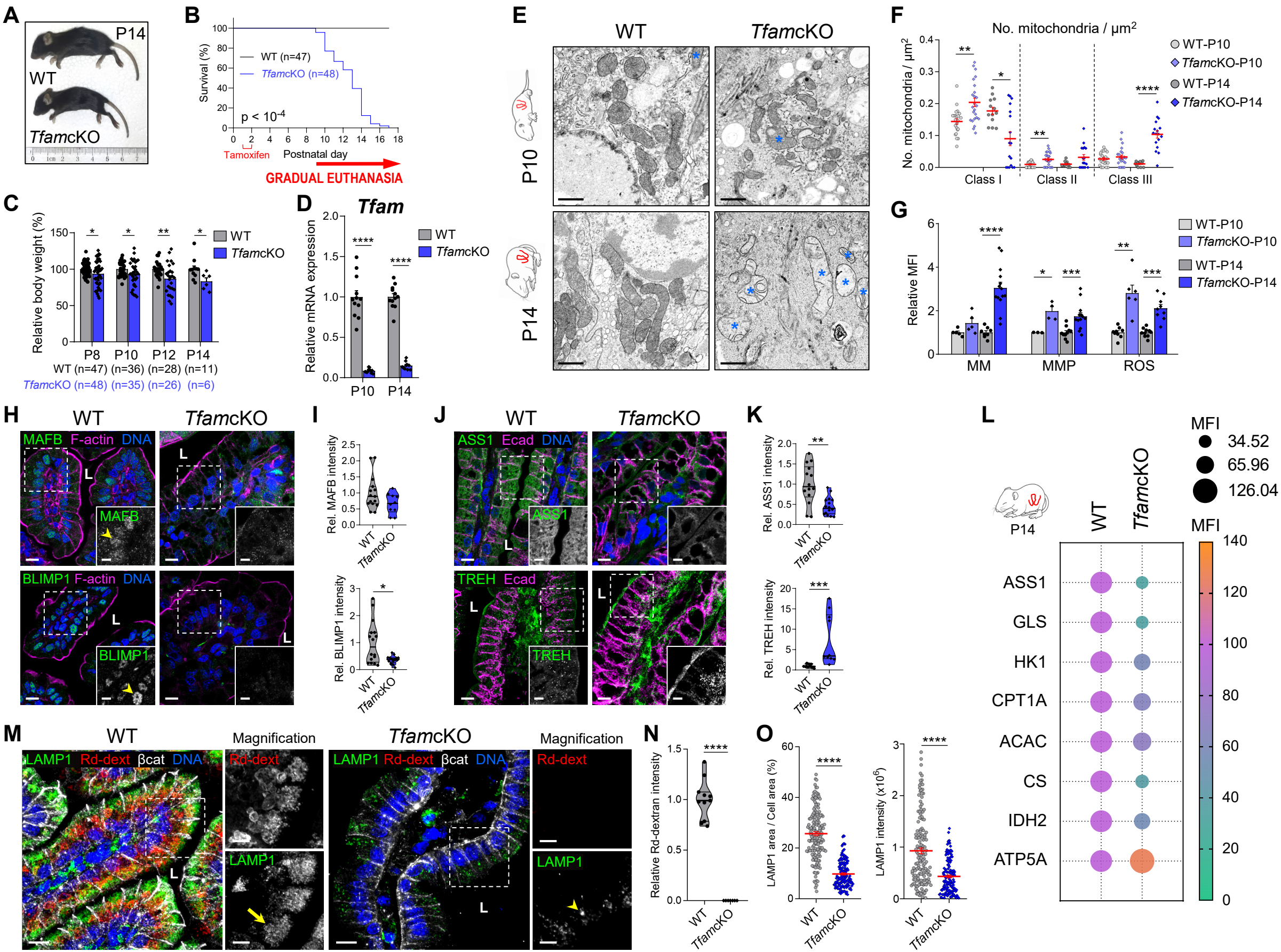
A
P14
WT
TfamcKO
B
Survival (%)
WT (n=47)
TfamcKO (n=48)
p < 10-4
Tamoxifen
Postnatal day
GRADUAL EUTHANASIA
C
Relative body weight (%)
WT
TfamcKO
P8 P10 P12 P14
WT (n=47) (n=36) (n=28) (n=11)
TfamcKO (n=48) (n=35) (n=26) (n=6)
D
Tfam
Relative mRNA expression
P10 P14
E
WT
TfamcKO
P10
P14
F
No. mitochondria / µm2
WT-P10
TfamcKO-P10
WT-P14
TfamcKO-P14
Class I
Class II
Class III
G
Relative MFI
MM
MMP
ROS
H
WT
TfamcKO
MAFB F-actin DNA
MAFB
BLIMP1 F-actin DNA
BLIMP1
Rel. MAFB intensity
Rel. BLIMP1 intensity
I
J
ASS1 Ecad DNA
ASS1
TREH Ecad
TREH
K
Rel. ASS1 intensity
Rel. TREH intensity
L
MFI
34.52
65.96
126.04
P14
ASS1
GLS
HK1
CPT1A
ACAC
CS
IDH2
ATP5A
M
WT
TfamcKO
Magnification
LAMP1 Rd-dext βcat DNA
Rd-dext
LAMP1
N
Relative Rd-dextran intensity
O
LAMP1 area / Cell area (%)
LAMP1 intensity (x10^6)

Figure 7

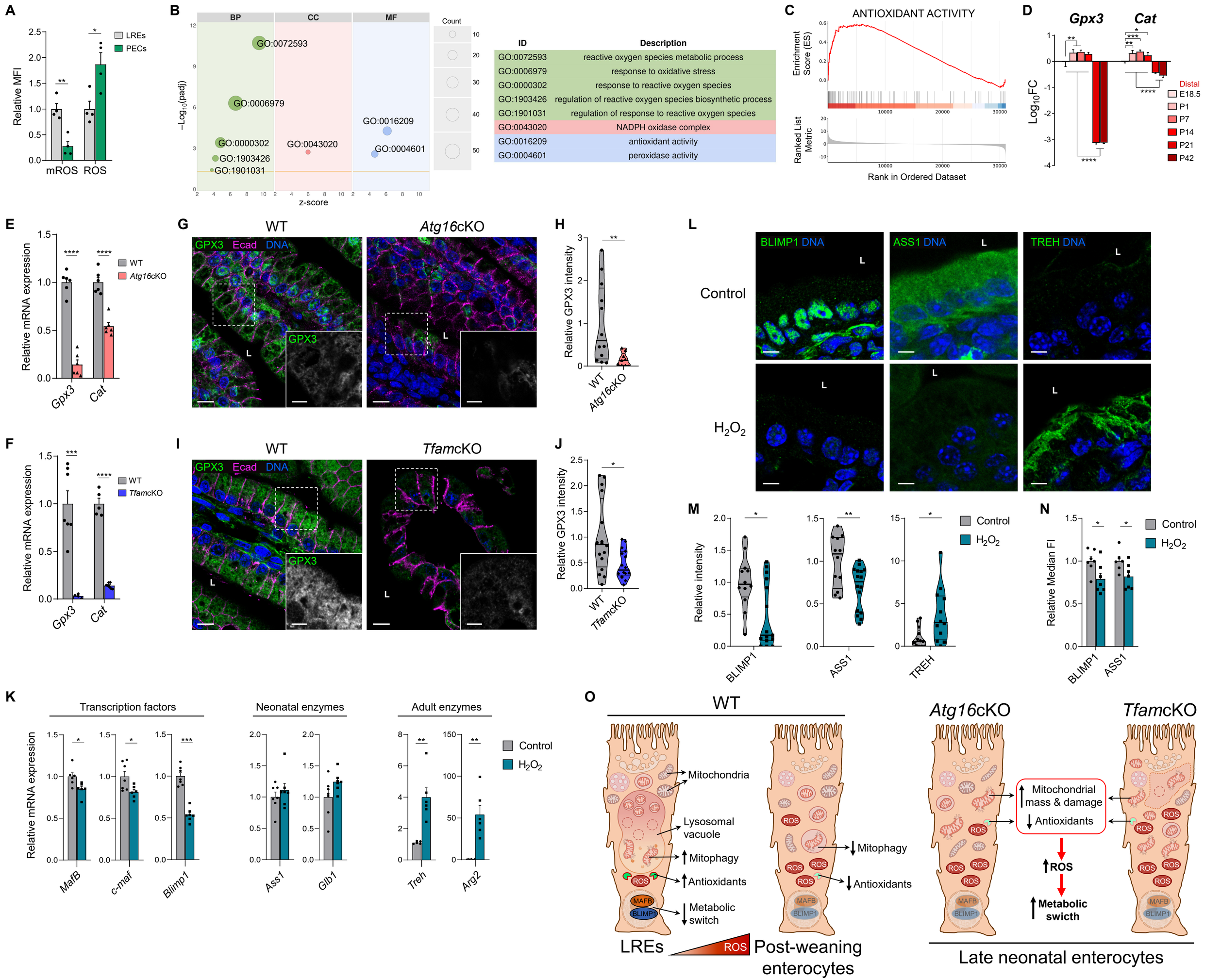
A
Relative MFI
LREs
PECs
mROS
ROS
B
BP
CC
MF
Count
GO:0072593
GO:0006979
GO:0000302
GO:1903426
GO:1901031
GO:0043020
GO:0016209
GO:0004601
z-score
ID
Description
GO:0072593 reactive oxygen species metabolic process
GO:0006979 response to oxidative stress
GO:0000302 response to reactive oxygen species
GO:1903426 regulation of reactive oxygen species biosynthetic process
GO:1901031 regulation of response to reactive oxygen species
GO:0043020 NADPH oxidase complex
GO:0016209 antioxidant activity
GO:0004601 peroxidase activity
C
ANTIOXIDANT ACTIVITY
Enrichment Score (ES)
Ranked List Metric
Rank in Ordered Dataset
D
Gpx3
Cat
Log10FC
Distal
E18.5
P1
P7
P14
P21
P42
E
Relative mRNA expression
WT
Atg16cKO
Gpx3
Cat
F
Relative mRNA expression
WT
TfamcKO
Gpx3
Cat
G
WT
Atg16cKO
GPX3 Ecad DNA
GPX3
L
H
Relative GPX3 intensity
WT
Atg16cKO
I
WT
TfamcKO
GPX3 Ecad DNA
GPX3
L
J
Relative GPX3 intensity
WT
TfamcKO
L
BLIMP1 DNA
ASS1 DNA
TREH DNA
Control
H2O2
M
Relative intensity
Control
H2O2
BLIMP1
ASS1
TREH
N
Relative Median FI
Control
H2O2
BLIMP1
ASS1
K
Transcription factors
Neonatal enzymes
Adult enzymes
Relative mRNA expression
Control
H2O2
MafB
c-maf
Blimp1
Ass1
Glb1
Treh
Arg2
O
WT
Mitochondria
Lysosomal vacuole
Mitophagy
Antioxidants
Metabolic switch
ROS
MAFB
BLIMP1
LREs
Post-weaning enterocytes
Atg16cKO
TfamcKO
Mitochondrial mass & damage
Antioxidants
ROS
Metabolic swicth
Late neonatal enterocytes

Figure S1

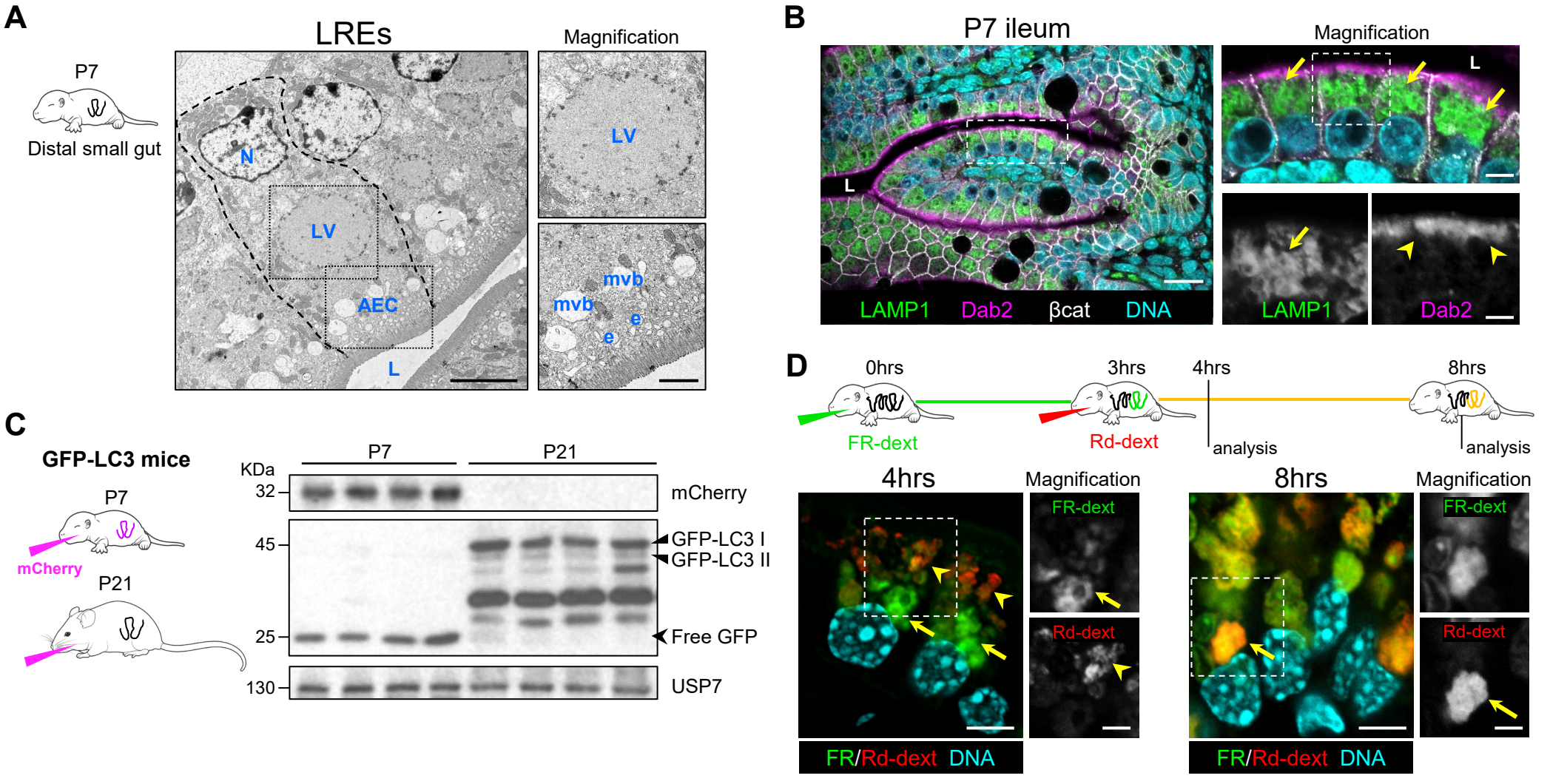
A
P7
Distal small gut
LREs
Magnification
N
LV
AEC
L
LV
mvb
mvb
e
e
B
P7 ileum
Magnification
L
L
LAMP1
Dab2
βcat
DNA
LAMP1
Dab2
C
GFP-LC3 mice
P7
mCherry
P21
KDa
P7
P21
32
45
25
130
mCherry
GFP-LC3 I
GFP-LC3 II
Free GFP
USP7
D
0hrs
3hrs
4hrs
8hrs
FR-dext
Rd-dext
analysis
analysis
4hrs
Magnification
8hrs
Magnification
FR-dext
Rd-dext
FR-dext
Rd-dext
FR/Rd-dext DNA
FR/Rd-dext DNA

Figure S2

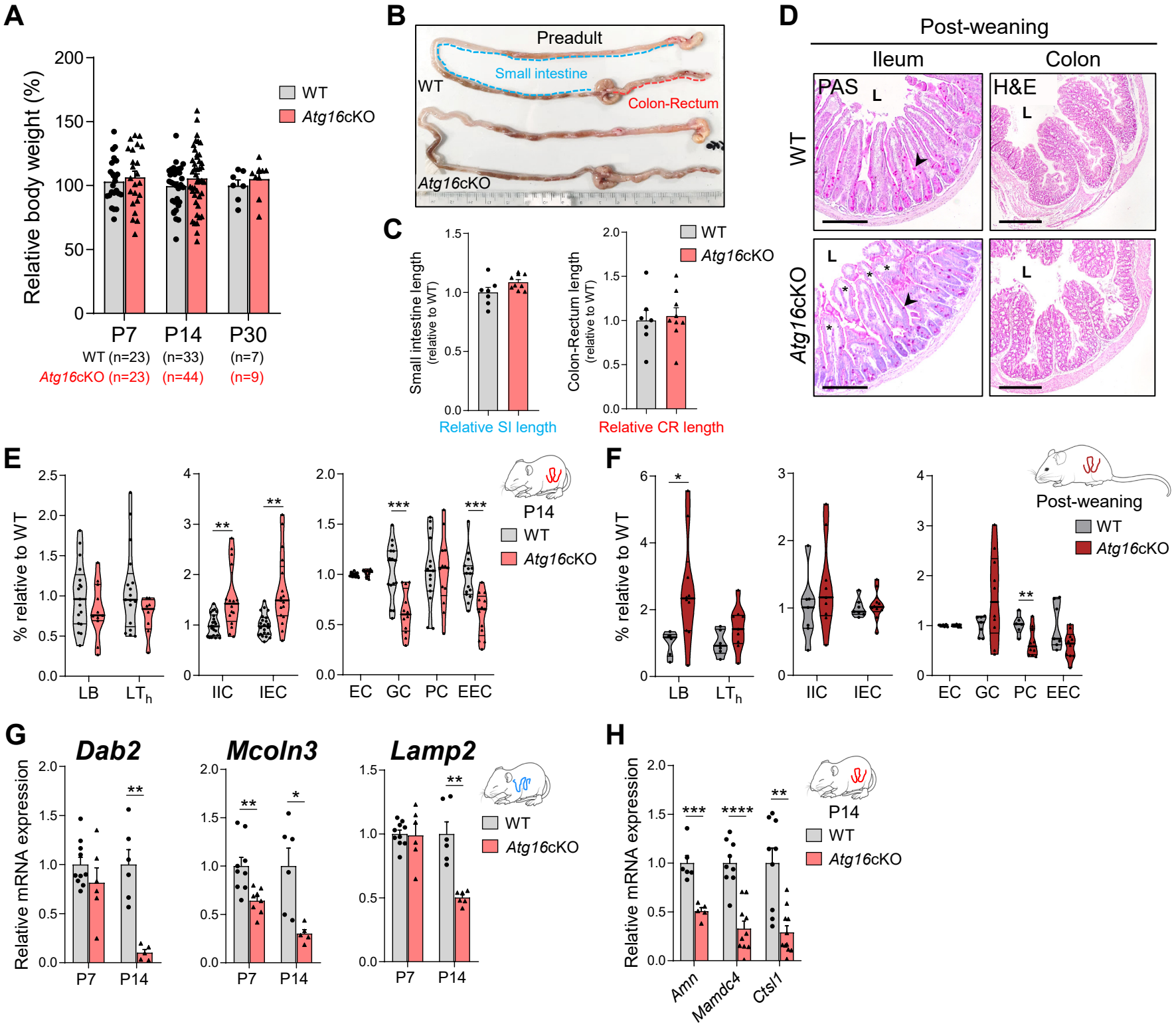
A
Relative body weight (%)
WT
Atg16cKO
P7
P14
P30
WT (n=23) (n=33) (n=7)
Atg16cKO (n=23) (n=44) (n=9)
B
Preadult
Small intestine
Colon-Rectum
WT
Atg16cKO
C
Small intestine length (relative to WT)
Colon-Rectum length (relative to WT)
Relative SI length
Relative CR length
D
Post-weaning
Ileum
Colon
PAS
H&E
L
E
% relative to WT
LB
LTh
IIC
IEC
EC
GC
PC
EEC
P14
F
Post-weaning
G
Dab2
Mcoln3
Lamp2
Relative mRNA expression
H
Amn
Mamdc4
Ctsl1

Figure S3

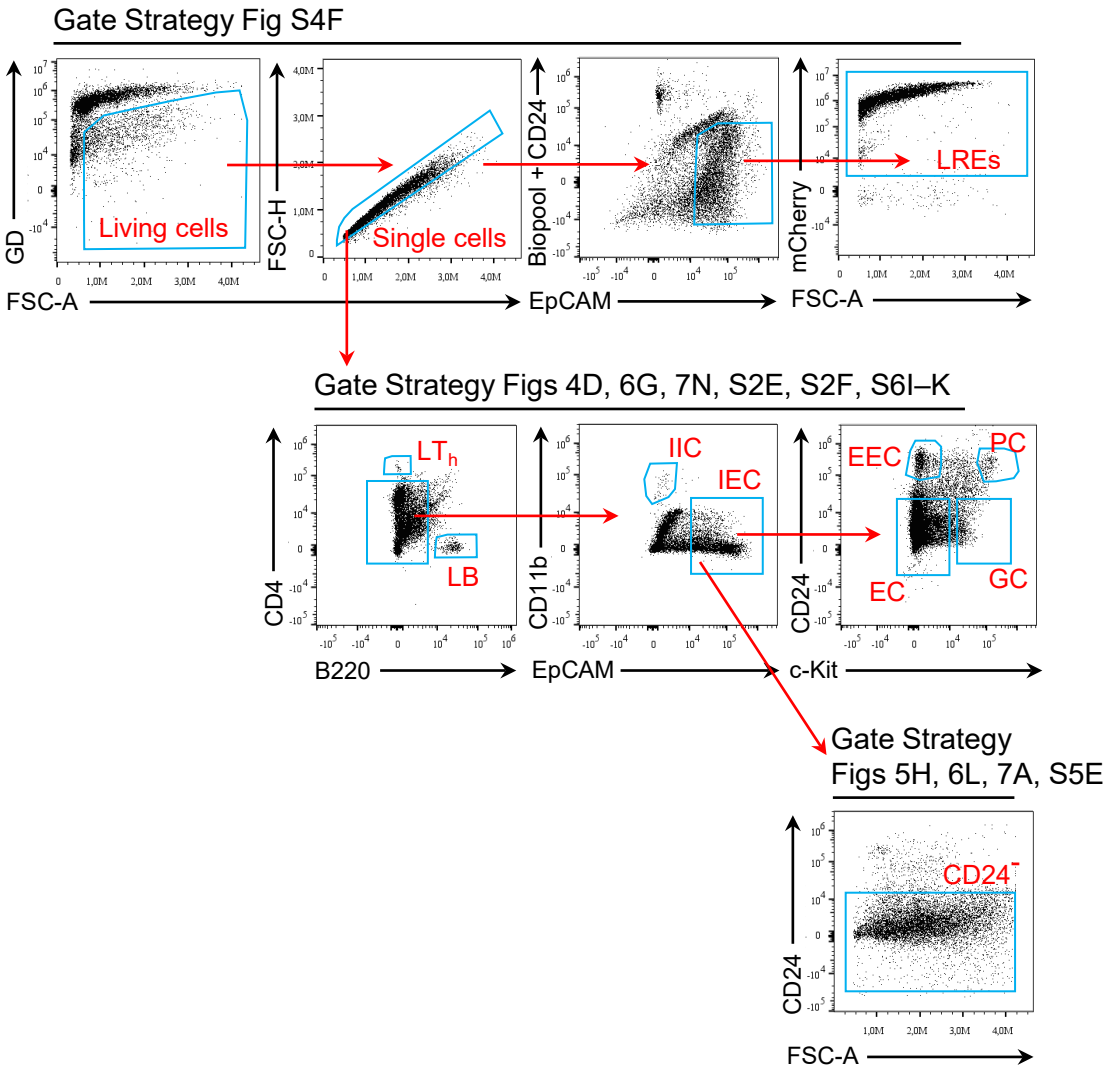
Gate Strategy Fig S4F
Living cells
Single cells
LREs
GD
FSC-A
FSC-H
Biopool + CD24
EpCAM
mCherry
FSC-A
Gate Strategy Figs 4D, 6G, 7N, S2E, S2F, S6I–K
LTh
LB
IIC
IEC
EEC
PC
EC
GC
CD4
B220
CD11b
EpCAM
CD24
c-Kit
Gate Strategy
Figs 5H, 6L, 7A, S5E
CD24-
CD24
FSC-A

Figure S4

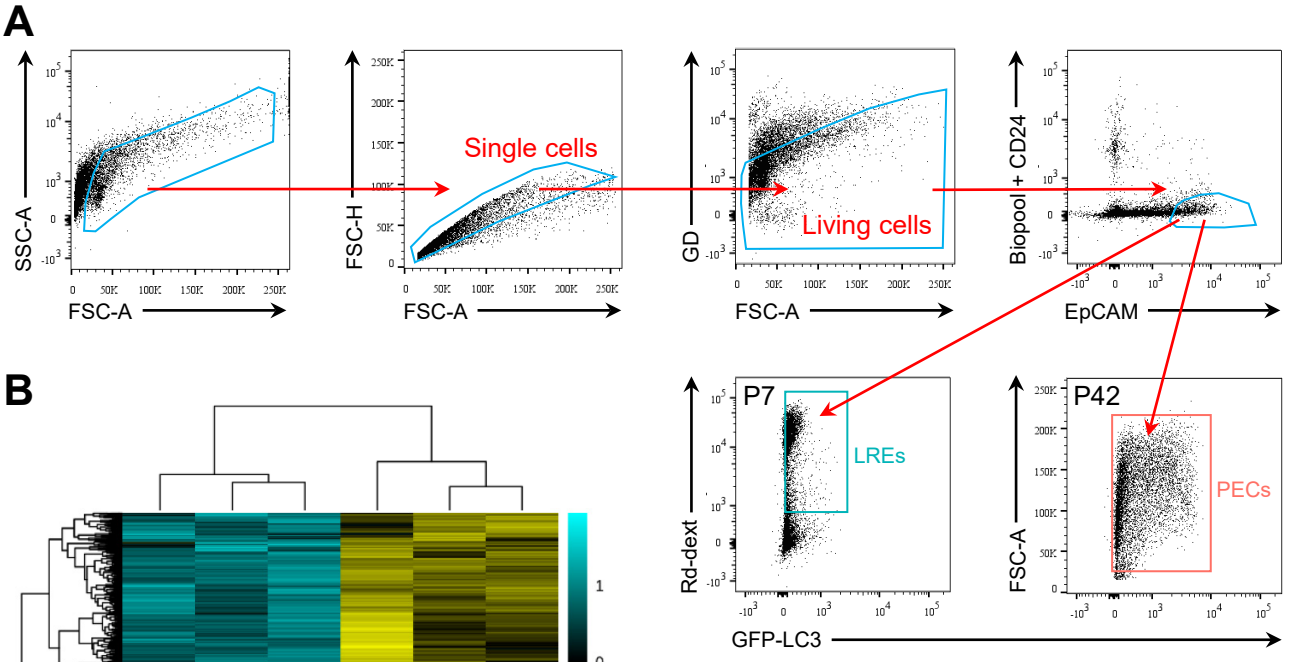

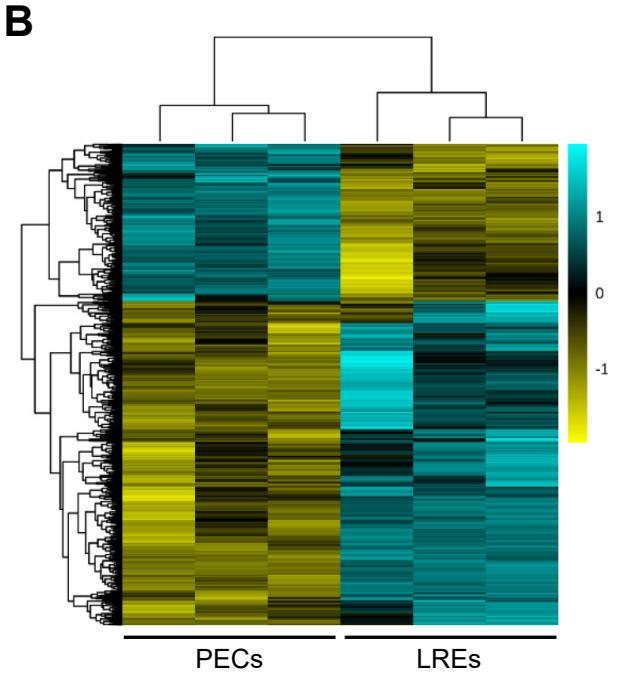

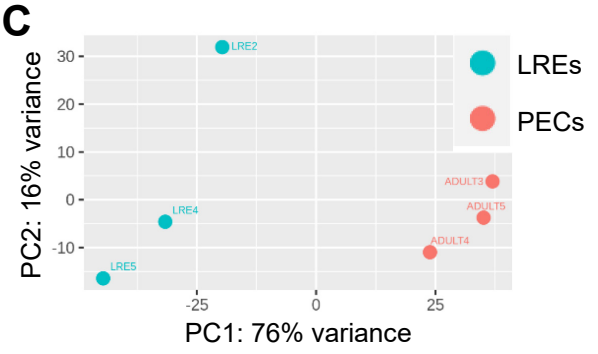

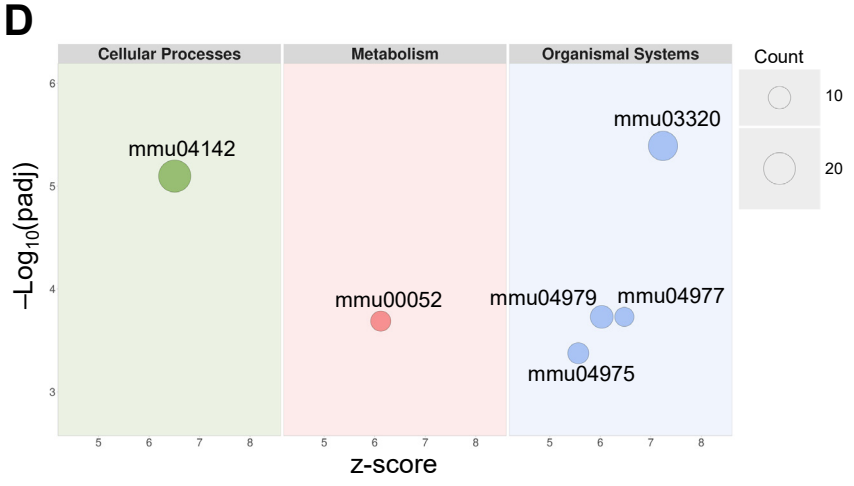

ID	Description
mmu04142	Lysosome
mmu00052	Galactose metabolism
mmu03320	PPAR signaling pathway
mmu04979	Cholesterol metabolism
mmu04977	Vitamin digestion and absorption
mmu04975	Fat digestion and absorption

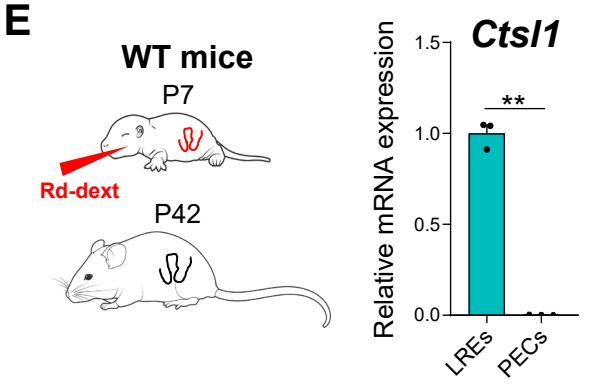

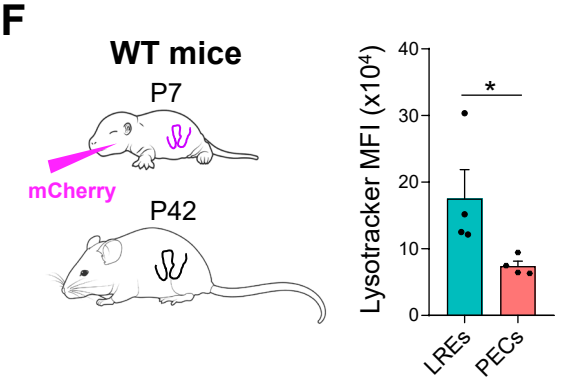

Figure S5

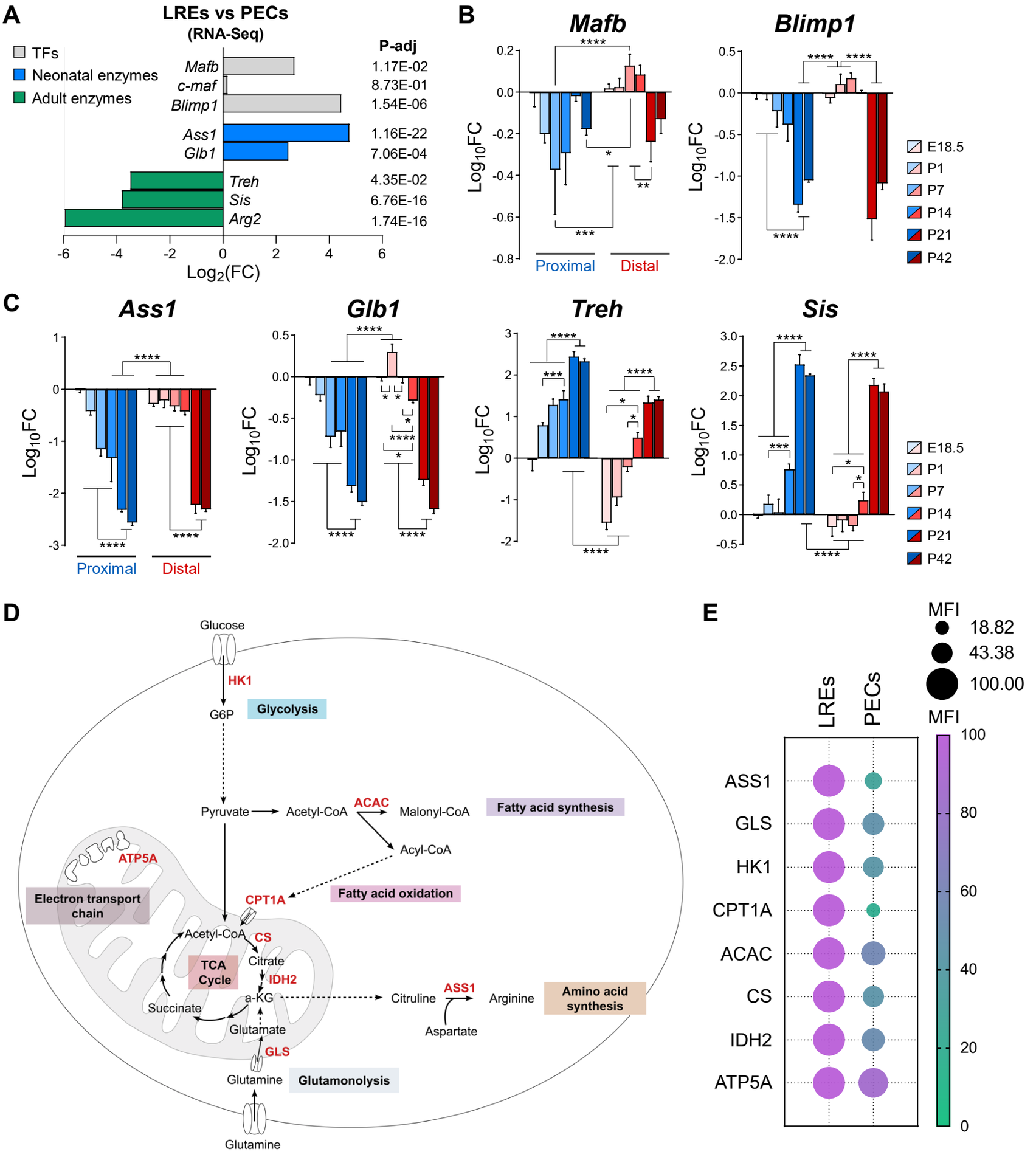
A
LREs vs PECs
(RNA-Seq)
TFs
Neonatal enzymes
Adult enzymes
P-adj
Mafb 1.17E-02
c-maf 8.73E-01
Blimp1 1.54E-06
Ass1 1.16E-22
Glb1 7.06E-04
Treh 4.35E-02
Sis 6.76E-16
Arg2 1.74E-16
Log2(FC)
B
Mafb
Blimp1
Log10FC
Proximal
Distal
E18.5
P1
P7
P14
P21
P42
C
Ass1
Glb1
Treh
Sis
D
Glucose
HK1
G6P
Glycolysis
Pyruvate
Acetyl-CoA
ACAC
Malonyl-CoA
Fatty acid synthesis
Acyl-CoA
ATP5A
Electron transport chain
CPT1A
Fatty acid oxidation
Acetyl-CoA
CS
Citrate
TCA Cycle
IDH2
a-KG
Succinate
Glutamate
Citruline
ASS1
Arginine
Aspartate
Amino acid synthesis
GLS
Glutamine
Glutamonolysis
Glutamine
E
MFI
18.82
43.38
100.00
LREs
PECs
ASS1
GLS
HK1
CPT1A
ACAC
CS
IDH2
ATP5A
100
80
60
40
20
0

Figure S6

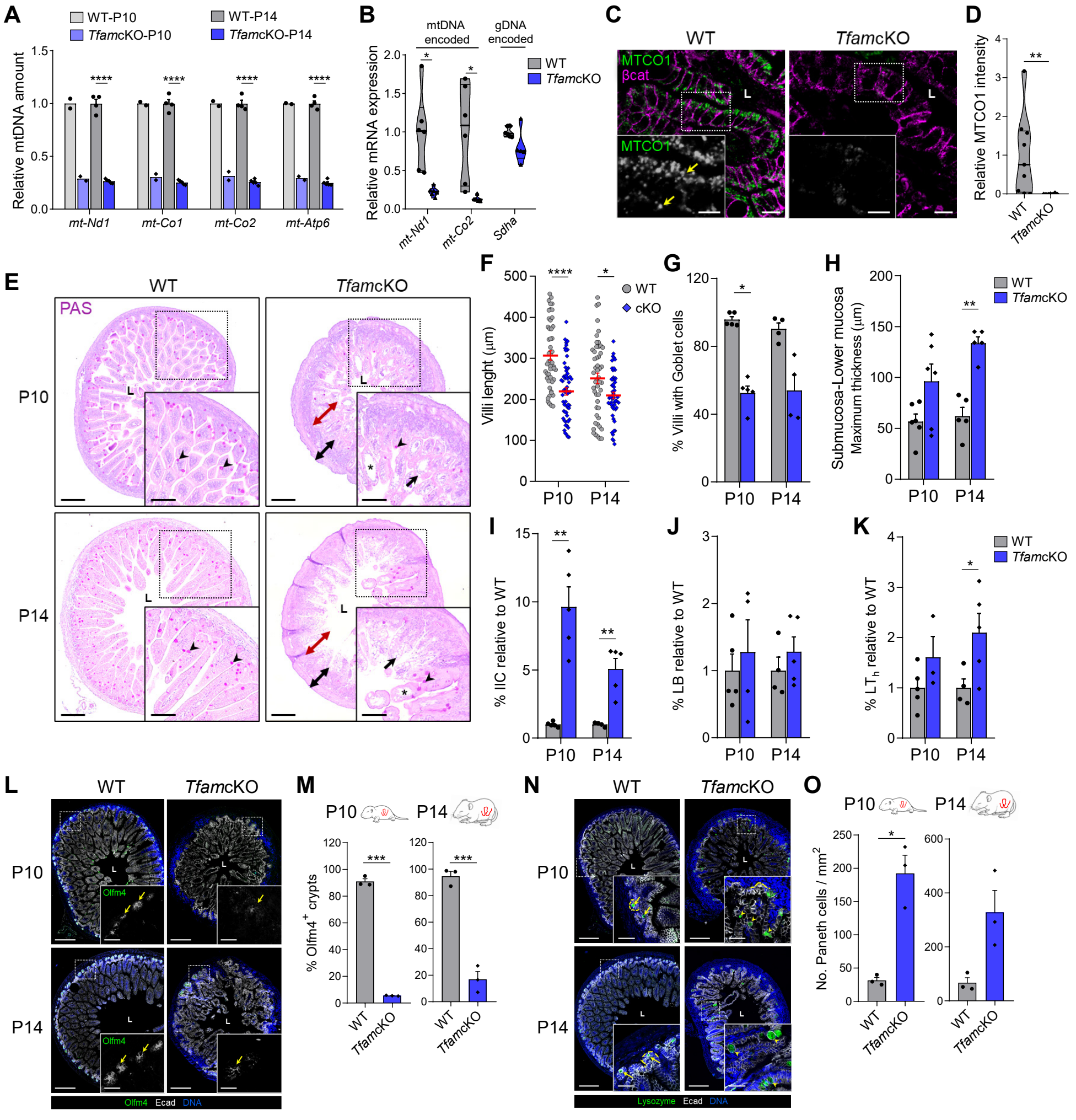
A
WT-P10
TfamcKO-P10
WT-P14
TfamcKO-P14
Relative mtDNA amount
mt-Nd1
mt-Co1
mt-Co2
mt-Atp6
B
mtDNA encoded
gDNA encoded
Relative mRNA expression
WT
TfamcKO
mt-Nd1
mt-Co2
Sdha
C
WT
TfamcKO
MTCO1
βcat
L
D
Relative MTCO1 intensity
E
WT
TfamcKO
PAS
P10
P14
F
Villi lenght (µm)
WT
cKO
G
% Villi with Goblet cells
H
Submucosa-Lower mucosa Maximum thickness (µm)
I
% IIC relative to WT
J
% LB relative to WT
K
% LTh relative to WT
L
Olfm4
Olfm4 Ecad DNA
M
% Olfm4+ crypts
N
Lysozyme Ecad DNA
O
No. Paneth cells / mm2
P
% of mitochondria
Mitochondrial area
Mitochondrial aspect ratio
Class I
Class II
Class III
WT-P10
TfamcKO-P10
WT-P14
TfamcKO-P14

Figure S7

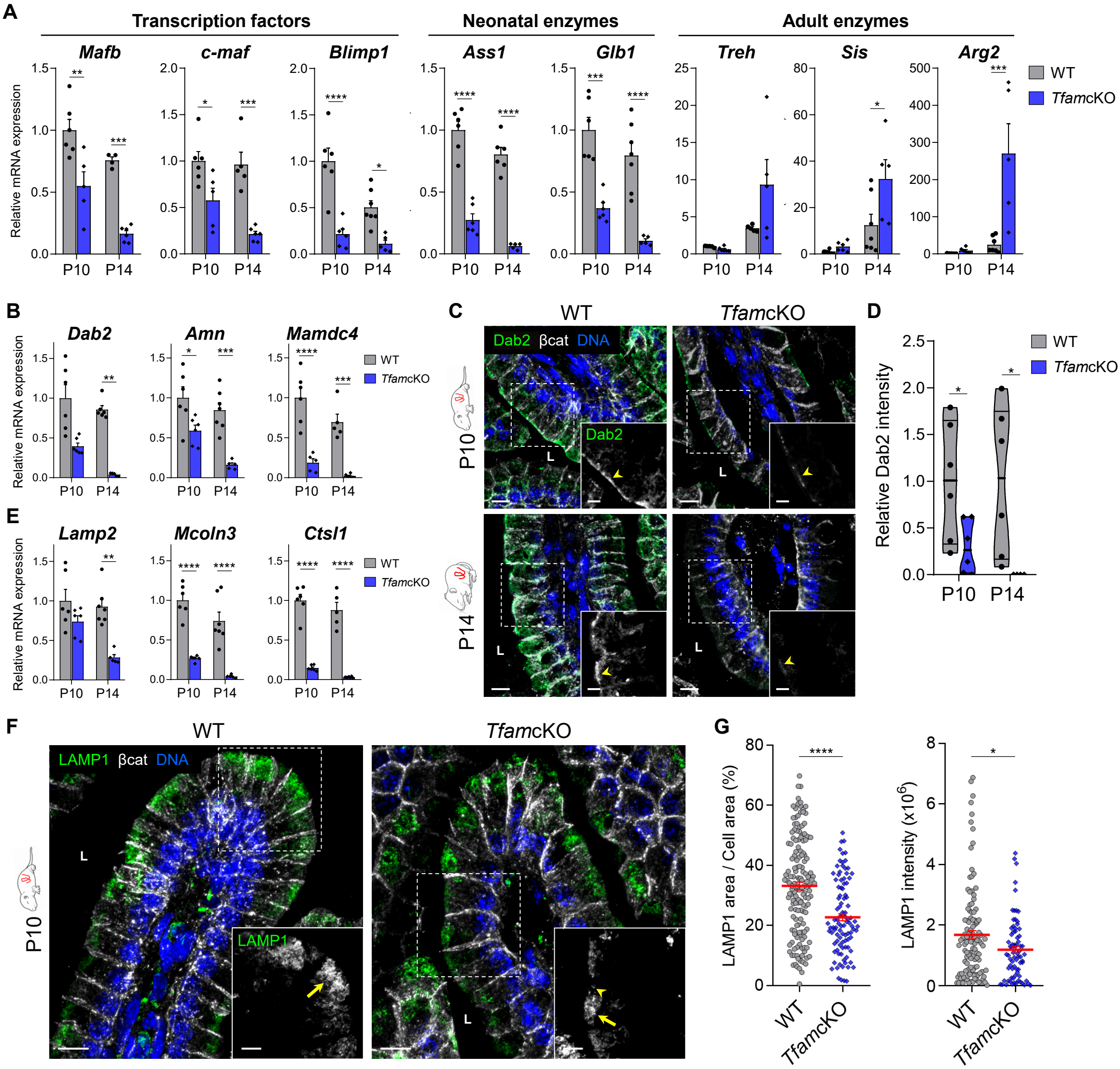
A
Transcription factors
Neonatal enzymes
Adult enzymes
Mafb
c-maf
Blimp1
Ass1
Glb1
Treh
Sis
Arg2
Relative mRNA expression
P10
P14
WT
TfamcKO
B
Dab2
Amn
Mamdc4
C
WT
TfamcKO
Dab2 βcat DNA
Dab2
L
P10
P14
D
Relative Dab2 intensity
E
Lamp2
Mcoln3
Ctsl1
F
LAMP1 βcat DNA
LAMP1
G
LAMP1 area / Cell area (%)
LAMP1 intensity (x10^6)

Table S1

	Class	No. mitochondria / μm^2	% of mitochondria	Mitochondrial area	Mitochondrial aspect ratio
Figure 4C	I	11, 10	11, 10	239, 271	239, 276
	II	11, 10	11, 10	13, 32	12, 28
	III	11, 9	11, 10	14, 12	18, 12
Figures 6F and S6P	I	23, 24, 13, 17	23, 24, 13, 17	184, 321, 259, 128	169, 329, 251, 130
	II	23, 24, 13, 17	23, 24, 12, 17	19, 73, 14, 45	21, 74, 15, 44
	III	23, 24, 13, 17	23, 24, 13, 17	45, 78, 17, 134	47, 78, 16, 149

Table S2

Protein	Figure 5H		Figure 6L	Figure S5E
	WT vs *Atg16*cKO	WT-P14 vs WT-Preadult		
ASS1	*	****	***	***
GLS	*	****	****	**
HK1	***	**	**	–
CPT1A	*	****	***	****
ACAC	NS	****	***	**
CS	****	****	***	****
IDH2	****	****	****	*
ATP5A	NS	****	*	NS